STATIC AND DYNAMIC ANALYSES OF VORTEX RESISTORS

By

SYED HAMID

Bachelor of Engineering
Sri Venkateswara University
Anantapur, India
1969

Master of Science
Oklahoma State University
Stillwater, Oklahoma
1972

Submitted to the Faculty of the Graduate College
of the Oklahoma State University
in partial fulfillment of the requirements
for the Degree of
DOCTOR OF PHILOSOPHY
July, 1976

STATIC AND DYNAMIC ANALYSES OF
VORTEX RESISTORS

Thesis Approved:

Karl N. Reid
Thesis Adviser

Jerald D. Parker

Don F. Kincannon

William G. Tiederman, Jr.

Norman N. Durham
Dean of the Graduate College

ACKNOWLEDGMENTS

I would like to express my appreciation to my thesis adviser Dr. Karl N. Reid for his guidance, encouragement, and technical supervision during my doctoral program. Discussions with him have been most valuable in my technical development.

I would like to thank Dr. W. G. Tiederman, Dr. J. D. Parker, and Dr. D. F. Kincannon for serving on my thesis committee.

Thanks are also extended to Dr. H. R. Sebesta, Dr. J. P. Chandler, Dr. A. H. Soni, and Dr. D. W. Grace for their encouragement and help.

I would like to thank my parents for their encouragement and support.

I wish to express my sincere thanks to Dr. B. N. Murali for his encouragement and help.

I would also like to thank my friends and colleagues, V. Maddali, H. W. Chang, D. Smith, and G. Prakash for their companionship.

I would like to express my gratitude to my school teacher Mr. K. Janardan Rao whose instructions had a profound influence on my academic career.

I would like to acknowledge Harry Diamond Laboratories for their support through contract DAAG-39-75-C-0028.

Lastly, Mrs. Carol Taylor deserves special thanks for her expert typing of this thesis.

TABLE OF CONTENTS

Chapter Page

LIST OF TABLES

LIST OF FIGURES

NOMENCLATURE

A	- Cross-sectional area of the loading orifice, in.^{2}
b	- Width of the inlet orifice, in.
C_{d1}	- Discharge coefficient of inlet orifice
C_{d2}	- Discharge coefficient of the central orifice
C_{d3}	- Discharge coefficient of the exit orifice of SVR
C_{d4}	- Discharge coefficient of the loading resistor
h	- Height of the vortex chamber, in.
K_1-K_4	- See Appendix E (Equations E.7 and E.26)
L	- Length of the capillary tube, in.
l_1	- Length of the inlet orifice, in.
l_2	- Length of the central orifice, in.
P_i	- Static pressure at the upstream of the vortex resistor, psi
P_o	- Static pressure at the downstream of the vortex resistor, psi
P_u	- Static pressure at the upstream of the central orifice (see Equation B.13), psi
P_1	- Static pressure at the outer periphery of the vortex chamber, psi
P_2	- Static pressure at the exit of the vortex chamber, psi
P_3	- Static pressure at the downstream of the central orifice, psi
P_4	- Static pressure at the inlet of the orifice of the SVR, psi
Q	- Volumetric flow rate, in.^{3}/sec.
R	- Resistance of fluid resistor, lbf.sec/in.^{5}

r - Radial coordinate, in.

Re_d - Reynolds number based on the diameter d

Re_{de} - Reynolds number based on a diameter d_e

r_1 - Radius of the vortex chamber, in.

r_2 - Radius of the central orifice, in.

T - Temperature of the operating fluid, °F

T_1 - Time delay, seconds

T_2 - First order lag, seconds

u - Radial velocity, in/sec.

u_1 - Radial velocity at the inlet of the vortex chamber, in/sec.

u_2 - Radial velocity at $r=r_2$ in the vortex chamber, in/sec.

u_3 - Radial velocity at $r=r_2$ in the diffuser chamber, in/sec.

u_δ , u_s - Radial velocity functions (see Equation D.7)

v - Tangential velocity, in/sec.

v_1 - Tangential velocity at the inlet of vortex chamber, in/sec.

v_2 - Tangential velocity at the inlet of the central orifice, in/sec.

v_3 - Tangential velocity at the downstream of the central orifice, in/sec.

v_3' - Tangential velocity at the inlet of the diffuser chamber, in/sec.

v_δ - Tangential velocity at $y=\delta$, in./sec.

w - Axial velocity in the central orifice, in./sec.

x_{m1} - Characteristic length used for shear stress calculations (see Appendix B), in.

x_{m2} - Characteristic length used for shear stress calculations (see Appendix B), in.

y - Axial coordinate, in.

$\Delta(\cdot)$ - Incremental change in the variable in the parenthesis (eg. p_i)

ΔP - Pressure drop across a resistor, lbf./in.^{2}

ΔQ - Change in volumetric flow rate, in.^{3}/sec.

δ - Boundary Layer Thickness, in.

$\alpha_1 - \alpha_5$ - Constants (see definitions in Appendix D)

λ - A dimensionless parameter defined by $24\mu\, r_1/h^2 u_1$

μ - Absolute viscosity of the fluid, $\frac{\text{lbf.sec}}{\text{in}^2}$

ν - Kinematic viscosity of the fluid, in^2/sec.

ρ - Fluid density, lbf.sec^2/in.^{4}

τ_t - Tangential shear stress, lbf/in.^{2}

τ_{t1} - Tangential shear stress on the annular wall of the vortex chamber, lbf/in.^{2}

τ_{t2} - Tangential shear stress in the vortex chamber, lbf/in.^{2}

τ_{t3} - Tangential shear stress in the central orifice, lbf/in.^{2}

CHAPTER I

INTRODUCTION

I.1. Background

In fluid power and fluidic systems resistors are used for various applications such as impedance matching, flow rate measurement and control. Orifices and capillary tubes are the most common fluid resistors. Figures 1 and 2 show typical steady-state characteristics of a capillary tube and a short-tube orifice respectively. Hydraulic fluid is assumed to be the operating medium here and throughout this thesis. Normally ΔP is considered the independent variable (plotted on abscissa) and Q the dependent variable (plotted on ordinate). Resistance is defined as the inverse slope of the Q vs. ΔP curve at an operating point, i.e., $R \equiv \partial(\Delta P)/\partial Q$. Since most fluid resistors are nonlinear (R depends on the operating point), it is convenient to describe the steady-state behavior in terms of the Q vs. ΔP relationship or "characteristic curve" instead of the "resistance." Resistor geometrical parameters, fluid thermodynamic properties (density and temperature or viscosity) determine the steady-state characteristics. The term "temperature sensitivity," used in this thesis, describes the variation of the steady-state flow rate through the resistor due to fluid temperature variation, i.e., $\partial Q/\partial T$ evaluated at an operating point. For fluid temperature ranges normally encountered in practice, the temperature sensitivity of a resistor can be substantial.

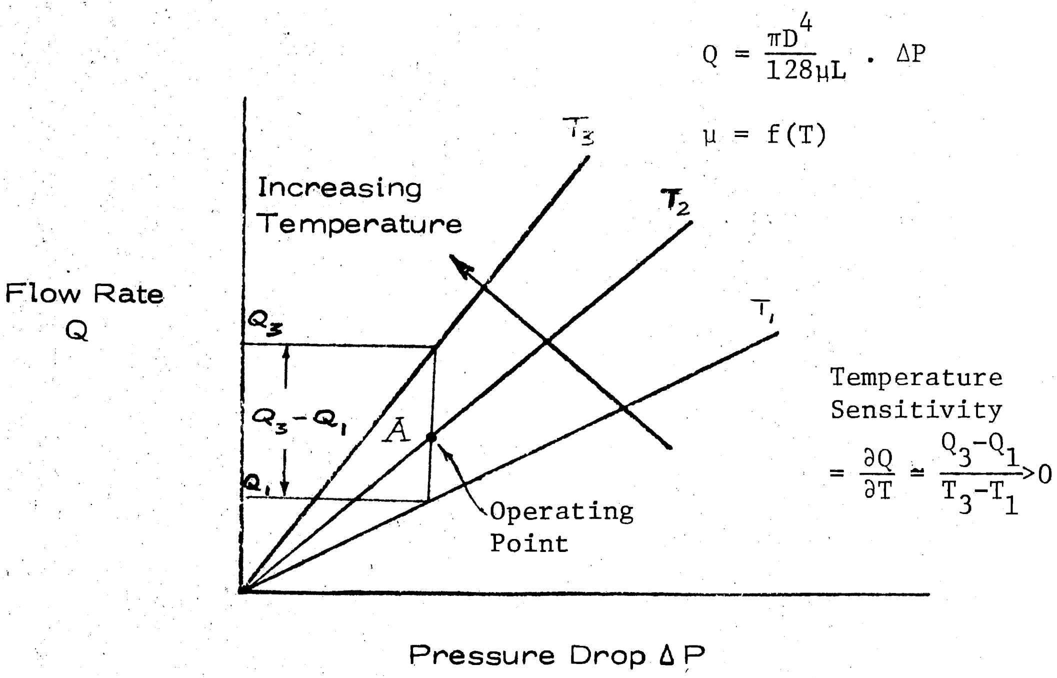

$$Q = \frac{\pi D^4}{128 \mu L} \cdot \Delta P$$

$$\mu = f(T)$$

Temperature Sensitivity

$$= \frac{\partial Q}{\partial T} \doteq \frac{Q_3 - Q_1}{T_3 - T_1} > 0$$

Figure 1. Steady-State Characteristics of a Capillary Tube (Assuming Fully-Developed Laminar Flow)

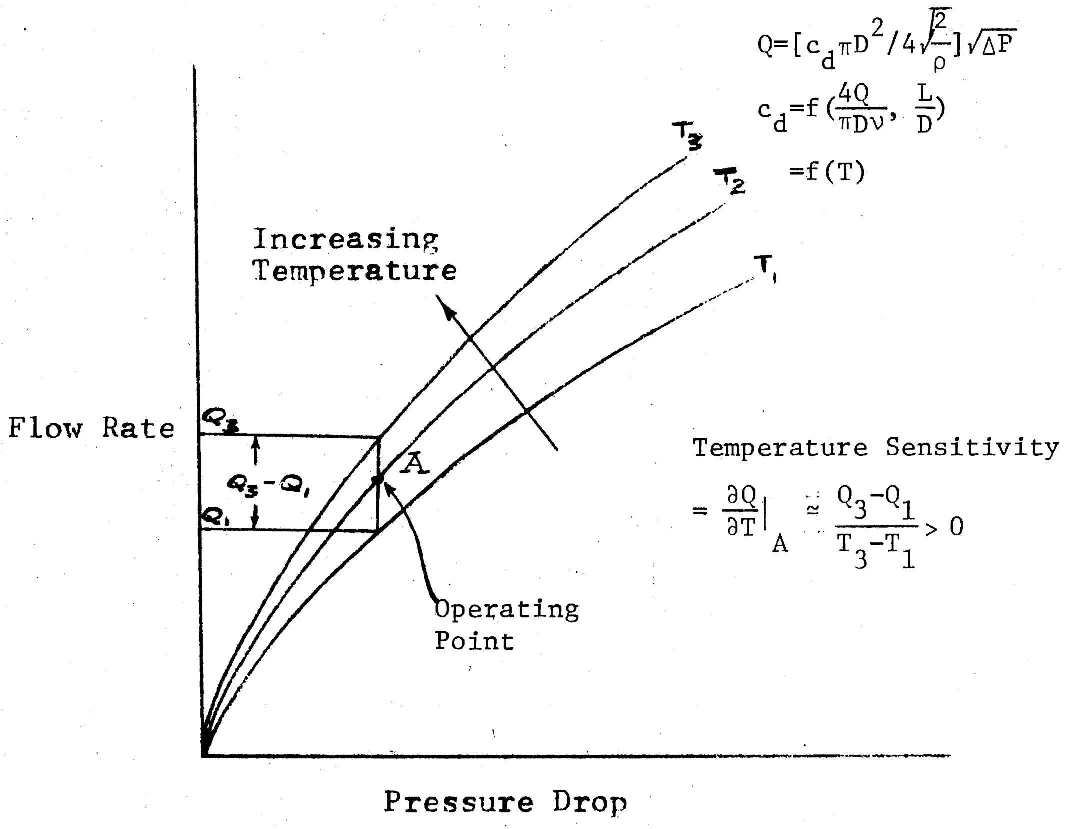

$$Q=[c_d \pi D^2/4\sqrt{\frac{2}{\rho}}]\sqrt{\Delta P}$$

$$c_d=f(\frac{4Q}{\pi D\nu}, \frac{L}{D})$$

$$=f(T)$$

Temperature Sensitivity

$$= \frac{\partial Q}{\partial T}\bigg|_A \simeq \frac{Q_3-Q_1}{T_3-T_1} > 0$$

Figure 2. Steady-State Characteristics of a Short-Tube Orifice With Sharp-Edged Entry

In many applications the variation of flow rate (at a constant pressure drop) with the temperature is undesirable. For example, if the pressure at the supply port of a hydraulic proportional amplifier is held constant (normal operation), the supply flow rate may vary substantially due to the sensitivity of the orifice resistance to temperature variations. This variation affects the gain characteristics of the amplifier and thereby alters steady-state and dynamic behavior of the associated system. In this case it is desirable to use a compensating resistor to minimize the temperature sensitivity of the supply port.

Vortex resistors can be designed to have a positive, zero, or negative temperature sensitivity. Capillary tubes and short-tube orifices always exhibit positive temperature sensitivities. Properly designed vortex resistors may be used with capillary tube and orifice type resistors to achieve temperature compensation.

Figures 3 and 4 show schematics of two types of vortex resistors: the Non-Symmetric Vortex Resistor, or "NSVR" (also called the vortex diode), and the Symmetric Vortex Resistor, or "SVR." Analysis of the fluid mechanics of the vortex resistors reveals that the resistance elements (orifices, vortex chamber and diffuser chamber) can be divided into two groups. One group (vortex chamber and central orifice) contributes a negative temperature sensitivity. In contrast, the second group contributes a positive temperature sensitivity effect and tends to cancel the effect of the first group. This second group consists of the inlet orifice and the sudden expansion diffuser in the case of the NSVR. In the SVR configuration, the inlet and exit orifices together with the diffuser chamber form the positive temperature sensitivity

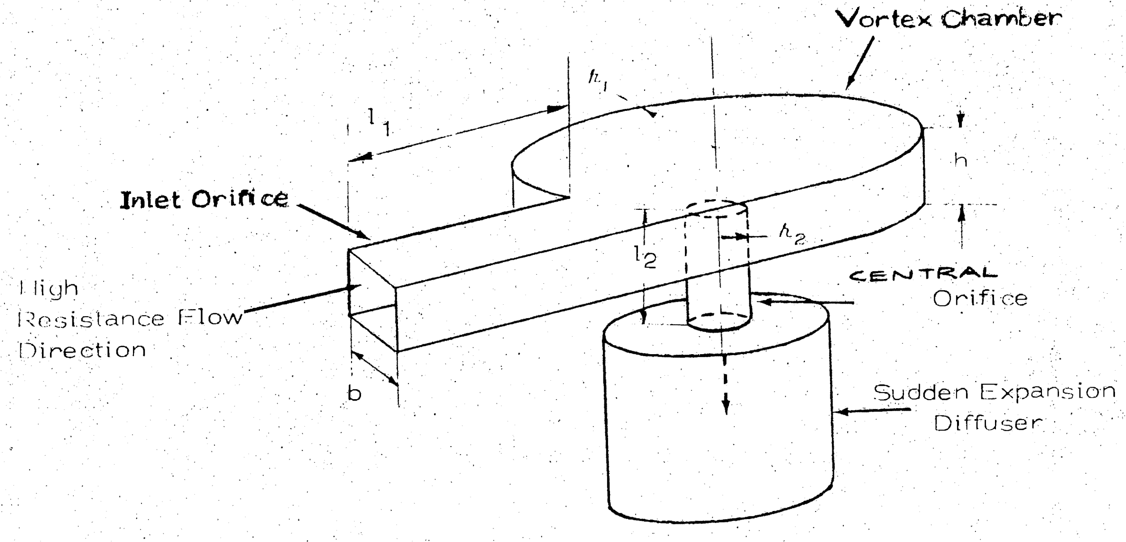

Figure 3. Geometry of a Non-Symmetric Vortex Resistor

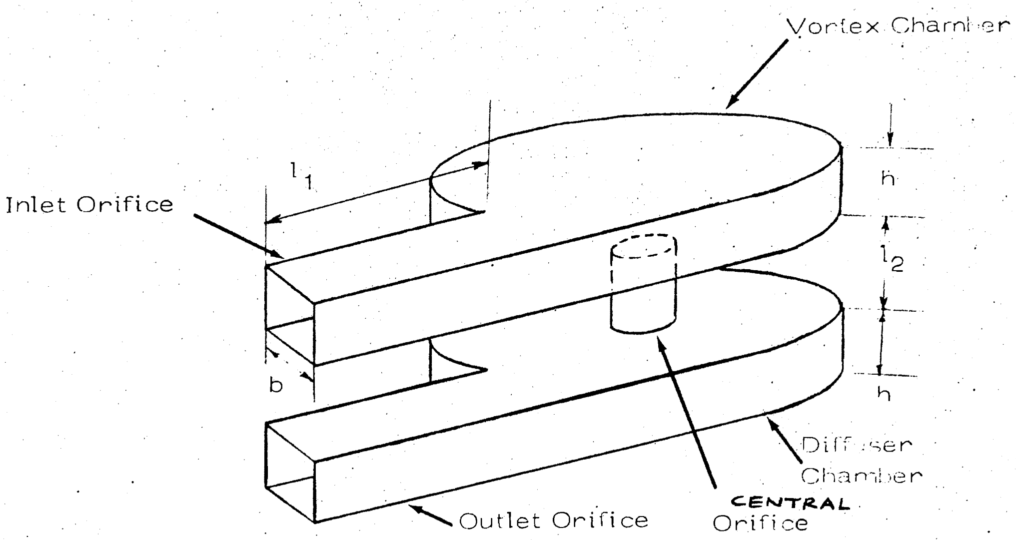

Figure 4. Geometry of a Symmetric Vortex Resistor

group. Figures 5 and 6 show measured steady-state characteristics for two NSVR geometries, one which exhibits a negative and one a small positive temperature sensitivity. When the positive and negative effects of the two resistance groups exactly match each other, the resultant vortex resistor is temperature-insensitive. Figure 7 shows a case in which the temperature sensitivity is near zero, or negligible.

For a given pressure drop and a comparable minimum dimension (i.e., vortex chamber height compared to orifice width or diameter), the vortex chamber can offer substantially higher resistance* than the simple orifice alone. Figure 8 shows the pressure drop-flow rate characteristics of two different vortex resistors and for a simple short-tube orifice which has the same geometry as the central orifice in the vortex resistors. The increase in resistance due to the inclusion of the vortex chamber is apparent. Thus, a given resistance can be achieved with a larger minimum dimension in a vortex resistor than in a simple short-tube orifice. Sensitivity to contamination due to solid particles in the hydraulic fluid is correspondingly less for the vortex resistor.

I.2. Scope of the Study

The principal objective of this study was to develop mathematical models which describe the steady-state and dynamic behavior of the two basic types of hydraulic vortex resistors, for flow in the high resistance direction. A steady-state model should relate the dependent variable Q to the independent variables ΔP and T; a dynamic model should also include time as an independent variable.

---

*$R \equiv \partial(\Delta P)/\partial Q$.

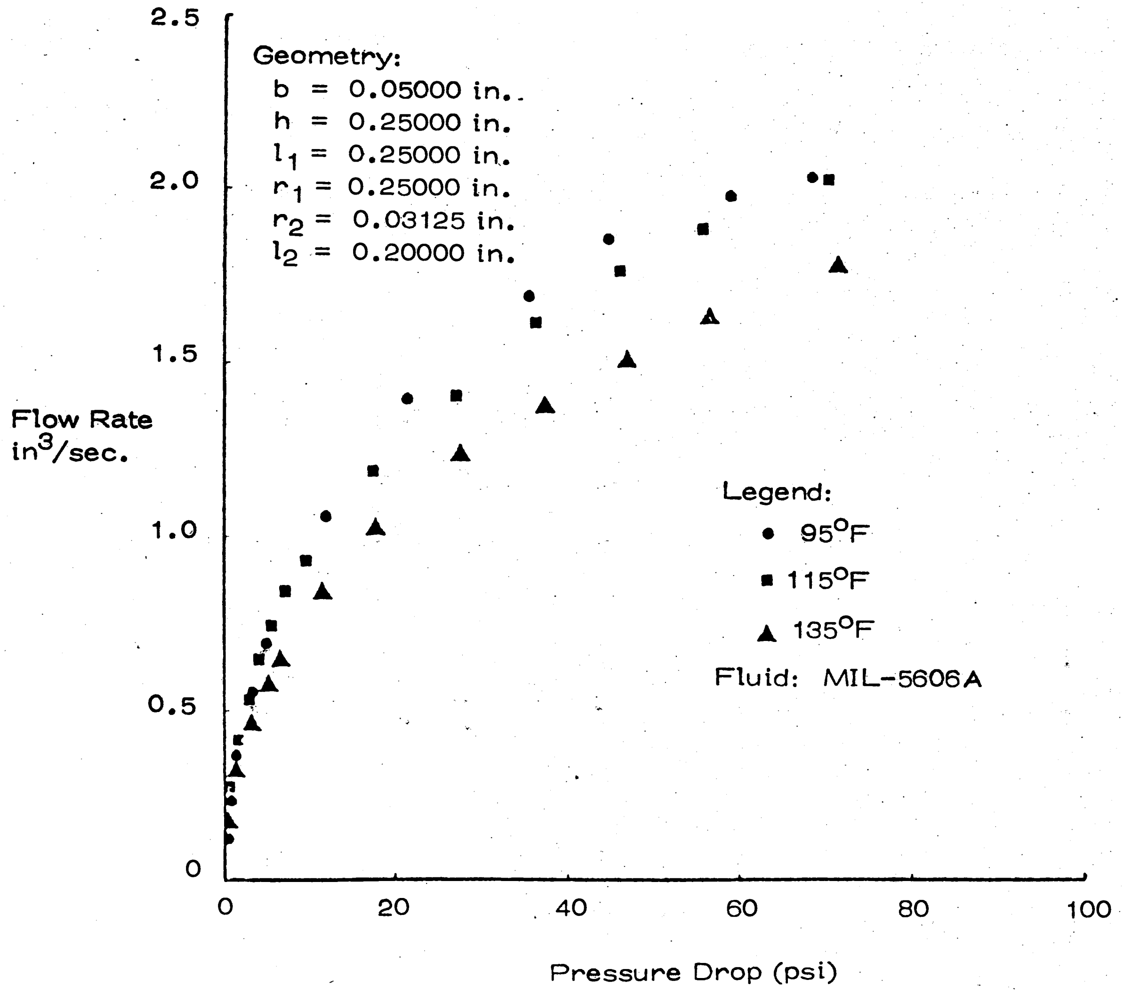

Figure 5. Measured Steady-State Characteristics of a NSVR With a Positive Temperature Sensitivity

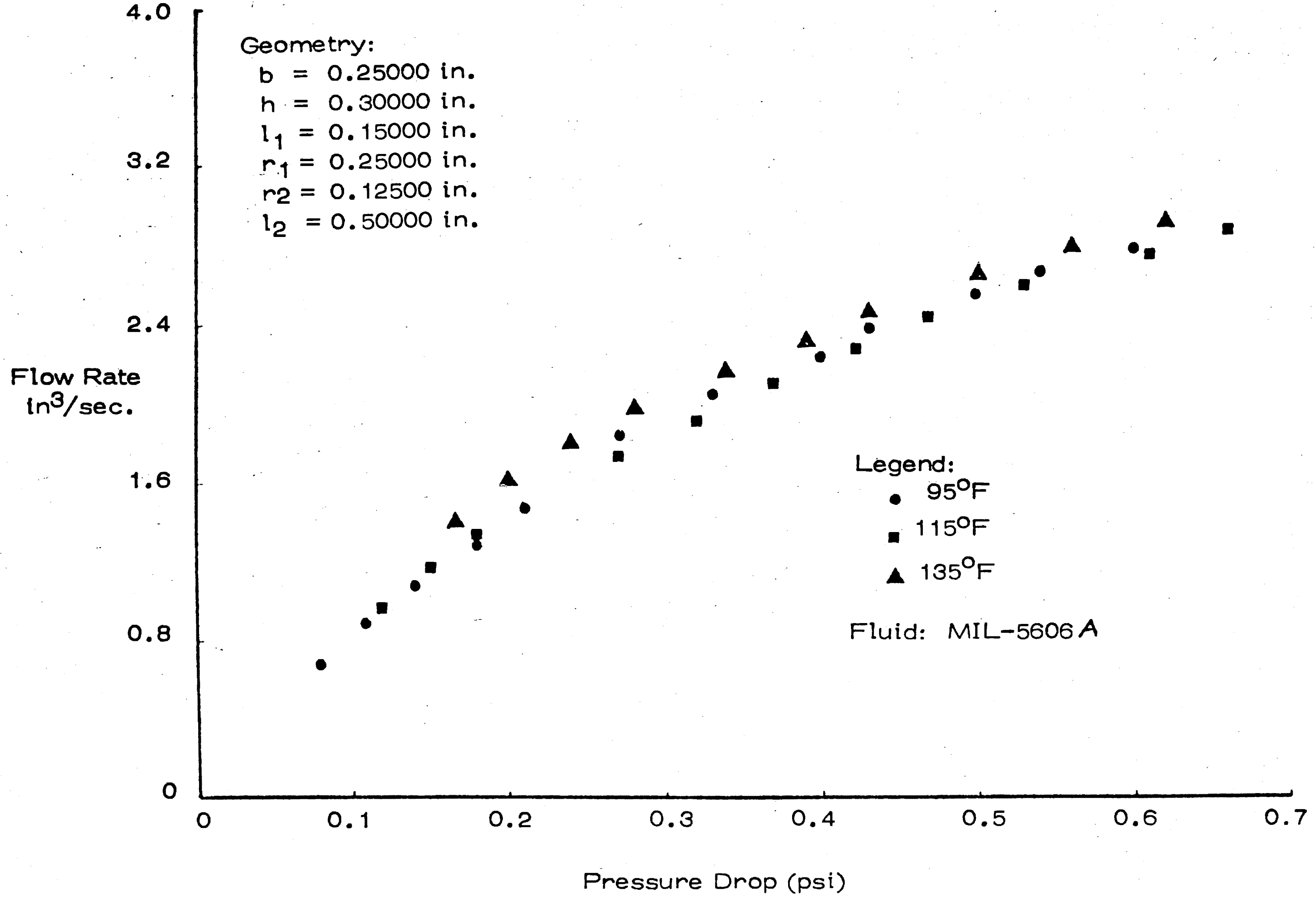

Figure 6. Measured Steady-State Characteristics of a NSVR With a Small Negative Temperature Sensitivity

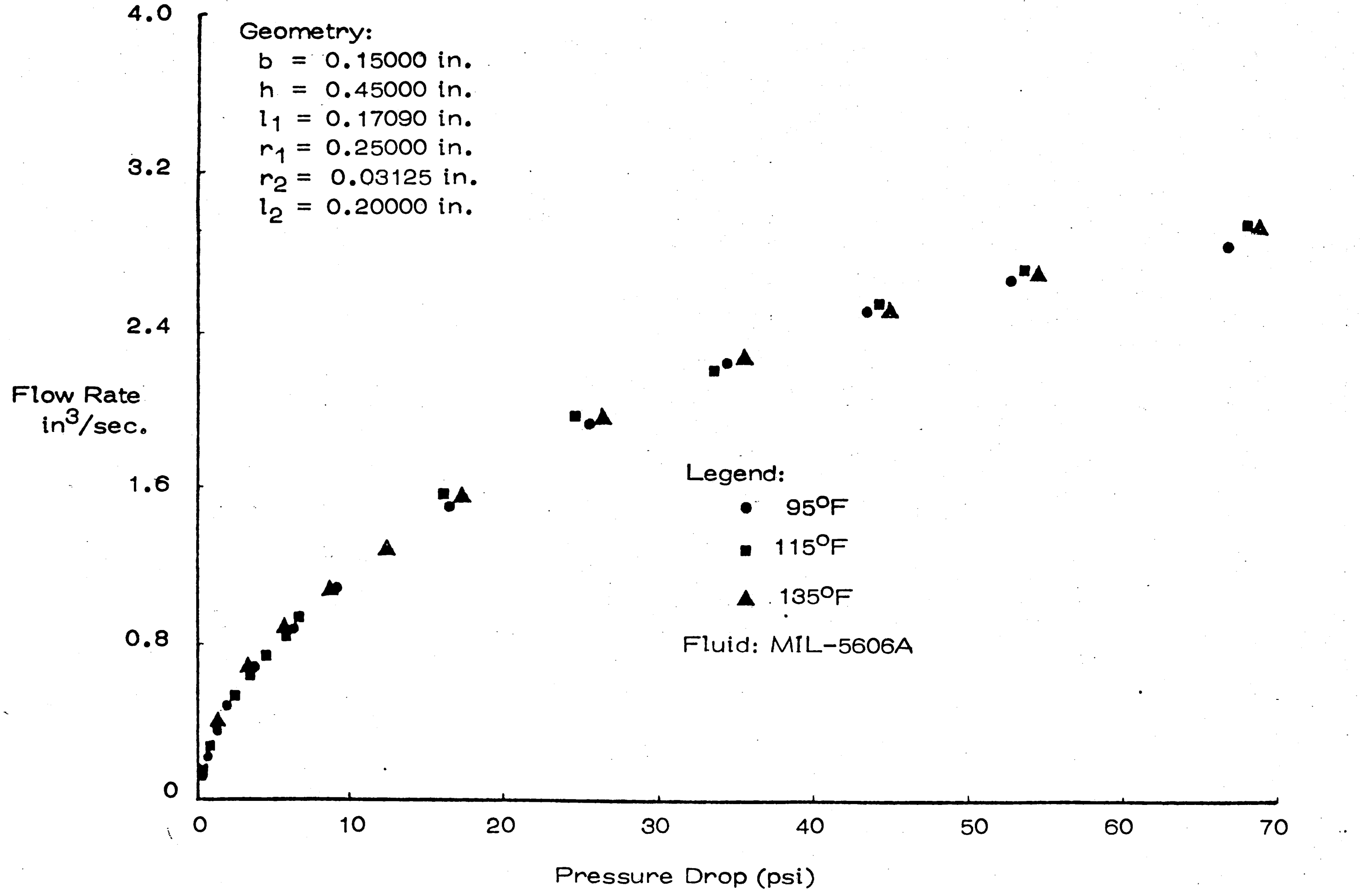

Figure 7. Measured Steady-State Characteristics of a NSVR With Negligible Temperature Sensitivity

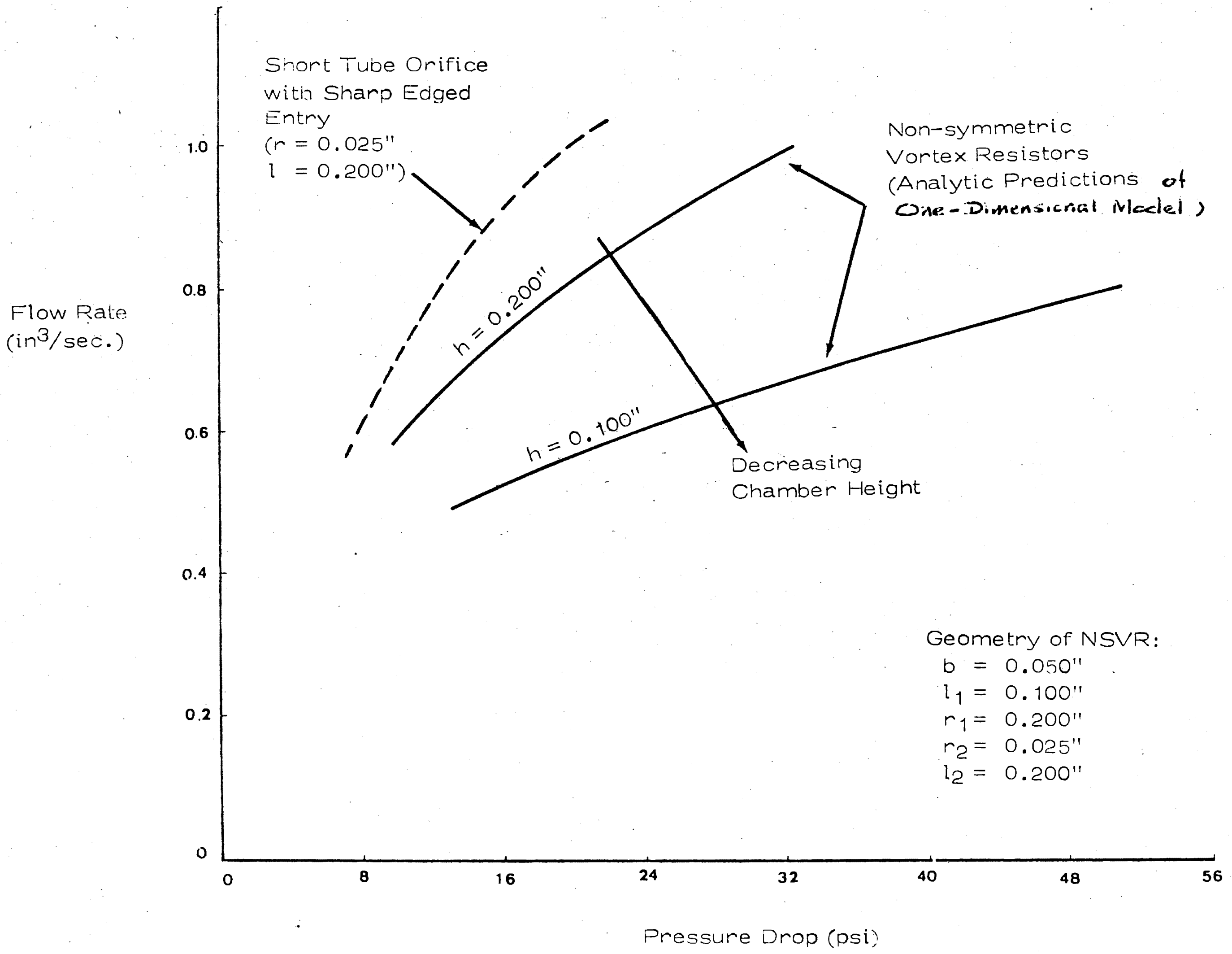

Figure 8. Typical Predicted Steady-State Characteristics of Non-Symmetric Vortex Resistors and a Comparable Short-Tube Orifice for Constant Temperature Operation

Secondary objectives were to demonstrate the feasibility of designing (1) a temperature-insensitive vortex resistor, and (2) a temperature-sensitive vortex resistor which can compensate for the temperature sensitivity of a conventional fluid resistor.

The study was limited to the following specific tasks:

1. Development of steady-state empirical models for the two basic types of vortex resistors.
2. Development of approximate analytical models for the two types of the vortex resistors.
3. Determination of maximum and minimum steady-state temperature sensitivities for a set of geometrical configurations which cover the expected practical range.
4. Development of an approximate dynamic model for the non-symmetric vortex resistor.

I.3. Summary of Results

An empirical model has been developed for the NSVR configuration (for flow in the high resistance direction). Experimental data taken on 24 different geometries and at temperatures of 95°F to 135°F (with MIL-5606A hydraulic oil) have been used in the model development. The model predictions exhibit a maximum error* of 30 percent over the range of the experimental data.

Empirical models have also been developed for the NSVR configuration with flow in the low resistance direction, and for the SVR configuration. These models have been developed by using only a limited

---

*Error = 100 x (experimental Q - predicted Q)/Experimental Q, at a given ΔP.

amount of data (8 geometries). Their usefulness is correspondingly limited.

Approximate analytical models have been developed for the symmetric and non-symmetric vortex resistors. Two steady-state analytical models, one incorporating a one-dimensional and the other a two-dimensional approximation to the flow field in the vortex chamber, have been developed for the non-symmetric vortex resistor. A one-dimensional model has been developed for the symmetric vortex resistor configuration. These models exhibit a maximum error of 15 percent of reading over the range of the experimental data measured.

The feasibility of designing temperature-insensitive and compensating vortex resistors in practical sizes has been established. (Compensating vortex resistors cancel the temperature sensitivity of conventional fluid resistors.)

Temperature sensitivities ranging from +0.00004 in.^{3}/sec.-°F (almost zero) to -0.0069 in.^{3}/sec.-°F have been measured with the available vortex resistor configurations. The temperature sensitivity of a comparable short-tube orifice is of the order of +0.005 in.^{3}/sec.-°F.

A linearized dynamic model based on a one-dimensional flow approximation has been developed which incorporates implicitly a pure time delay and a first order lag. The model can be used to predict the response of the resistor output pressure to step (with finite rise time) changes in the input pressure. Analytical predictions are in fair agreement with the experimentally observed dynamic responses.

Transient responses to a terminated-ramp input measured on a typical geometry indicated that the rise time is 13 milli-seconds. The predicted rise time using the analytical model is 9 milli-seconds.

CHAPTER II

LITERATURE SURVEY

The concept of the NSVR (or vortex diode) was originated by Dieter Thoma [1]*, and the SVR configuration was first used by the Lee Company [2] in the design of their "Lee Visco Jet." No analytical studies (in the laminar regime) of the SVR have been reported in the open literature. With the exception of reference [3], wherein Paul has obtained order-of-magnitude estimates for the NSVR performance, no analytical studies have been reported. The vortex and diffuser chambers (see Figure 4) have been studied separately as described in the sections below.

II.1. Vortex Flow

Vortex chamber studies have been motivated by applications in fluidics and in meteorology. Four different techniques have been used in the past with varying degrees of success for characterizing and predicting the vortex flow field. These techniques are:

(1) Similarity solutions,

(2) Momentum integral solutions,

(3) Finite difference solutions,

(4) Empirical approaches.

---

*Numbers in brackets refer to the references in the Bibliography.

Similarity solutions for a potential vortex flow over a stationary flat plate have been obtained by Kidd and Farris [4], and Hoffmann [5]. A numerical search is required to solve the two-point boundary value problem resulting from the similarity solution approach. It has been demonstrated in references [4 and 5] that the convergence time becomes too large for tangential Reynolds numbers greater than 4.75. Tangential Reynolds numbers for the SVR and the NSVR are expected to be of the order of a few hundreds at normal operating conditions. Hence a similarity solution technique in the existing form does not seem feasible.

Von Kármán's integral technique [6] (commonly called the momentum integral technique) is an approximate approach. In this approach, the partial differential equations describing the flow field are reduced to ordinary differential equations by integrating along one of the two independent space variables. This integration (commonly performed along the axis of the vortex) requires velocity profiles in functional forms. Two different approaches have been employed to obtain reasonable velocity profile functions. The first approach involves the concept of Prandtl's boundary layer. Velocity profile functions are developed on the basis of physical insight into the problem, as was originally done by Von Kármán. The second approach due to Boyack and Rice [7], assumes a general polynomial form for the velocity profiles without requiring any apriori knowledge of the flow field. In this respect, the second approach is superior to the first one but it tends to be computationally inferior due to the larger number of differential equations involved in the model.

The analyses of Rott and Lewellen [8], Wormley [9], and Kwok, Think and Lin[10], are based on the first momentum integral approach.

Rott and Lewellen's model [8] is a general one applicable to both laminar and turbulent flow regimes. Zero radial velocity is assumed in the core (i.e., the space between the top and bottom boundary layers of the vortex chamber) in order to produce a simplified model amenable to a closed-form analytical solution. Wormley [9] removed this restriction by including a developing flow region in which the radial velocity in the core is allowed to be different from zero. Wormley's model is valid for operation in the turbulent regime; it cannot be used directly for modeling the SVR and the NSVR for operation in the laminar regime. But, Wormley's basic approach can be utilized by including laminar shear stresses and velocity profile functions which are appropriate for the laminar regime.

A more approximate form of the momentum integral approach, as applied to vortex flow, is the "one-dimensional" approach. In this approach, the velocity profiles are assumed to be uniform. Closed form solutions based on the one-dimensional approach have been obtained by Taplin [11], and Bichara and Orner [12]. Taplin [11] treated the tangential velocity as a known function of the radial distance. Bichara and Orner [12] developed a more general model (turbulent regime) by calculating the radial distribution of the velocities using appropriate equations. This latter approach is highly efficient, and can be extended for use in the laminar regime. But, the results should be expected to have limited validity due to the velocity profile assumption.

The availability of high speed electronic computers with relatively large storage capacities makes finite-difference methods of solving partial differential equations more attractive. A recent application of this approach related to the vortex flow problem was presented by Farris et al. [13]. The computational times reported in reference [13] indicate that the state-of-the-art in this area of numerical computation has not yet reached a reasonable level of practicality.

Very few empirical or "black-box" studies of the vortex flow problem have been reported in the literature. The most relevant here is the empirical study of the vortex amplifier by Hondour and Rezek [14]. The important effect of viscosity variation of the hydraulic oil (due to temperature changes) was not included in this model however. Since the vortex amplifier characteristics are strongly influenced by viscosity variations, the model presented in reference [14] is of limited use.

Studies conducted on vortex rate sensors are not pertinent to the study of the SVR or the NSVR due to the significant differences in the associated flow fields observed in these two classes of devices. The Rossby number (ratio of radial to tangential velocity) is very large (much greater than unity) for a vortex rate sensor and it is of the order of 0.1 for the SVR and the NSVR.

In summary, no efficient analysis technique has been reported which is directly applicable to the vortex chamber under normal operating conditions. An empirical study of the vortex chamber is feasible. An alternative semi-analytical approach is the one-dimensional approach of Bichara and Orner [12] with necessary modifications for operation in laminar regime. Yet another, but more difficult, approach is to adapt Wormley's momentum integral approach to the laminar flow case.

II.2 Orifice Flow

The axial flow through the central orifice in the vortex resistor is accompanied by a large swirl at the inlet induced by the flow in the vortex chamber (forward flow case). This swirl flow through the orifice resembles the swirl flow through nozzles used in swirl atomizers. The effect of swirl is to force a large portion of the fluid to the boundary layer on the cylindrical surface, and thereby increase the resistance to flow through the orifice. In the NSVR there is no swirl in the orifice when flow is in the "reverse" direction (i.e., low resistance direction).

Taylor [15] and Weber [16] have studied the swirl flow through nozzles using the momentum integral approach. It is possible to adapt this approach for analyzing the central orifice in the vortex resistor. But, the resulting model would significantly increase the complexity of the overall model of the vortex resistor. A simple model (essentially one dimensional) which takes into account the effect of swirl in the orifice has been developed by Bichara and Orner [12]. Since the inlet conditions for the orifice are not exactly the ideal conditions used in the more sophisticated approach of references [15 and 16], it appears more reasonable to use the approximate but efficient model of reference [12].

The vortex resistor rectangular cross-section orifices (i.e., the inlet orifice for the NSVR and the inlet and outlet orifices for the SVR) and circular cross-section central orifice, can be modeled as short-tube orifices with sharp-edged entries. The coefficient of discharge reported by Lichtarowicz, et al. [17] and Reid [18] can be used for predicting the flow characteristics of these orifices.

II.3 Diffuser Flow

The diffuser chamber in the case of the NSVR is a sudden expansion section. This chamber can be modeled with reasonable accuracy by means of a one-dimensional momentum equation approach. The diffuser chamber of the SVR is characterized as a decelerating vortex flow (counter-rotating with respect to the inlet vortex chamber); the corresponding flow field is exceedingly complex.

Radial diffuser flows have been studied both analytically and experimentally by Jansen [19 and 20]. His analyses are based on a momentum integral technique. The flow field in the radial diffuser is assumed to be symmetric about a mid-plane, with good accuracy. But, the flow field in the diffuser chamber of the SVR is dominantly anti-symmetric and resembles the flow field on one side of an enclosed rotating disc. Therefore, Jansen's results cannot be used for the vortex resistor case.

There is no published literature on the analysis of the flow field in a diffuser chamber such as that in an SVR. But, the rotating disc studies can serve as a guide. Analytical and experimental studies of an enclosed disc were originally conducted by Daily and Nece [21]. Recently Miloh and Poreh [22] have extended the analysis to non-Newtonian fluids. The analysis involves consideration of two boundary layers, one on the rotating disc and the other on the stationary casing. Rigid body rotation is assumed for the core and a momentum integral approach is used to solve for the flow field. These analyses do not include through-flow. The basic approach of Daily and Nece can be extended to the diffuser chamber of the vortex resistor. Alternatively, one-dimensional approach, similar to the one of reference [12], can be used to approximate the complex flow field existing in the diffuser chamber of the SVR.

II.4. Vortex Dynamics

No analytical or experimental results have been reported in the open literature concerning the dynamical behavior of SVR and NSVR elements. However, some work has been done on the dynamics of fluidic vortex amplifier and vortex rate sensors.

The vortex rate sensor has a low swirl component whereas a NSVR inherently has a large swirl component. Results of dynamic studies of vortex rate sensors [23, 24, 25] appear to be of limited value in understanding the dynamical behavior of vortex resistance elements.

Duff, et al. [26] and Knapp [27] have measured the dynamic response of a vortex valve, but no attempt has been made to analytically predict the response. Taplin [28] has derived an analytical model for small-signal operation of a vortex amplifier. His "one-dimensional model" includes a time delay T_1 and a first order lag T_2 to characterize the vortex chamber dynamics. The propagation of tangential velocity from the outer edge of the vortex chamber to the exit orifice gives rise to the pure time delay T_1. For inviscid flow, T_1 equals the chamber fill time. But, due to viscous effects, the flow is contained largely in the boundary layer on the top and bottom surfaces of vortex chamber. This tends to reduce the effective chamber volume (see reference [29]). Taplin [28] used one quarter of the chamber fill-time as the time delay. The second time constant T_2 arises from the inertia of the core between the two boundary layers. Again one quarter of the chamber fill-time was used by Taplin [28] for T_2. In contrast, Bell [30] used $T_1 = 1/2$ the chamber fill-time for T_1 and $T_2 = 1.3$ times the chamber fill-time to match his experimental data. The empirical nature of the models used by Taplin and Bell is obvious.

To rationalize the choices of T_1 and T_2, Anderson [31] derived a distributed parameter dynamic model. The model was used to estimate the times T_1 and T_2. The resulting times were fractions of the chamber fill-time ranging from 0.2778 to 0.3648 for T_1 and from 0.6454 to 0.7647 for T_2 for the four cases studied by Anderson. Unlike Bell [30] and Taplin [28], Anderson does not predict a constant fraction of the chamber fill-time for T_1 and T_2. In this respect, Anderson's model is superior to the others. Experimental results confirm the validity of Anderson's approach.

Anderson's model is based in part on Wormley's steady-state model [9] which in turn uses turbulent shear stress terms. A major modification would be required in the Anderson model to make it useful in the dynamic characterization of the NSVR and SVR which typically operate in the laminar flow regime.

Although the previous dynamic studies have limited direct application to the vortex resistor problem, Taplin [28] and Bell [30] suggest a model form for describing the vortex chamber dynamics. That is, a model form which includes a pure time delay and a first order lag agrees reasonably well with experimental data.

CHAPTER III

STEADY-STATE EMPIRICAL MODELS

In cases where fluid systems involving a large number of elements are to be simulated, it is often desirable to use simple mathematical models for the elements in order to maximize computational efficiency. The empirical models developed here for symmetric and non-symmetric vortex resistors are single algebraic equations which contain experimentally derived coefficients. They are computationally efficient for preliminary design calculations but limited in their range of application by the available data base. More accurate analytical models are developed in Chapter IV which consist of sets of algebraic/differential equations; these models are applicable over a wide range of geometrical and operational conditions, but they require the use of a digital computer in performing analysis and design calculations.

III.1. Model Form

The empirical models developed in this study are similar in functional form to the vortex amplifier model developed by Hondour and Rezek [14] except that the effect of viscosity is included here. The steady-state characteristic of a vortex resistor is assumed to be of the form

$$\frac{r_1^4 \Delta P}{\rho Q^2} = a_1 \left(\frac{b}{r_1}\right)^{a_2} \left(\frac{h}{r_1}\right)^{a_3} \left(\frac{l_1}{r_1}\right)^{a_4} \left(\frac{r_2}{r_1}\right)^{a_5} \left(\frac{l_2}{r_1}\right)^{a_6} \left(\frac{Q}{r_1 \nu}\right)^{a_7} \tag{1}$$

where the a's are constants which are computed by linear regression using experimental data. The form of Equation (1) is consistent with that normally used in analyses and data correlations for orifice type resistors.

III.2. Experimental Apparatus and Procedure for Measurement of Steady-State Characteristics

Figure 9 shows a schematic of the experimental apparatus used to obtain steady-state characteristics for vortex resistors over a range of geometrical and operational conditions. These data were used to determine the constants in Equation (1) and to validate the one-dimensional and two-dimensional models presented in Chapter IV. A Vickers hydraulic piston pump rated at 5 gpm (at 1500 psig) provided the fluid power source. The operating fluid was MIL-5606A hydraulic oil. A chromalox coil-type immersion heater (of 10 kW capacity) was used for heating the hydraulic oil (95° - 135° F). A feedback temperature controller was used to maintain the oil temperature constant at any desired value above the room temperature. Figure 10 is a photograph of the test stand and primary instrumentation.

III.2.1. Resistor Block

The vortex resistor block was of laminated construction. Figure 11 shows parts of the NSVR assembly. Tapped holes in the top and bottom allowed mounting of the pressure gauges and thermocouples very near the effective inlet and exit of the resistor. Locating-pins were used in accurately drilled holes to insure proper alignment of the laminates.

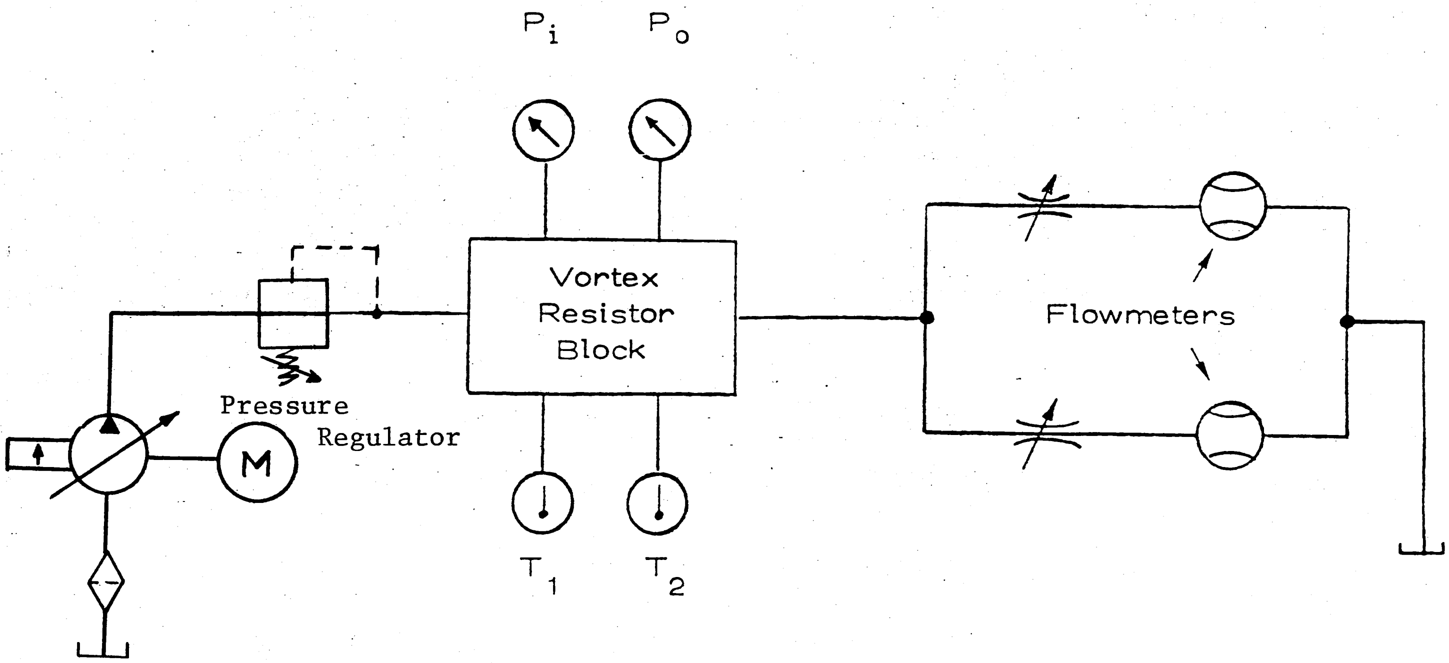

Figure 9. Schematic of Experimental Apparatus for Measurement of Steady-State Characteristics

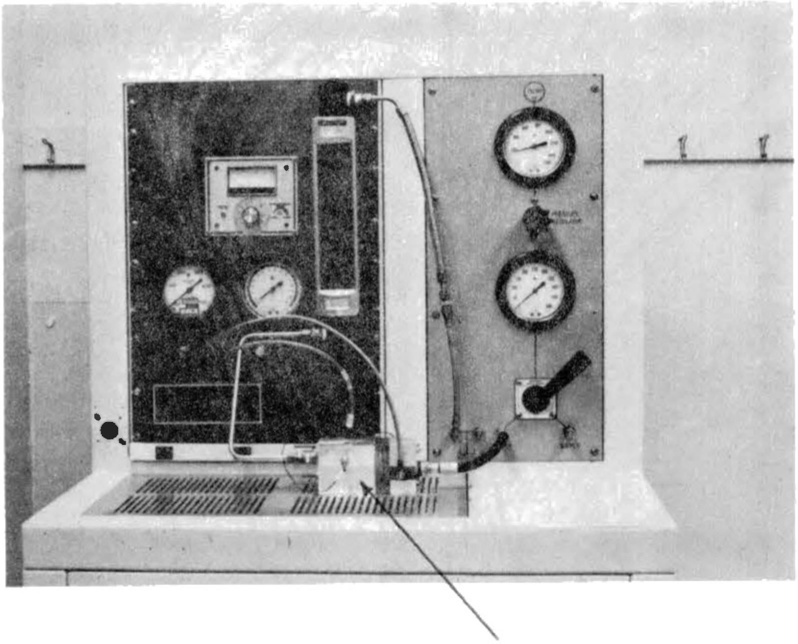

Figure 10. Photograph of the Test Stand and Primary Instrumentation

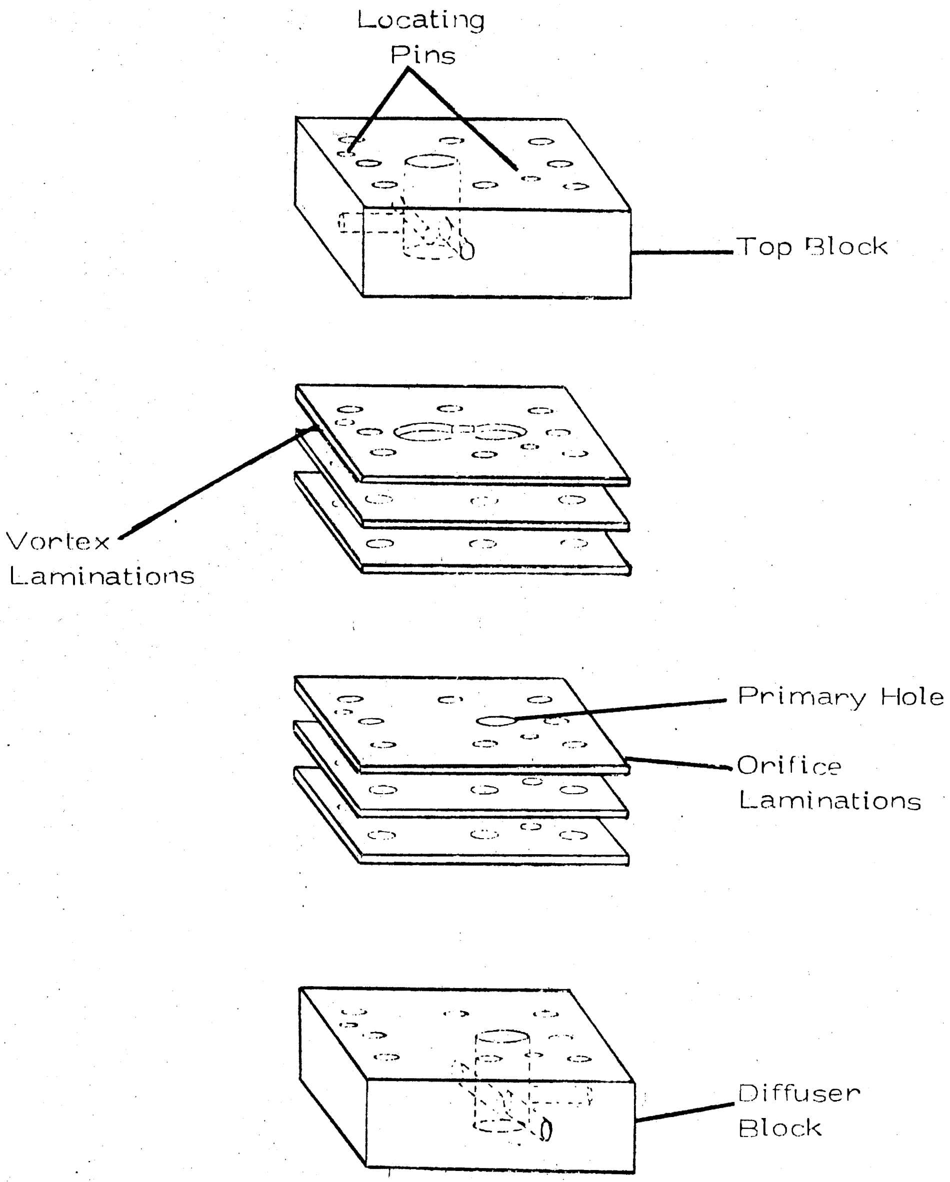

Figure 11. Laminated Construction for the SVR

Figure 11 shows the vortex chamber orifice and diffuser laminations used for the SVR configuration. (The vortex chamber and diffuser chamber laminations are identical.) For the non-symmetric configuration or NSVR, no diffuser laminations were used. The end block of the NSVR contained a sudden expansion diffuser aligned with the central orifice as shown in Figure 12. Figure 13 is a photograph showing the various parts of the NSVR assembly.

Table I lists the various sets of laminations used in this study. Sets 1 and 2 were made by Air-Research Corporation. Sets 3 and 4 were designed and constructed at OSU. Sets 1 and 2 were made from steel and were copper plated. Set 3 was made of brass and set 4 of plexi-glass. In sets 1 through 3, surfaces in contact were sufficiently smooth and the clamping force during assembly was large enough to result in negligible leakage between the laminations. Rubber O-ring seals were used with set 4 laminations to eliminate leakage. Different end blocks were used for the four sets of laminations due to their different geometric scales. Different overall resistor geometries were assembled from sets 1, 2, and 3. The height of the vortex chamber (and diffuser chamber in the case of the SVR) and the length of the central orifice were conveniently varied by the number of laminations used.

III.2.2. Instrumentation

The following quantities were measured:

1. Inlet and outlet static pressures,
2. Volumetric flow rate through the resistor,
3. Temperature of the hydraulic oil.

Bourdon-tube type pressure gauges were used to measure the static

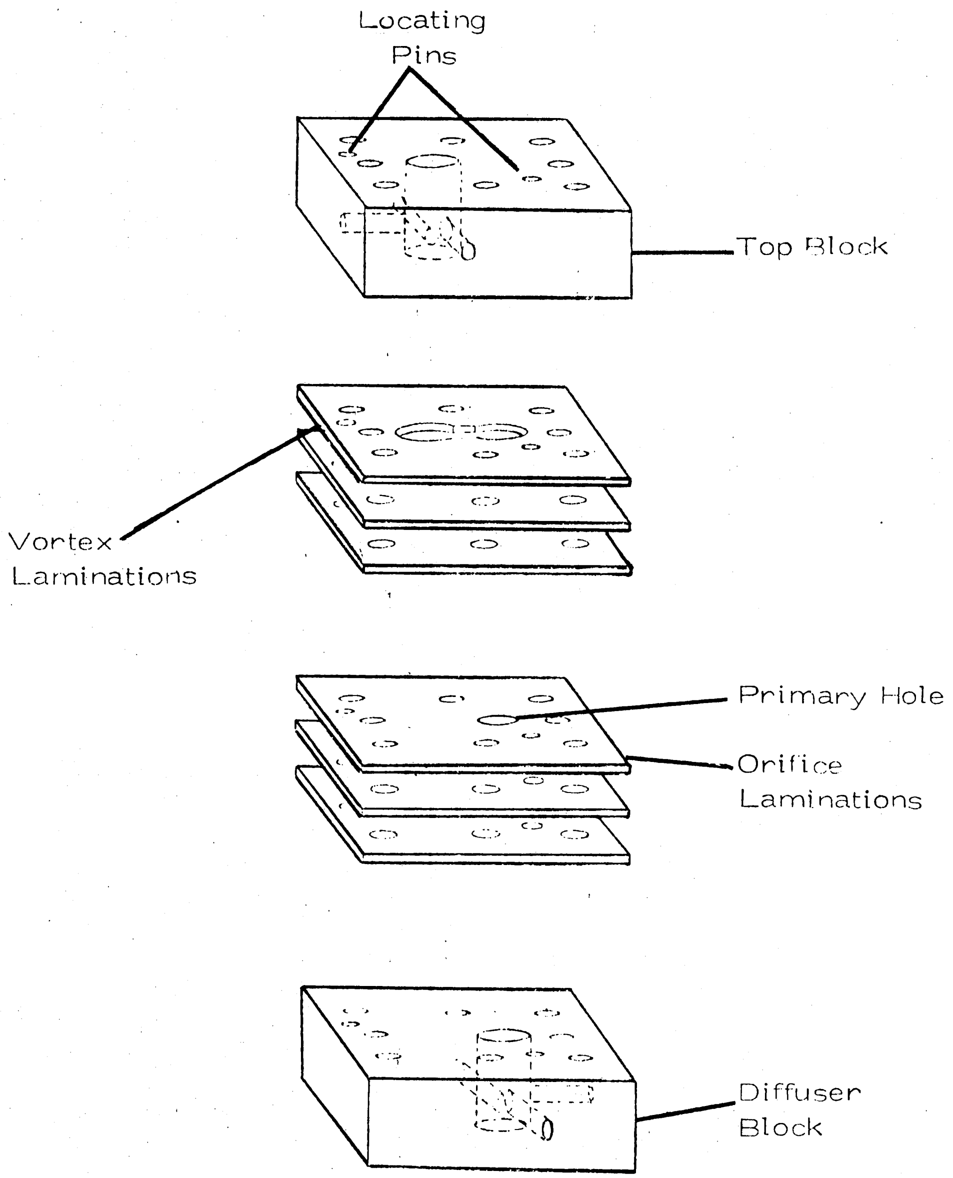

Figure 12. Laminated Construction of the NSVR

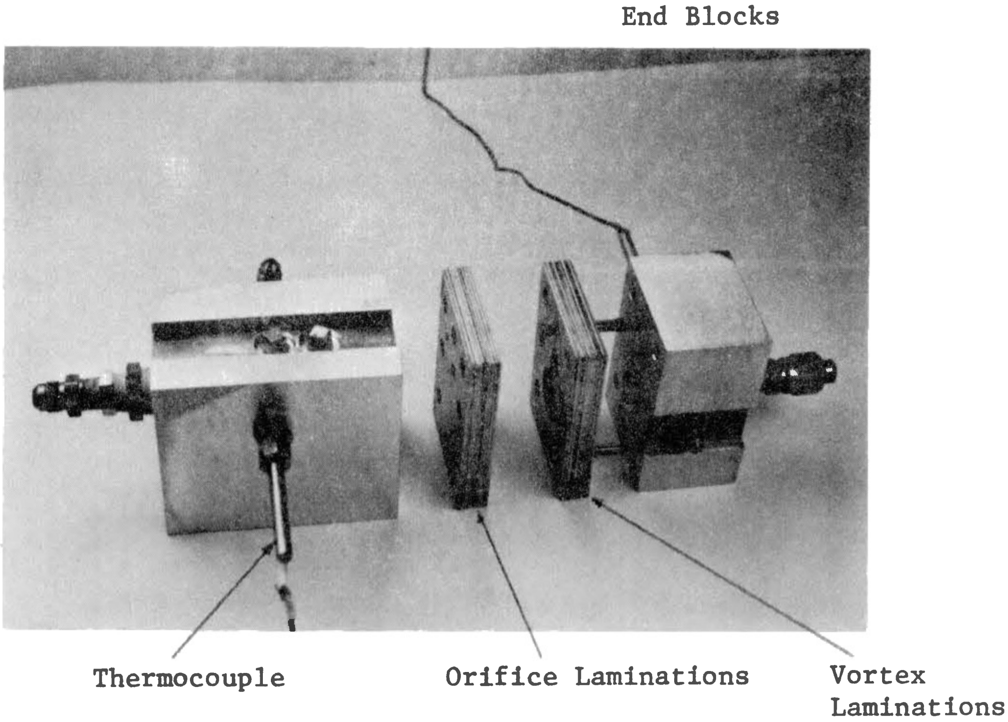

Figure 13. Exploded View of the NSVR Block Assembly

TABLE I

GEOMETRY OF LAMINATIONS USED IN THE STEADY-STATE STUDY

Set No.	Width b inch	Length of Inlet Orifice l_1 inch	Thickness per Lamination inch	Vortex Chamber Radius r_1 inch	Orifice Radius r_2 inch	Maximum Number of Laminations Used	Remarks
1	0.03280	0.09525	0.010	0.08955	--	8	Four geometries were tested for SVR from these laminations
	--	00	0.010	--	0.03475	5	
2	0.02845	0.29795	0.006	0.13630	--	20	Twelve geometries were tested for SVR and NSVR (both high and low resistance flow directions) from this set.
	0.03675	0.28650	0.006	0.14195	--	20	
	0.04775	0.22700	0.005	0.14171	--	10	
	--	--	0.010	--	0.06000	7	
3	0.05000		0.050	0.25000	--		24 geometries were tested for NSVR from this set of laminations (in high resistance flow direction).
	0.10000			0.25000	--		
	0.15000			0.25000	--		
	0.20000			0.25000	--		
	0.25000			0.25000	--		
	--	--		--	0.06250		
	--	--		--	0.12500		
	--	--		--	0.14950		
	--	--		--	0.20100		
	--	--		--	0.25000		
4	0.25000		0.500	1.000	--	2	This set was made of plexi-glass and was primarily used in flow visualization study
	--	--	0.560	--	0.42500	1	

pressures in the range 0.5 psig and up. For pressures below 0.5 psig, strain-gauge pressure transducers were used for improved accuracy. The pressure gauges were calibrated with a dead-weight tester. The maximum error in pressure measurement was ± 0.2% of the full scale.

Fischer-Porter rotameter-type flowmeters were used to measure the volumetric flow rate. Three different flowmeters were used to cover the entire range of flow rate, i.e., 0.001 to 1 gpm. The flowmeters were calibrated with the actual operating fluid over the entire range of temperature operation. Maximum error in flow rate measurement was ± 0.4% of the full scale.

A Leeds and Northrup Numatron II temperature measurement system was used in conjunction with locally built Iron-Constantan thermocouples. The thermocouple elements were located in the end blocks of the vortex resistor. The flow sensitivities of the thermocouples were minimal (of the order of 1°F error for the total range of flow rate used) when they were located in the end block position shown in Figure 14. The overall error of the temperature measurement system was less than ± 1°F.

The temperature measurement system was calibrated by measuring the temperature of boiling water. Two thermocouples, one at the upstream and one at the downstream of the resistor, were used to determine the temperature difference across the resistor. By thermally insulating the resistor block the temperature difference in the worst case (at lowest flow rate) was ± 2.5°F. An average of the two temperatures was used as the temperature of the hydraulic oil for computational purposes.

III.2.3. Properties of MIL-5606A Hydraulic Oil

Density and viscosity were the only properties of the hydraulic oil

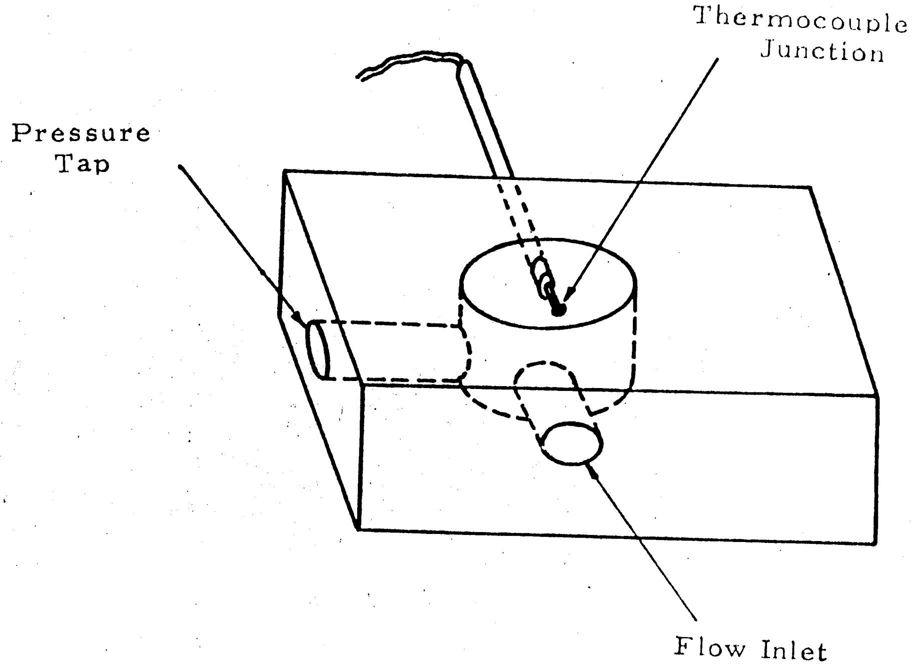

Figure 14. Location of the Thermocouple in the End Block

used in the analysis of the resistor. Properties data available from the literature (see Figures 15 and 16) were used for all calculations. The pressure dependence of viscosity and density was not included due to the relatively low operating pressure. Care was taken to remove all trapped air from the system by bleeding.

All measured steady-state data are presented in detail in reference [33]. Typical pressure drop-flow rate characteristics are shown in Chapter IV.

III.3. Empirical Correlations

Appendix A outlines the linear regression procedure used to obtain the model constants (a_i's of Equation 1 based on the measured data). Figure 17 shows a correlation for an NSVR with a radius ratio (r_2/r_1) of 0.299. Other parameters for this case are listed in Table III in Appendix A. The flow conditions ranged from $\frac{Q}{r_1 \nu}$ = 100 to 1000. The model agrees with the experimental data within 30 percent of reading.

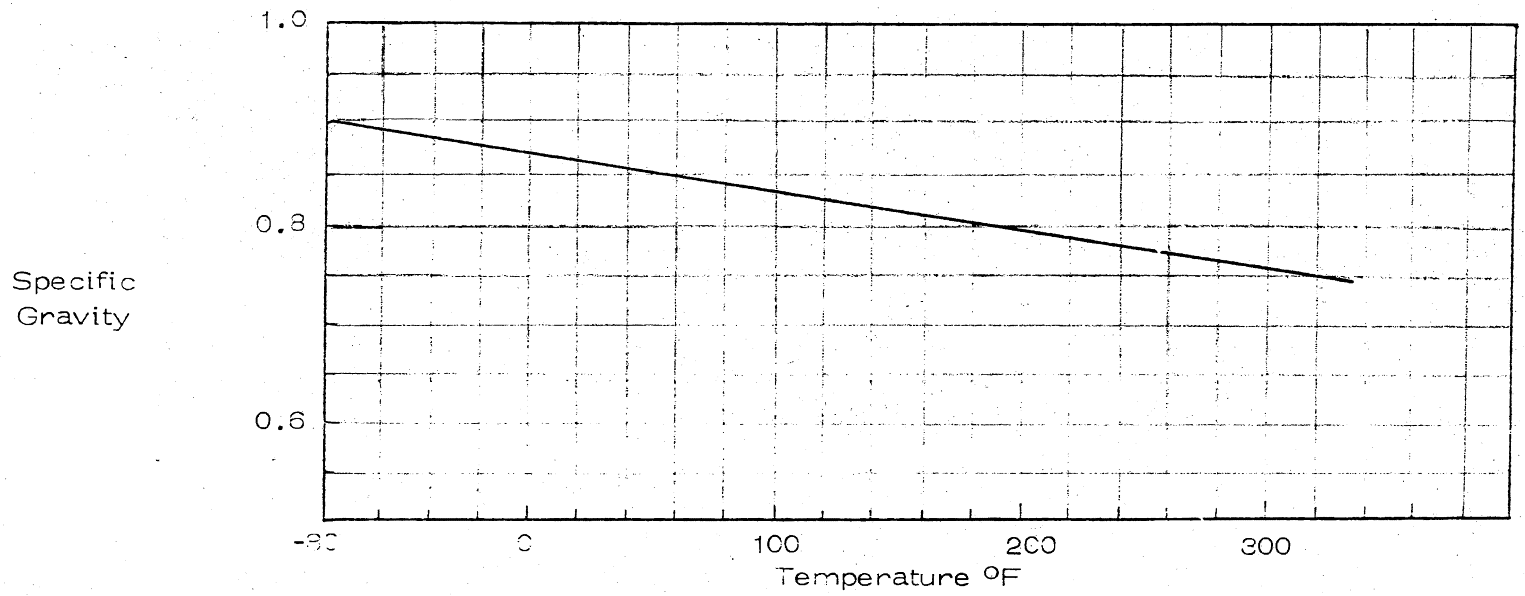

Figure 15. Specific Gravity of MIL-5606A as a Function of Temperature (See Reference [2])

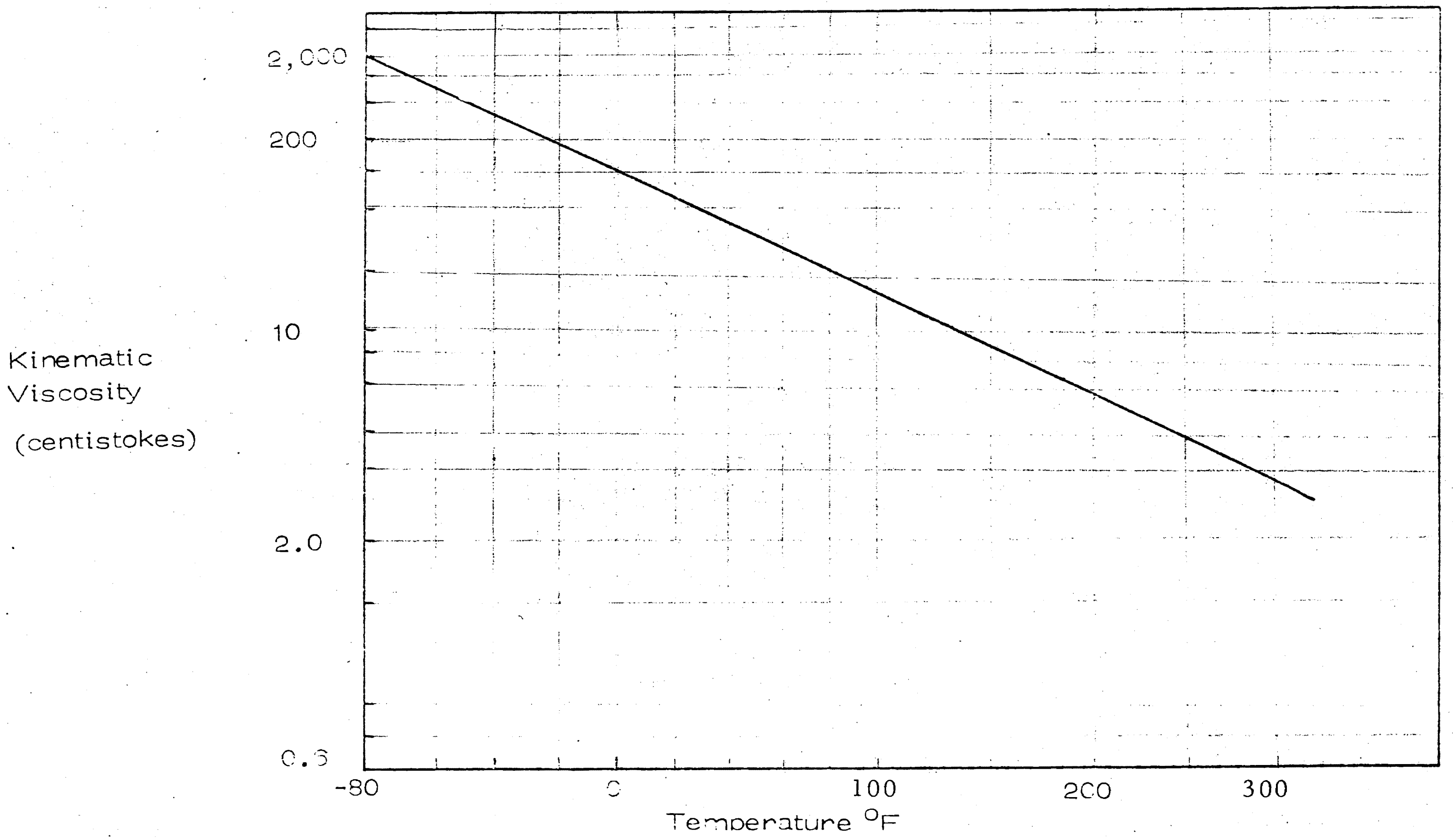

Figure 16. Kinematic Viscosity of MIL-5606A as a Function of Temperature (See Reference [2])

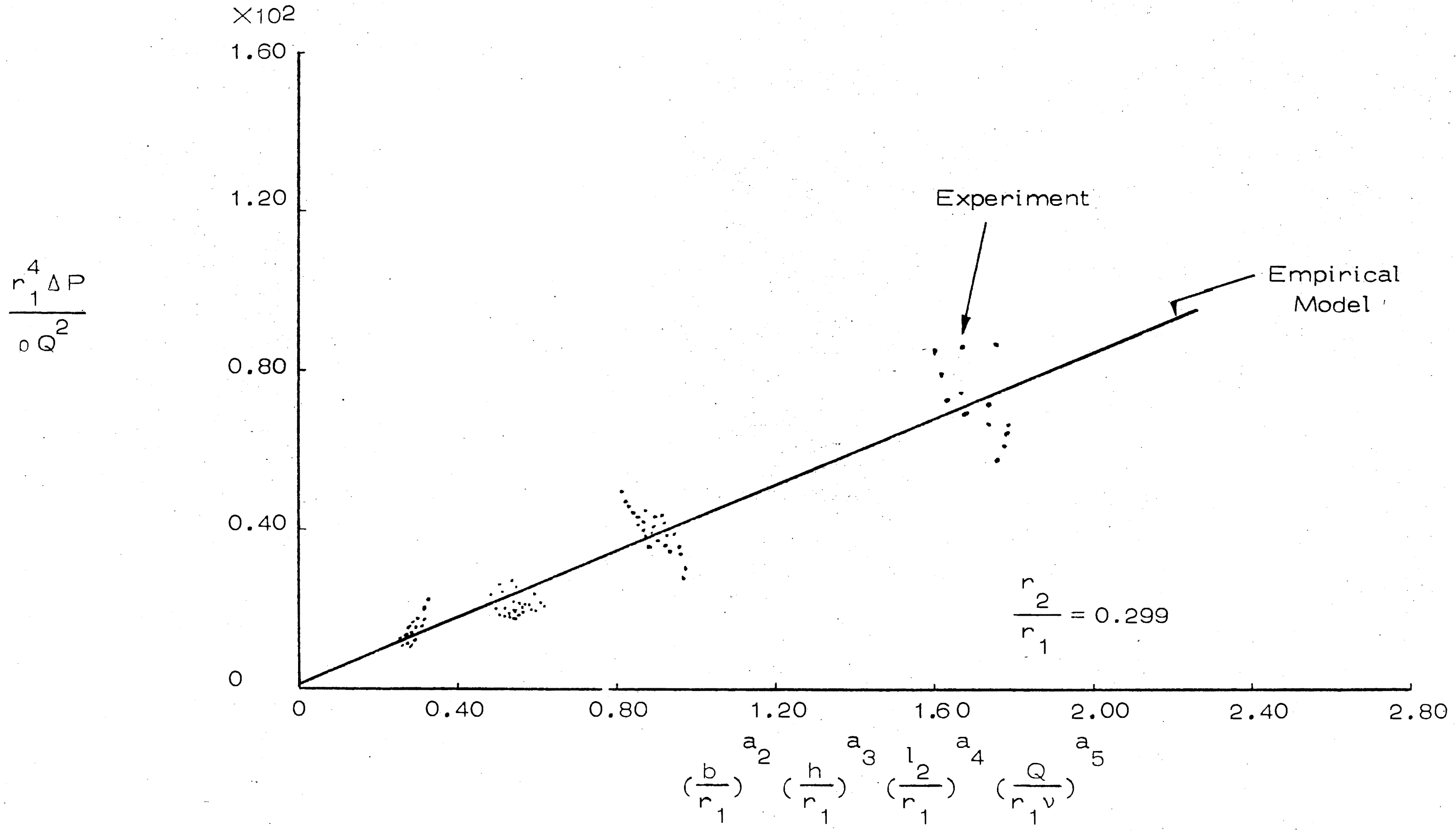

Figure 17. Empirical Model of A NSVR for Operation in the High Resistance Flow Direction

CHAPTER IV

STEADY-STATE ANALYTICAL MODELS

This chapter summarizes the development of approximate analytical models which predict the steady-state behavior of the two types of vortex resistors. The approach is to approximate the basic flow processes with simple and manageable functions. In the case of the vortex chamber (see Figure 4), the flow field has been relatively well described in earlier studies [9]. The flow field in the diffuser chamber of the SVR has not been studied and is difficult to visualize intuitively. A flow visualization study was conducted to identify the basic character of the flow field in the symmetric vortex resistor.

IV.1. Flow Visualization Study

A large scale plexi-glass model (2 inches outer diameter vortex chamber) run on water was used for the flow visualization study. Figure 18 shows the schematic of the experimental setup. Figure 19 shows an exploded view of the model with the dye-injection system. The first plate on the left carries an injector (inside the tube) which was used for introducing dye at different depths in the vortex chamber. The vortex chamber, central orifice and diffuser plates can also be seen in Figure 19. The flow conditions were maintained at a Reynolds number (based on the central orifice diameter) of 200 for all cases except that shown in Figure 27. For Figure 27, the Reynolds number was 500.

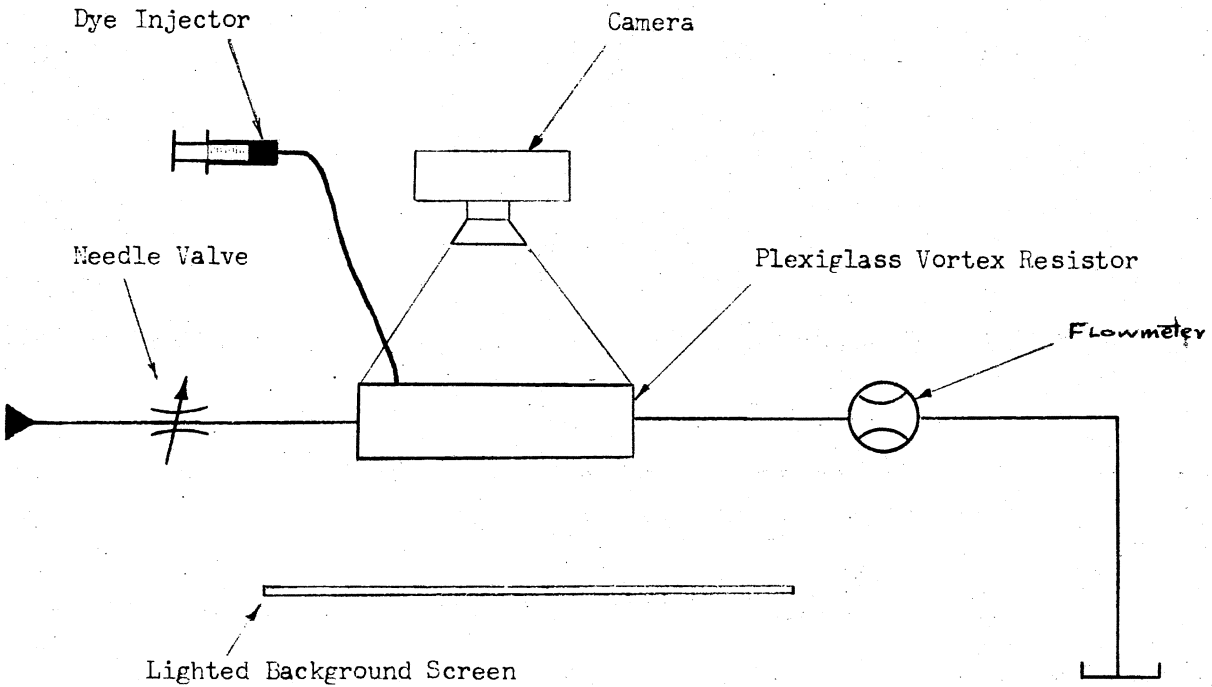

Figure 18. Schematic of Flow Visualization Apparatus

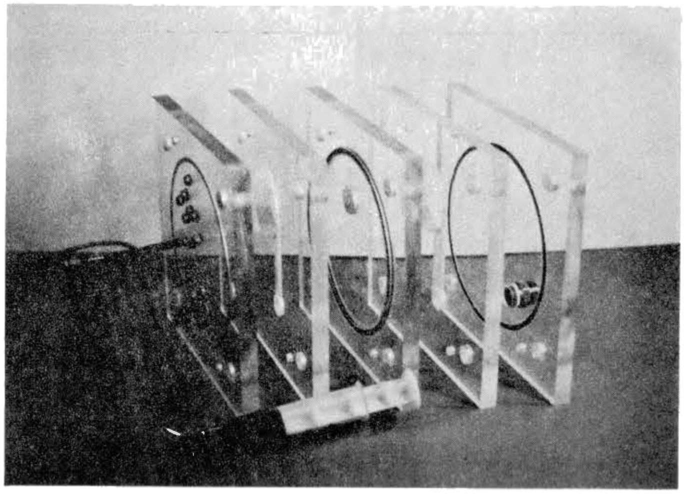

Figure 19. Plexiglass Model for Flow Visualization

IV.1.1. Vortex Chamber

Figures 20-23 show typical results from the flow visualization study of the vortex chamber. Figures 20 and 21 show the boundary layer flow. In the cases shown in Figures 22 and 23, dye was introduced into the core region. The dye streaks in these latter cases show the core flow with a relatively large tangential to radial velocity ratio. The streamlines appear to be disturbed due to the wake created by the injector.

IV.1.2. Diffuser Chamber

Figures 24-29 show the flow patterns in the diffuser chamber. In all cases the diffuser chamber was first filled with dye, and then water flow was initiated by opening the needle valve (see Figure 18). The flow patterns of Figures 24, 25, and 26 were observed in time succession. A spinning, tube-like flow pattern was observed during the test. (The spinning of the tube was about a toroidal axis [see Figure 30]). Figure 27 shows the flow pattern at a high Reynolds number. Figure 28 shows the reverse flow on the top surface of the diffuser chamber. Figure 29 shows the boundary layer flow along the annular wall and reverse flow on the top surface of the diffuser chamber. An attempt to photograph cases where dye was injected into the core region of the diffuser failed. The dye injected at various heights dispersed quickly without a stable pattern. The presence of the injector and the rate of injection disturbs the flow field strongly. Recirculation was observed in the core region of the orifice. Figure 30 shows schematically the overall flow field observed in the SVR.

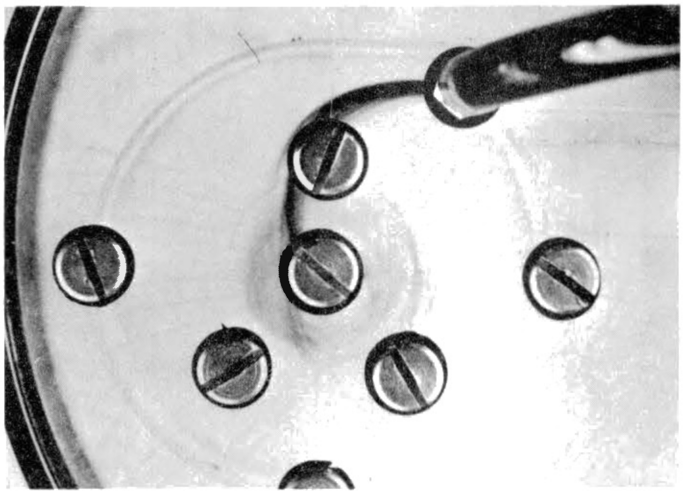

Figure 20. Boundary Layer Flow in Vortex Chamber

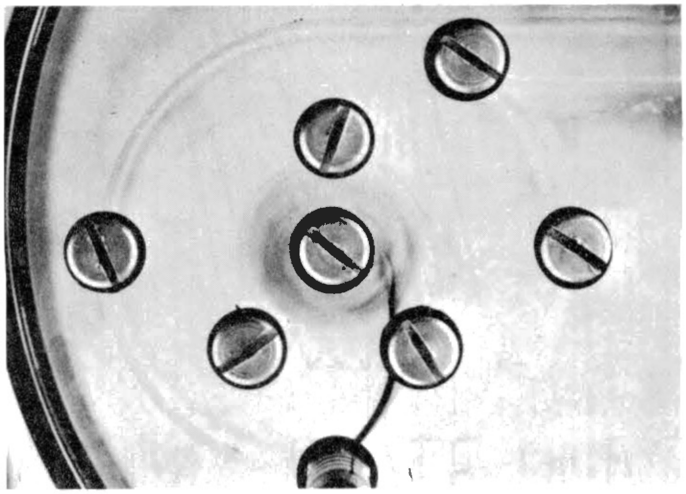

Figure 21. Boundary Layer Flow in Vortex Chamber

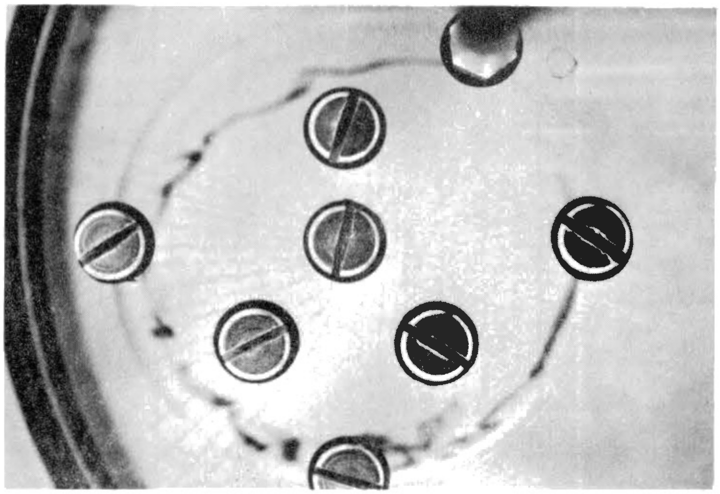

Figure 22. Core Flow in Vortex Chamber

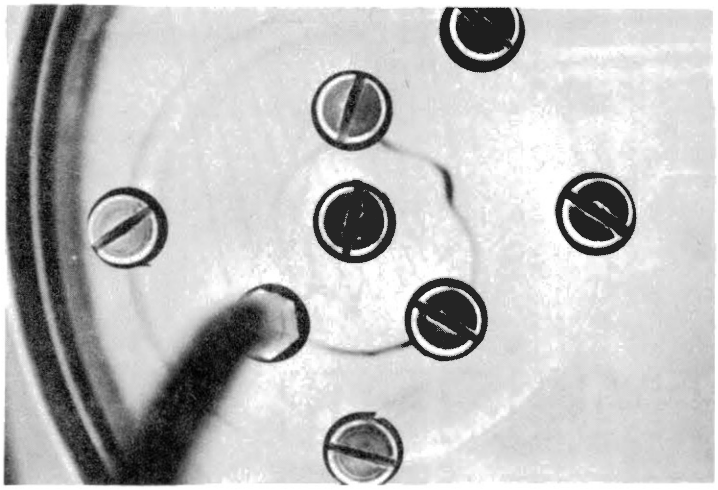

Figure 23. Core Flow in Vortex Chamber

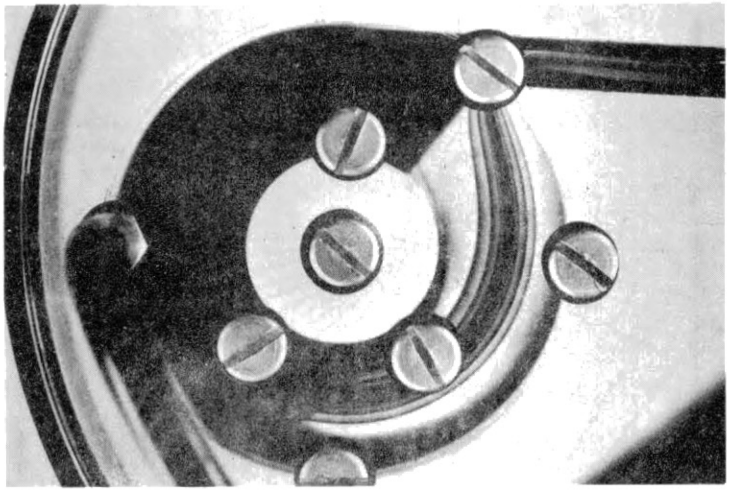

Figure 24. Flow Pattern in the Diffuser Chamber of SVR

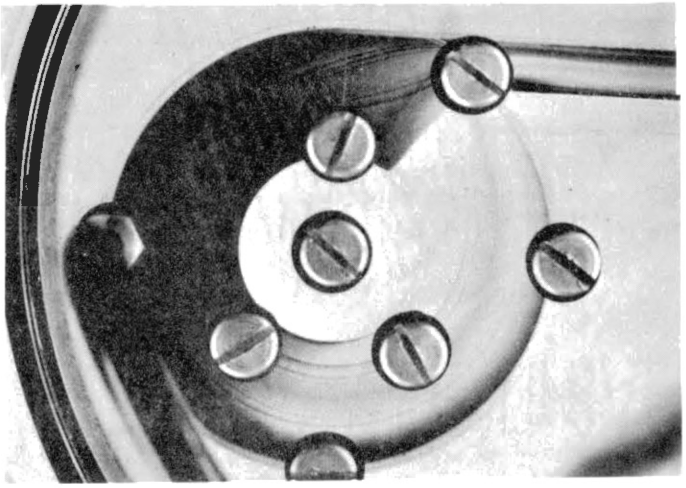

Figure 25. Flow Pattern in the Diffuser Chamber of SVR

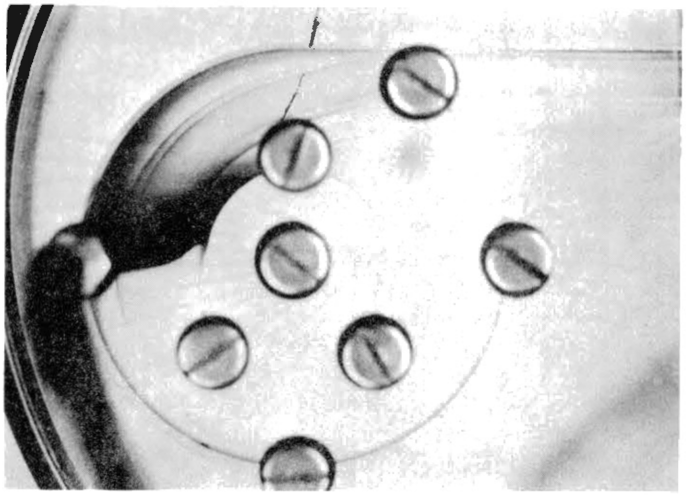

Figure 26. Flow Pattern in the Diffuser Chamber of SVR

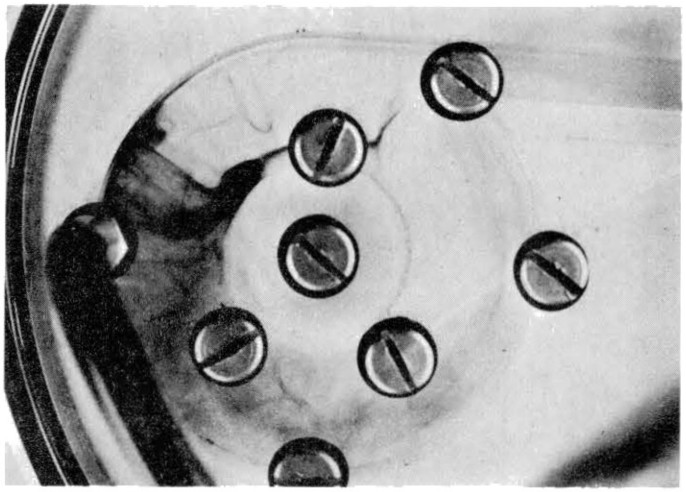

Figure 27. Flow Pattern in the Diffuser Chamber of SVR at a Reynolds Number of 500

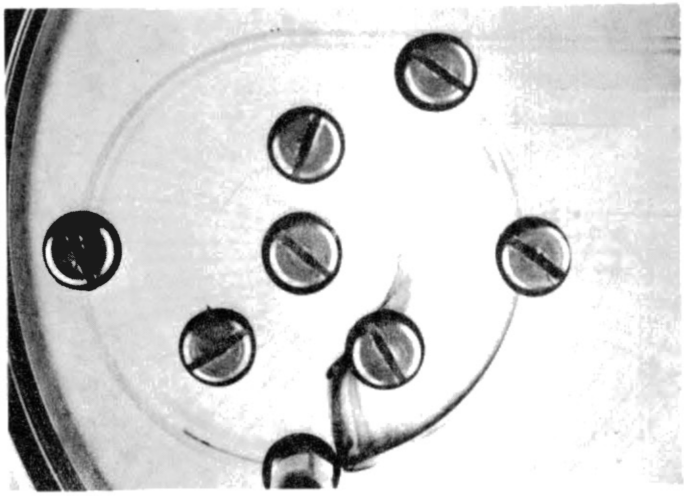

Figure 28. Reverse Flow in the Diffuser Chamber of SVR

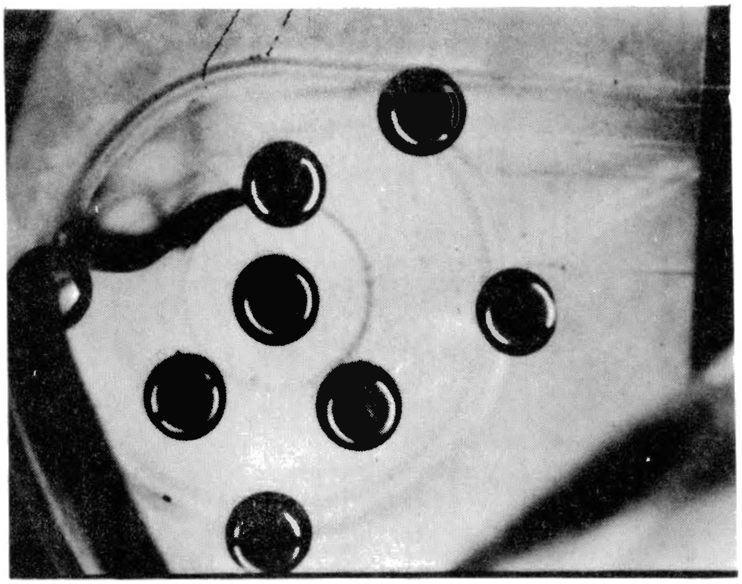

Figure 29. Reverse Flow in the Diffuser Chamber of SVR

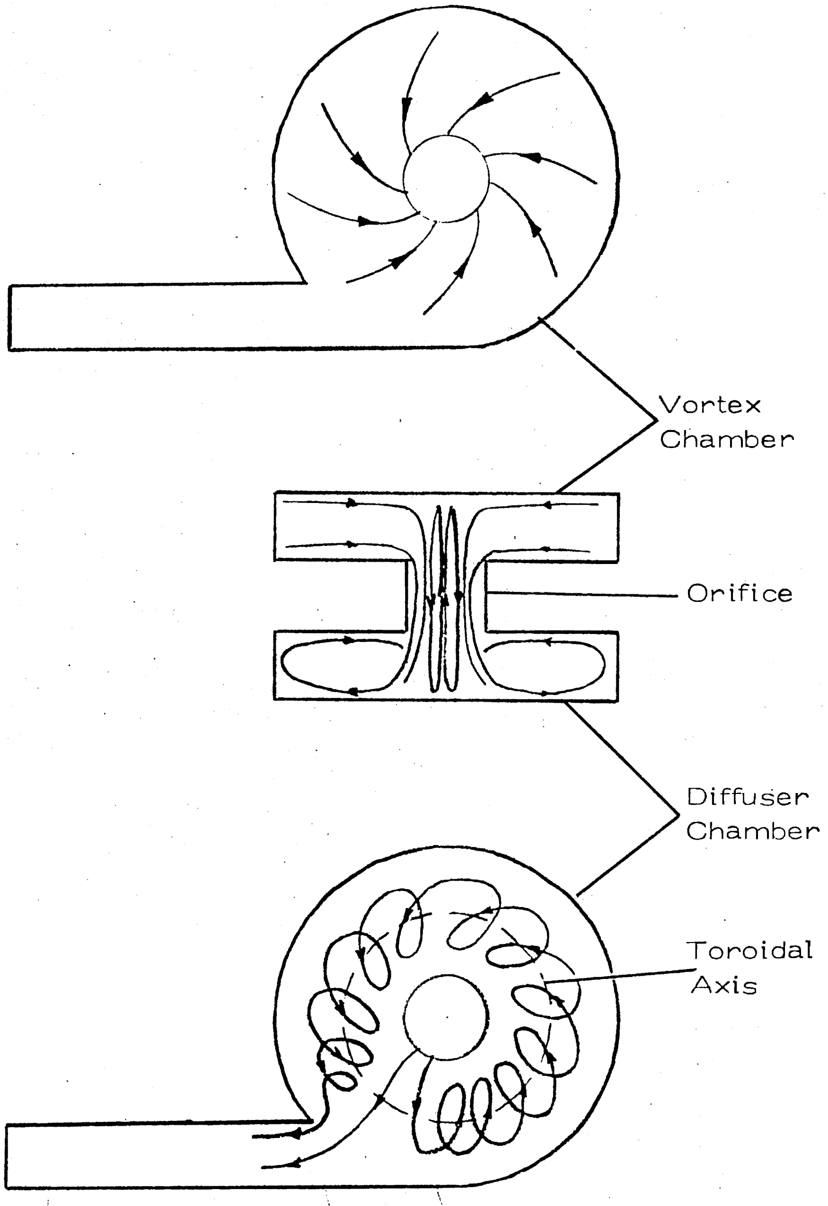

Figure 30. Flow Patterns in Vortex Resistor

The results shown in Figures 20-23 indicate that a boundary layer-vortex core model would be an appropriate description of the flow field in the vortex chamber. Figure 22 illustrates that the flow in the diffuser chamber is not symmetric about a mid-plane. The conceptual model for the idffuser chamber ideally should account for the observed reverse flow. Boundary layer flows may be assumed on the top and bottom surfaces of the diffuser chamber with the radial component of velocity being radially inward at the top and radially outward at the bottom.

IV.2. One-Dimensional Model of the NSVR

IV.2.1. Model Description

The geometry of the NSVR may be divided into four regions following the approach of Bichara and Orner [12]. Figure 31 shows the four regions. These regions may be modeled by making assumptions appropriate for the individual regions. The resulting equations may be suitably combined to result in an overall mathematical model.

The modeling approach for the NSVR is summarized below (see Appendix B for additional details). The inlet region of the NSVR is modeled as an orifice. The discharge coefficient characteristic is assumed to be the same as that of a short-tube orifice with a sharp-edged entry. Experimental data on the circular short-tube orifice reported in reference [18] are used even though the downstream conditions are not the same in the two cases. An empirical correlation (see Appendix B, Equation (B.5)) was developed to conveniently use the experimental orifice data.

The flow is assumed to be axisymmetric at the periphery of the region 2. The shear stress on the outer cylindrical surface of the

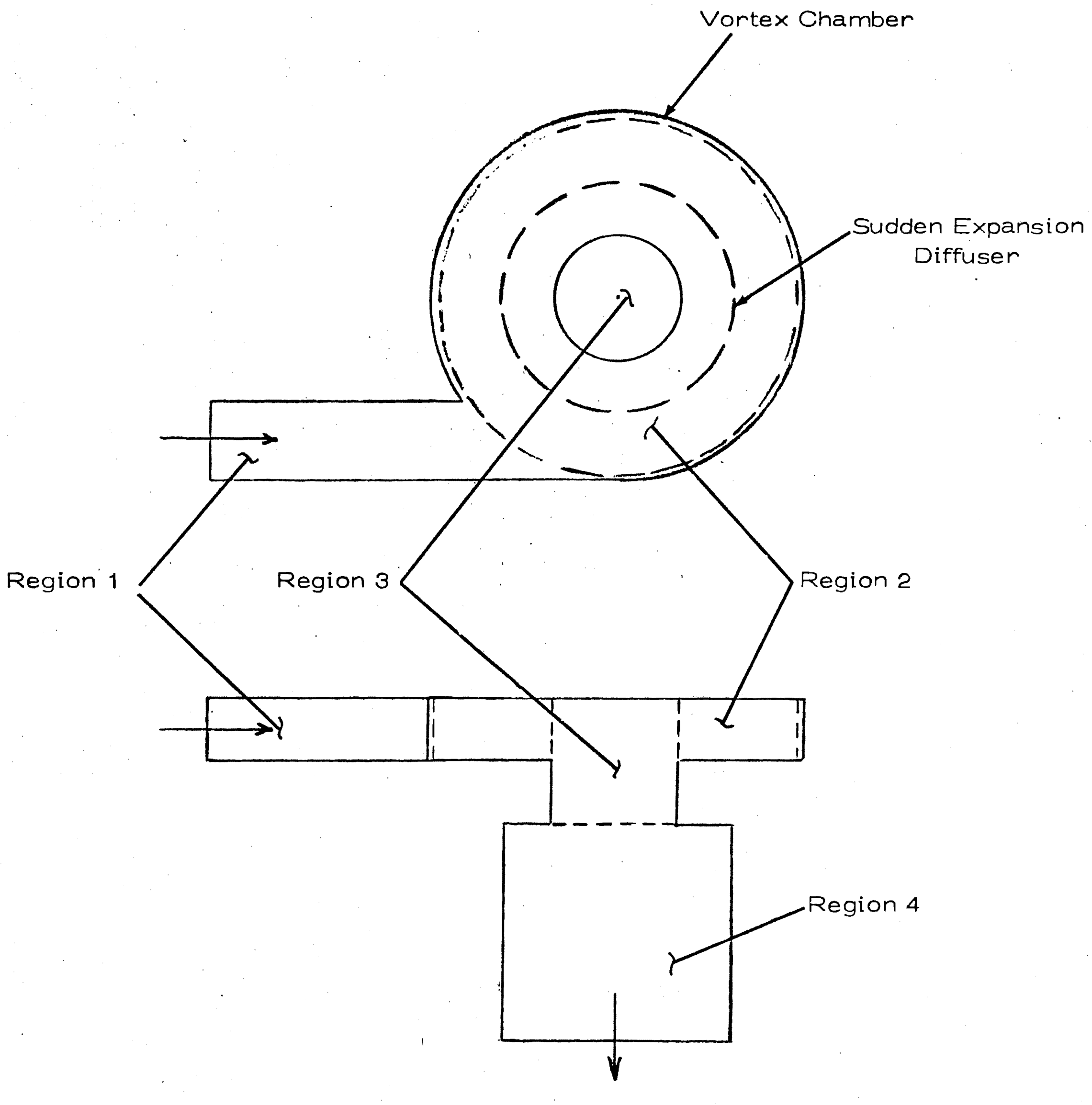

Figure. 31. Regions of NSVR

vortex chamber is obtained from an analogy with the flat plate solution of Blassius [32]. This assumption is understood to be a rough approximation. A more exact approach would take into account the non-axisymmetric nature of the flow field at the entry of the vortex chamber.

Flow within region 2 of the NSVR is assumed to be one-dimensional, i.e., the static pressures and velocities are assumed to be functions of the radial variable "r" only. The ordinary differential equations which result (see Appendix B) are much simpler than the corresponding ordinary differential equations that result from a momentum integral approach. These equations can be solved in closed form, which eliminates numerical integration and results in high computational efficiency. The assumption of uniform velocity profile does not permit inclusion of the shear stress into the model. However, a shear stress term can be artificially included. Radial shear is neglected but shear stress in the tangential direction is included.

The presence of a developing flow region in the vortex chamber suggests that the average shear stress should be greater than the shear stress for the fully-developed flow case. The tangential shear stress value was treated as a "free parameter," and was chosen such that the computed results agreed reasonably well with experimental data. A value two times that associated with fully-developed laminar flow between two parallel plates was found to produce acceptable results.

Region 3 is modeled as an orifice. Separation at the entry is minimized by the swirl, and the wall boundary layer is thinned due to centrifugal force produced by the swirl. These effects tend to result in a larger orifice discharge coefficient than for the case with no swirl. (For the case with no swirl, the discharge coefficient varies from 0.6 to 0.8 for the range of operation considered.) A value of unity was used for the discharge coefficient of the central orifice. The static pressure at the downstream end of the central orifice is assumed to be constant over the area of the orifice. But, the upstream pressure is allowed to vary with the radial distance r.

Region 4 is modeled as a sudden-expansion diffuser which recovers half of the kinetic energy of the fluid. This choice was based on an approximate analysis of the diffuser taking into account the effect of swirl. (See Appendix B for details.)

IV.2.2. Typical Results

Figures 32-35 compare experimental data and analytical predictions based on the one-dimensional model. The model predicts the experimentally observed behavior of the NSVR reasonable well in both the positive and negative temperature sensitivity regions for a majority of the geometries tested. The temperature range for the analytical predictions was limited to 95° to 135° F because of test stand limitations.

Figures 36-37 show analytical predictions for the temperature range -50°F to +150°F (a common military specification). The geometry of Figure 36 exhibits a relatively large negative temperature sensitivity (-0.0052 in^3/sec.-°F). In contrast, Figure 37 shows nearly zero temperature sensitivity (-0.0002 in^3/sec.-°F) over the entire temperature range. Experimental verification is needed to evaluate the accuracy of the predictions over the wide temperature range used in Figures 36 and 37.

Figure 38 shows the variation of flow rate as a function of

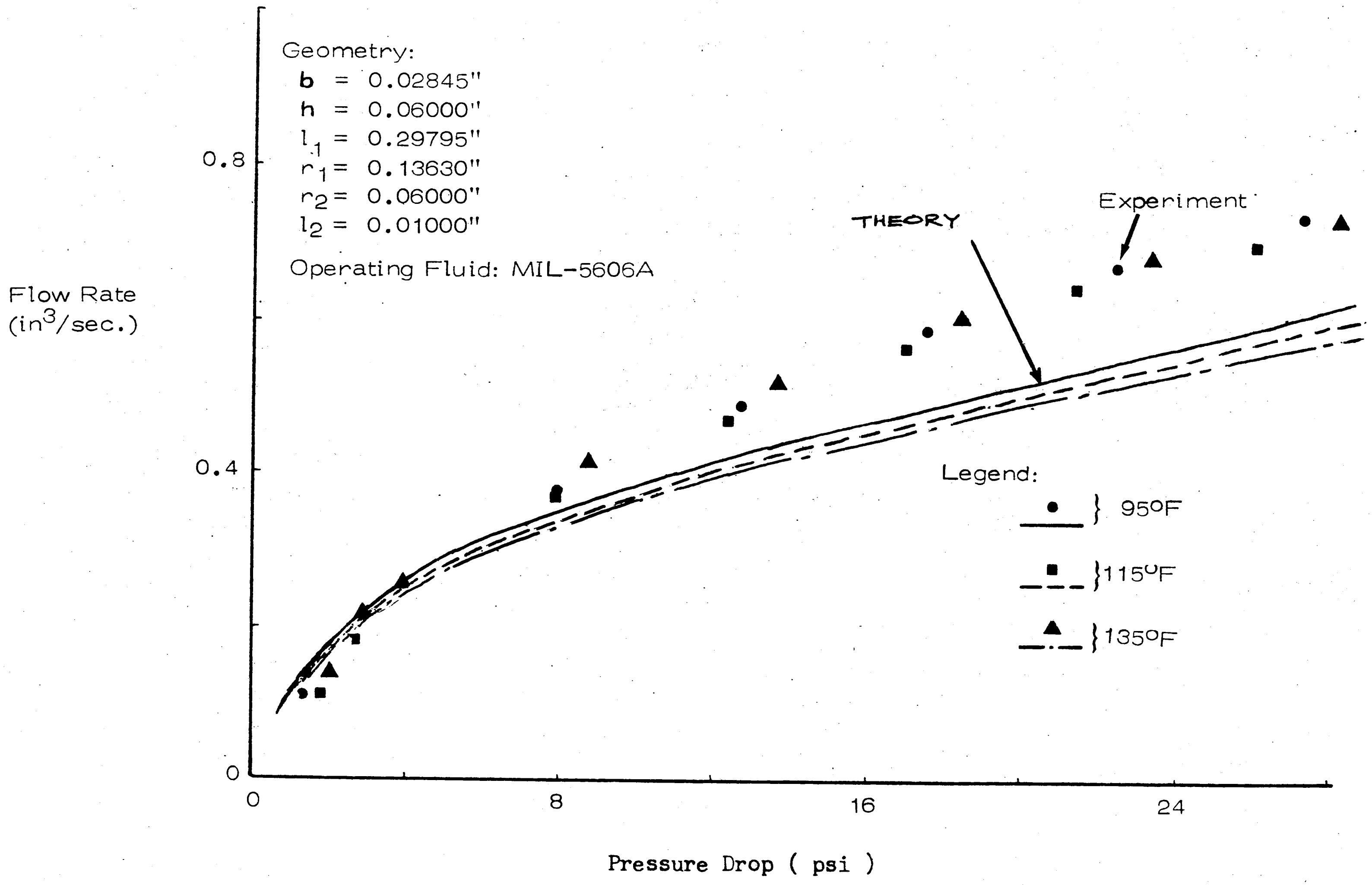

Figure 32. Comparison of Predictions of One-Dimensional Model With Experiment

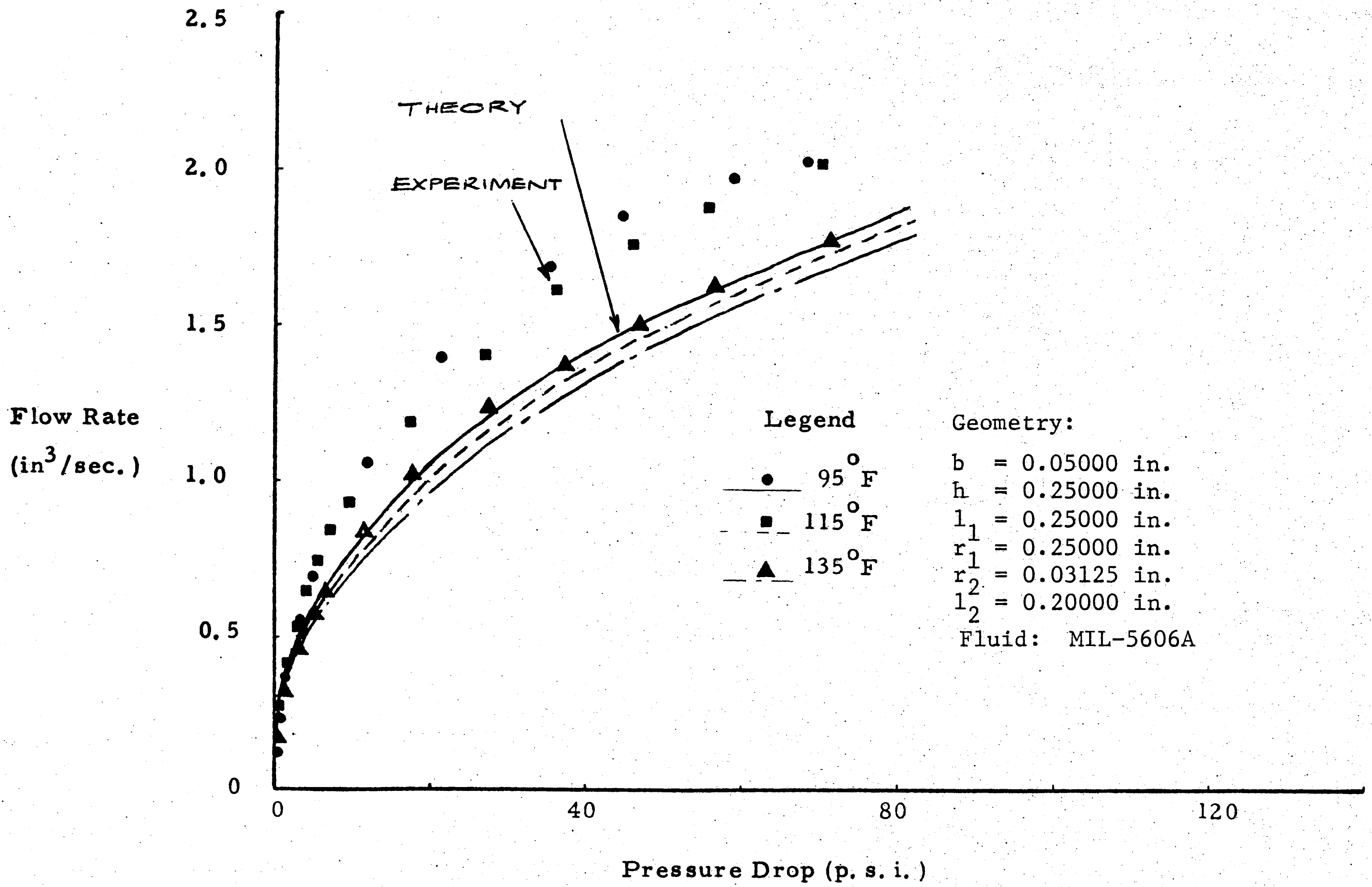

Figure 33. Comparison of One-Dimensional Model With Experiment

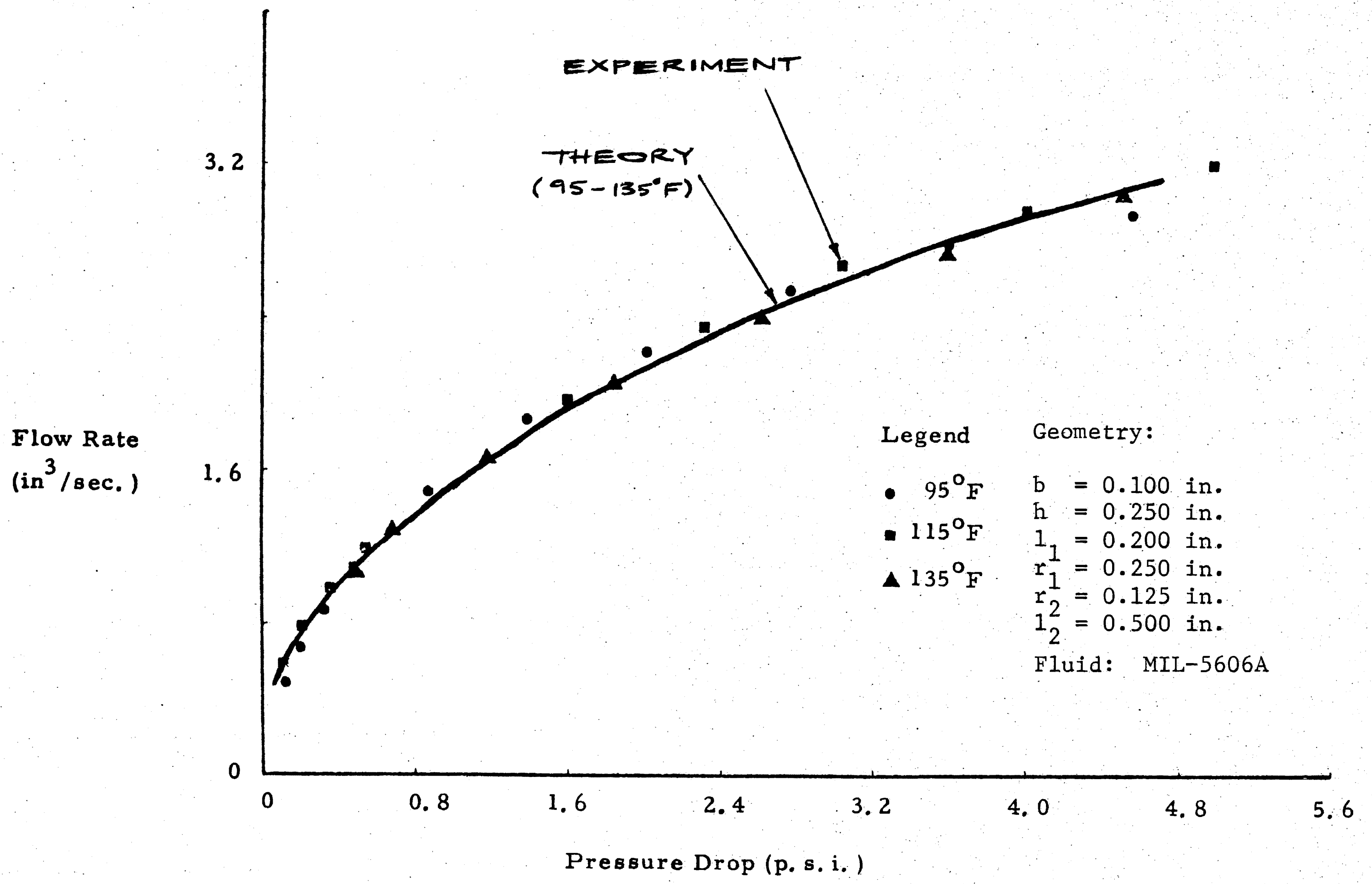

Figure 34. Comparison of One-Dimensional Model With Experiment

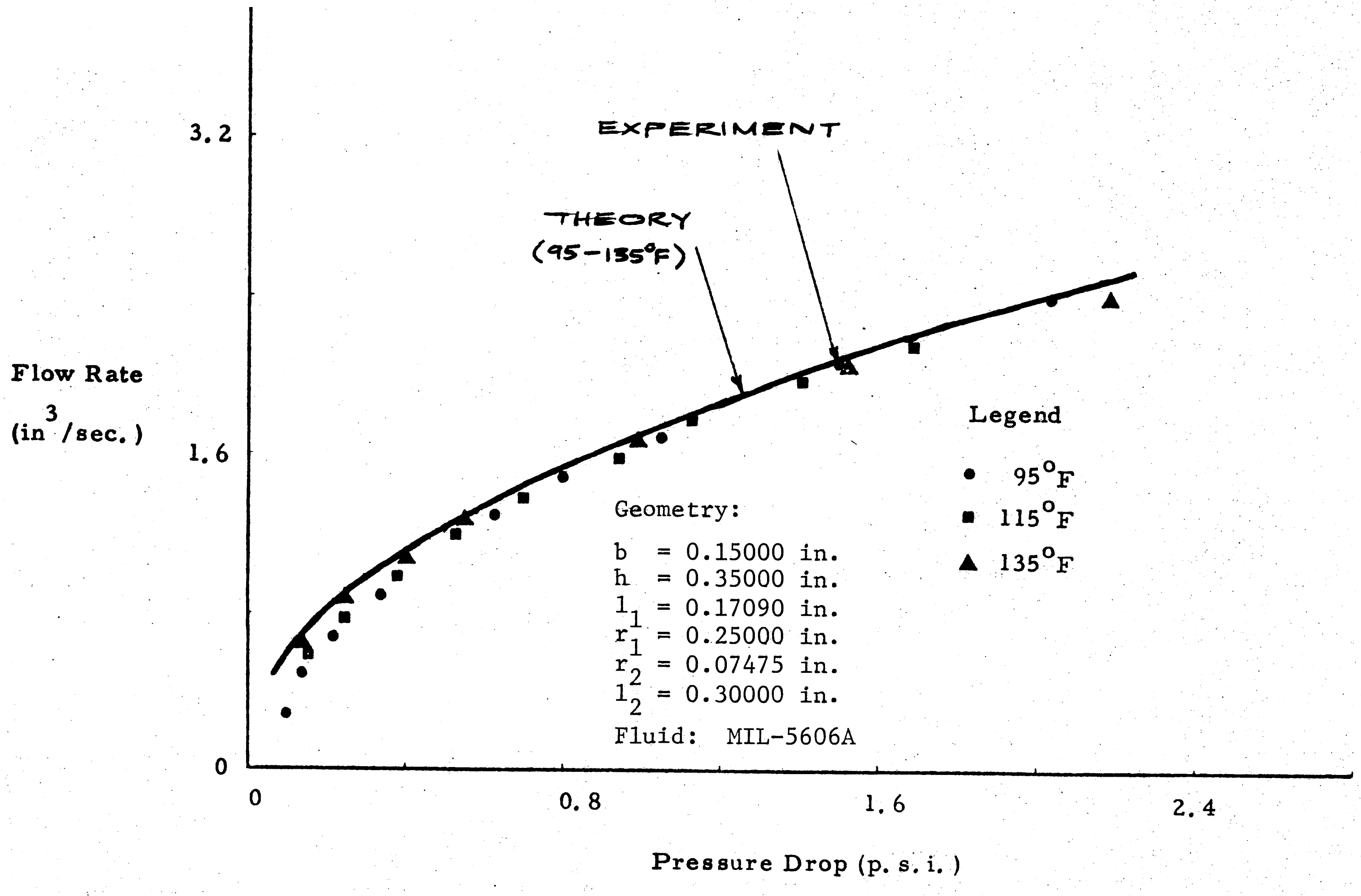

Figure 35. Comparison of One-Dimensional Model With Experiment

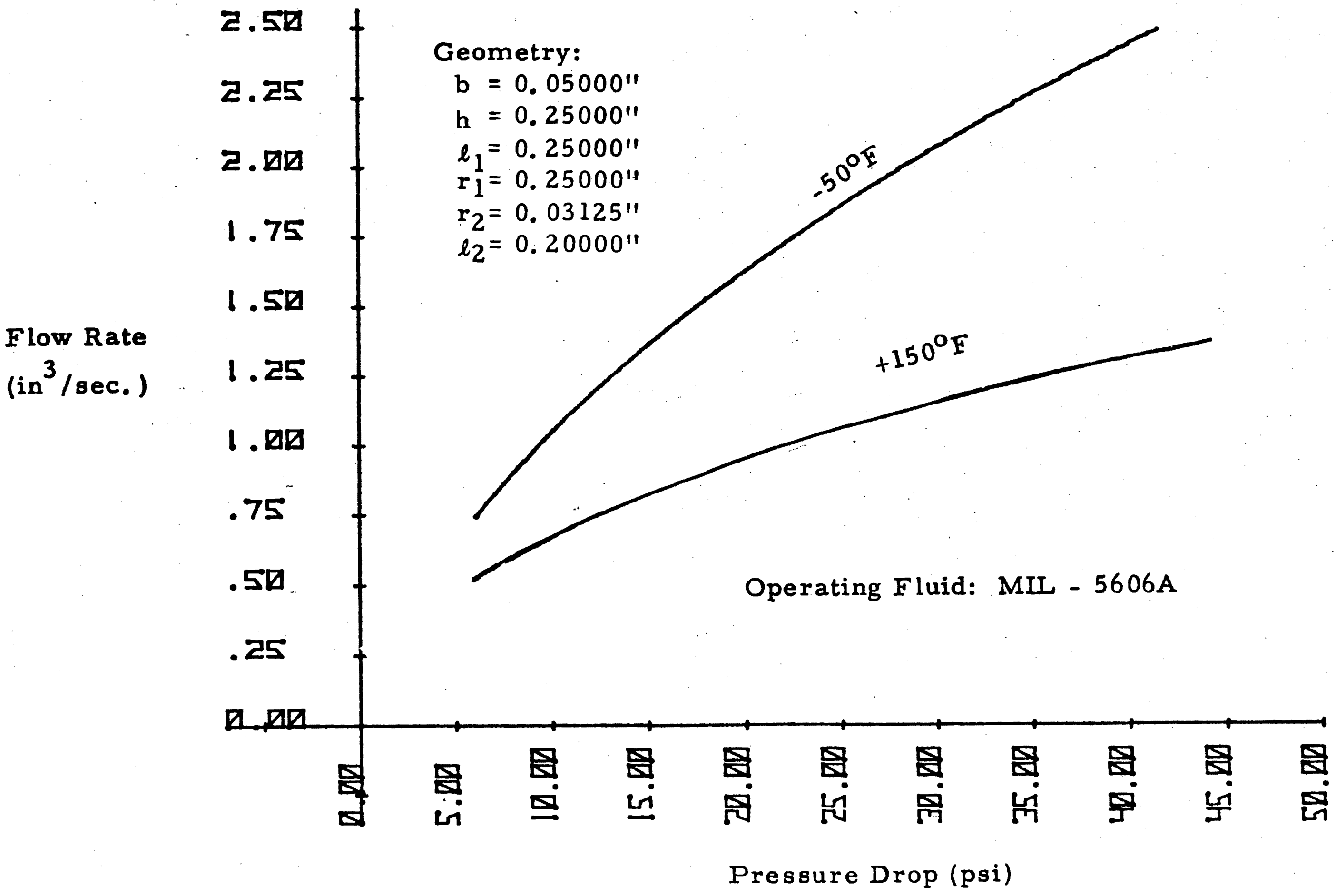

Figure 36. Steady-State Characteristic (Analytical) of a NSVR With a Large Negative Temperature Sensitivity

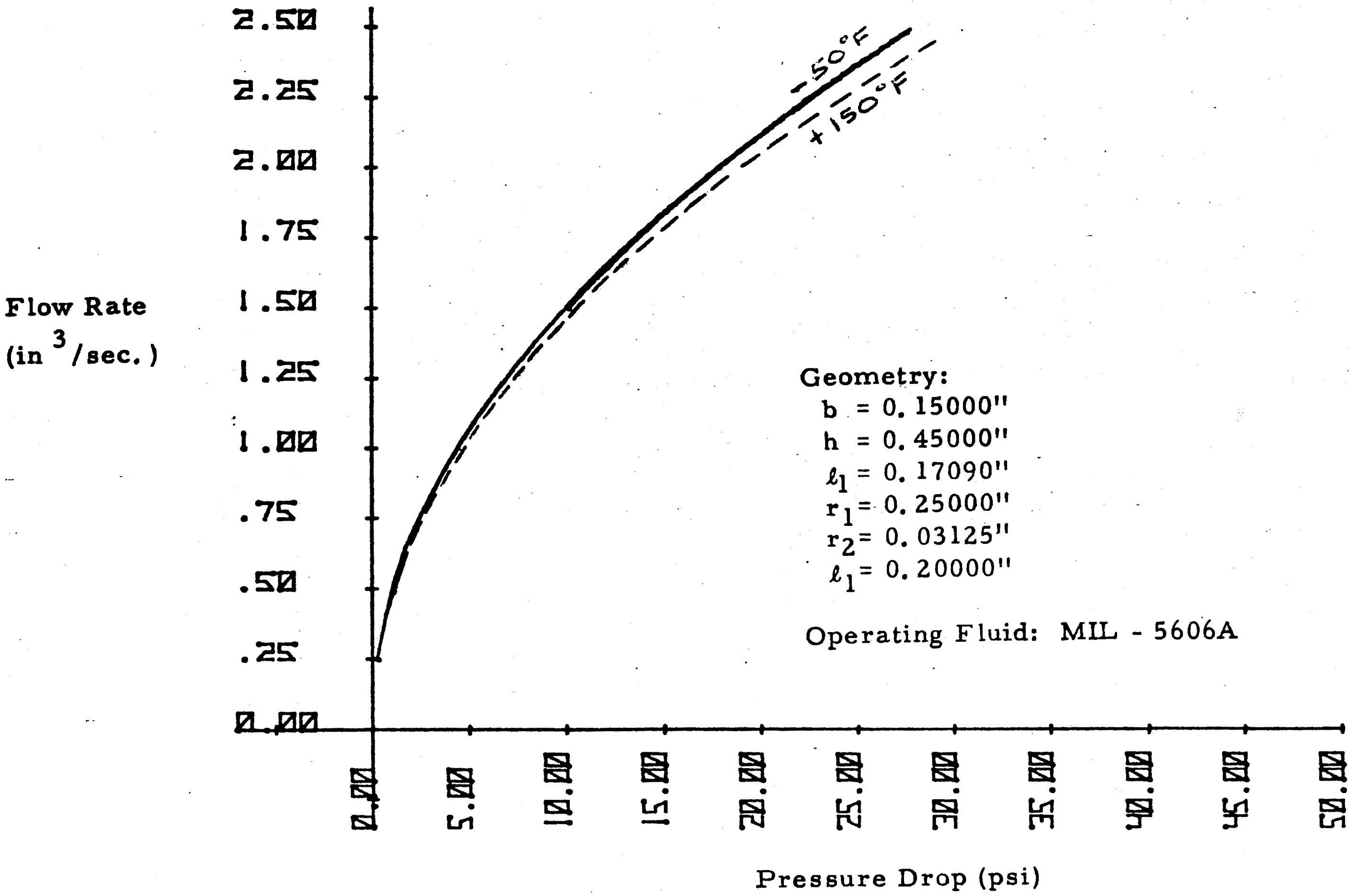

Figure 37. Steady-State Characteristic (Analytical) of a Temperature-Insensitive NSVR

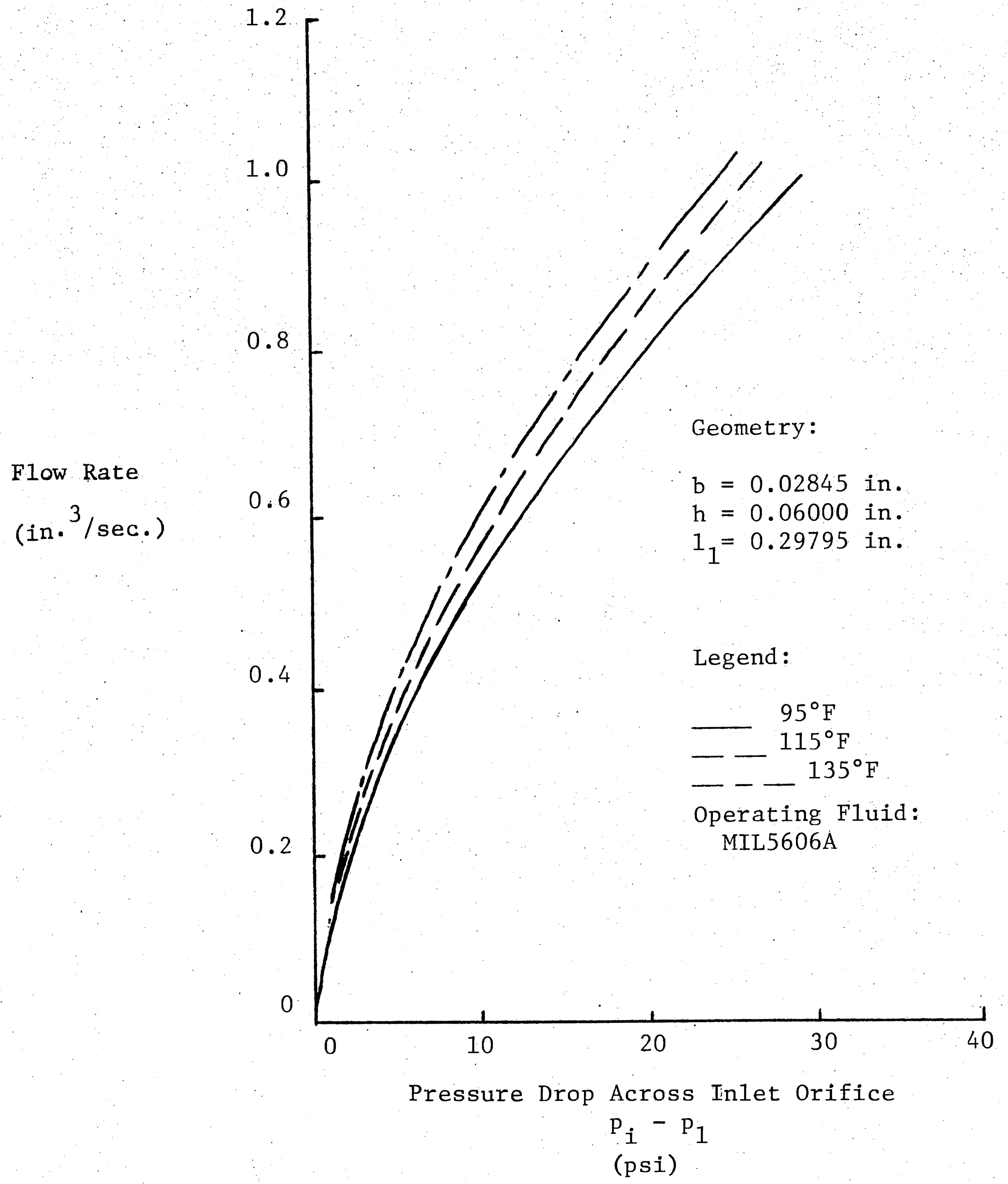

Figure 38. Computed Pressure Drop Across the Inlet Orifice

pressure drop across the inlet orifice and fluid temperature. The inlet orifice alone always exhibits a positive temperature sensitivity $[\partial Q/\partial T]$*. Figures 39 and 40 show the variation of the flow rate for the vortex chamber and the central orifice respectively. The average tangential velocity in a vortex is approximately proportional to the square root of the pressure drop across the vortex. The average tangential velocity in a given vortex chamber increases with higher flow rates and lower velocities. Therefore, if the viscosity decreases (due to temperature rise) the flow rate must decrease to maintain a constant average tangential velocity (or equivalently, the pressure drop). Thus, $\partial Q/\partial T|_{\Delta P=\text{constant}}$ is negative for the vortex chamber.

In the case of the central orifice the effect of inlet swirl is to force the fluid towards the cylindrical wall, thereby reducing the effective cross-sectional area of the orifice. As the fluid temperature increases (accompanied by viscosity decrease and swirl increase) the effective orifice area decreases and the resistance increases; the result is a negative $\partial Q/\partial T|_{\Delta P=\text{constant}}$.

At low pressure drops the swirl effect is small in both the vortex chamber and the central orifice. In this case, the inlet orifice characteristic dominates the NSVR resistance characteristic, resulting in an overall positive temperature sensitivity. At higher pressure drops the vortex chamber and the central orifice characteristics dominate, resulting in a negative temperature sensitivity for the NSVR. If the inlet orifice can be operated in the pressure drop range where $\partial C_d/\partial R_e$

---

*Temperature sensitivity is defined for a constant pressure drop.

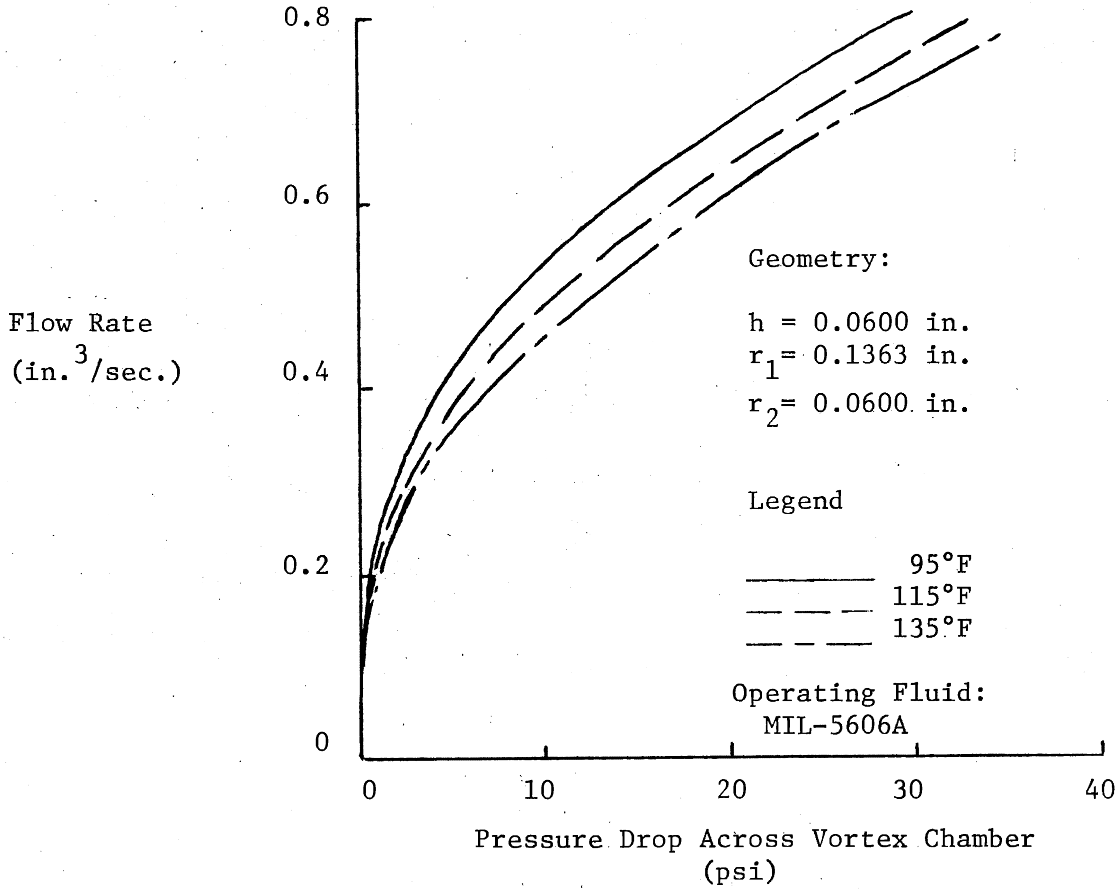

Figure 39. Computed Pressure Drop Across Vortex Chamber

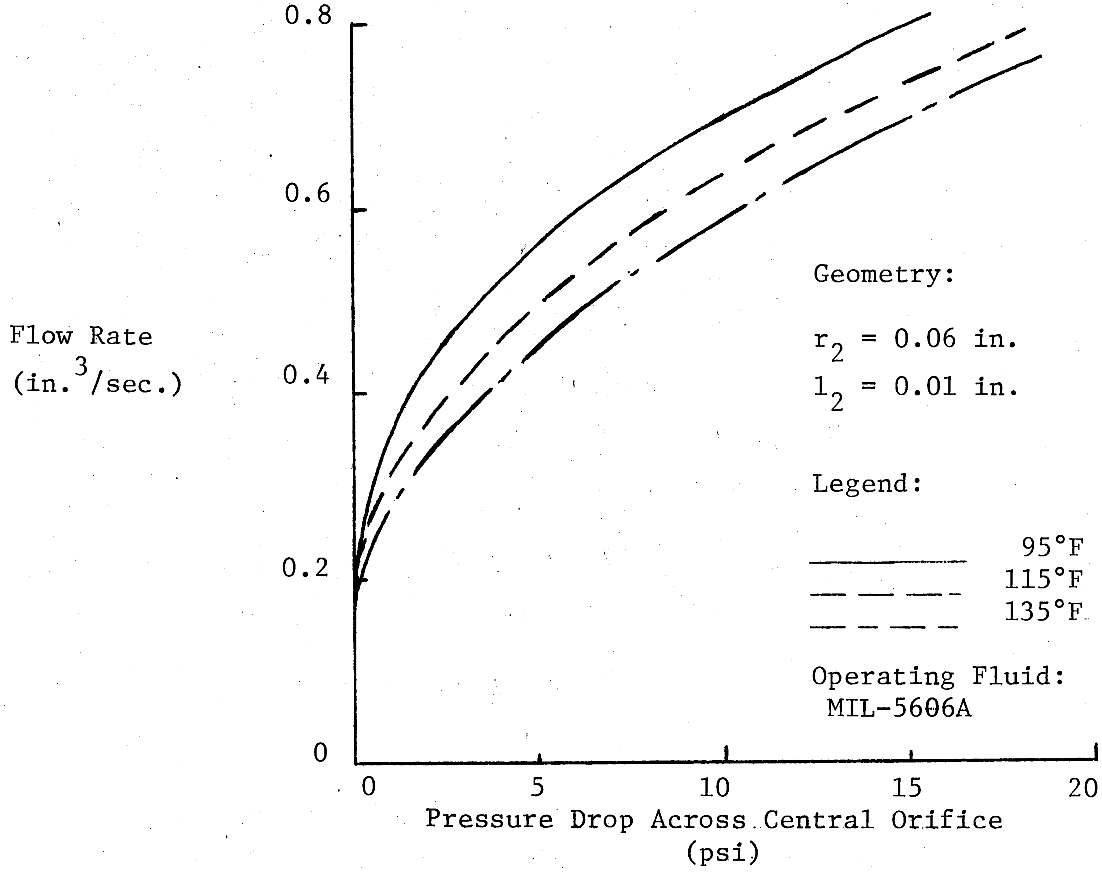

Figure 40. Computed Pressure Drop Across the Central Orifice

is negative (possible only for L/D<1; see Figure 41), the inlet orifice characteristic will reinforce the vortex chamber and central orifice characteristics, with the result that the overall temperature sensitivity is more negative than with the vortex chamber and the central orifice alone.

IV.3. One-Dimensional Model of the SVR

IV.3.1. Model Description

The SVR geometry is conveniently divided into five regions as shown in Figure 42 (see Appendix C for mathematical details). Models for regions 1, 2, and 3 are the same as those developed for the NSVR. A one-dimensional, axisymmetric flow is assumed to exist in region 4, which is contradictory to the flow field observed in the flow visualization study described earlier (see Section IV.1). In region 4 the flow field is essentially non-symmetric about a mid plane through the diffuser chamber. But, a non-uniform velocity profile would lead to partial differential equations, thereby increasing substantially the mathematical complexity of the model. The simpler one-dimensional axisymmetric assumption yields a model which is of lesser accuracy but greater mathematical simplicity than the partial differential equation model.

Regions 1 and 5 of the SVR are modeled as orifices with discharge coefficients equal to that of a short-tube orifice with a sharp-edged entry (see Figure 41).

IV.3.2. Typical Results

Figures 43-46 show comparisons of analytical predictions with typical experimental data for four SVR geometries. Geometries were

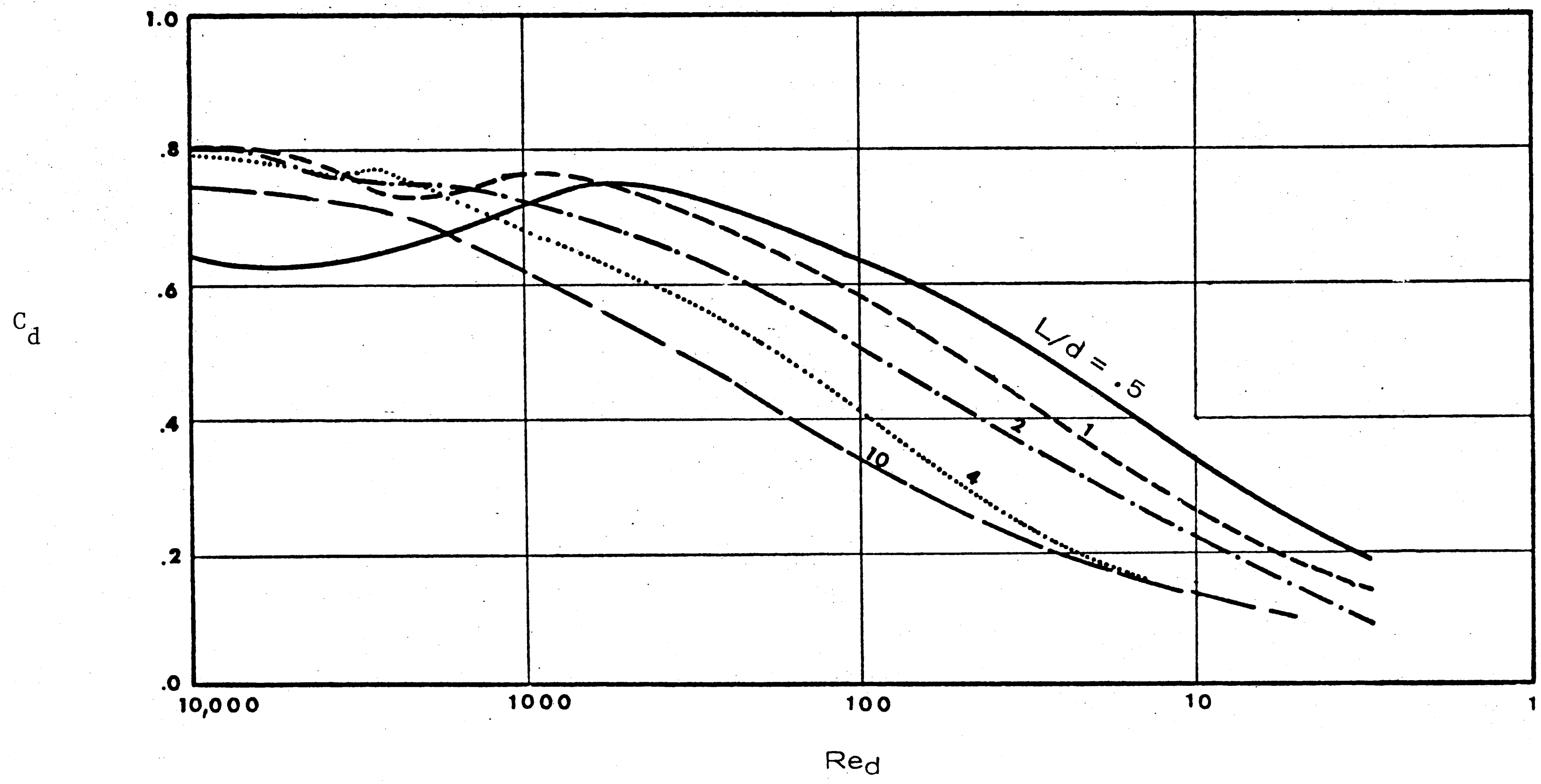

Figure 41. Discharge Coefficient of Circular Short-Tube Orifice With Sharp-Edged Entry (See Reference [18])

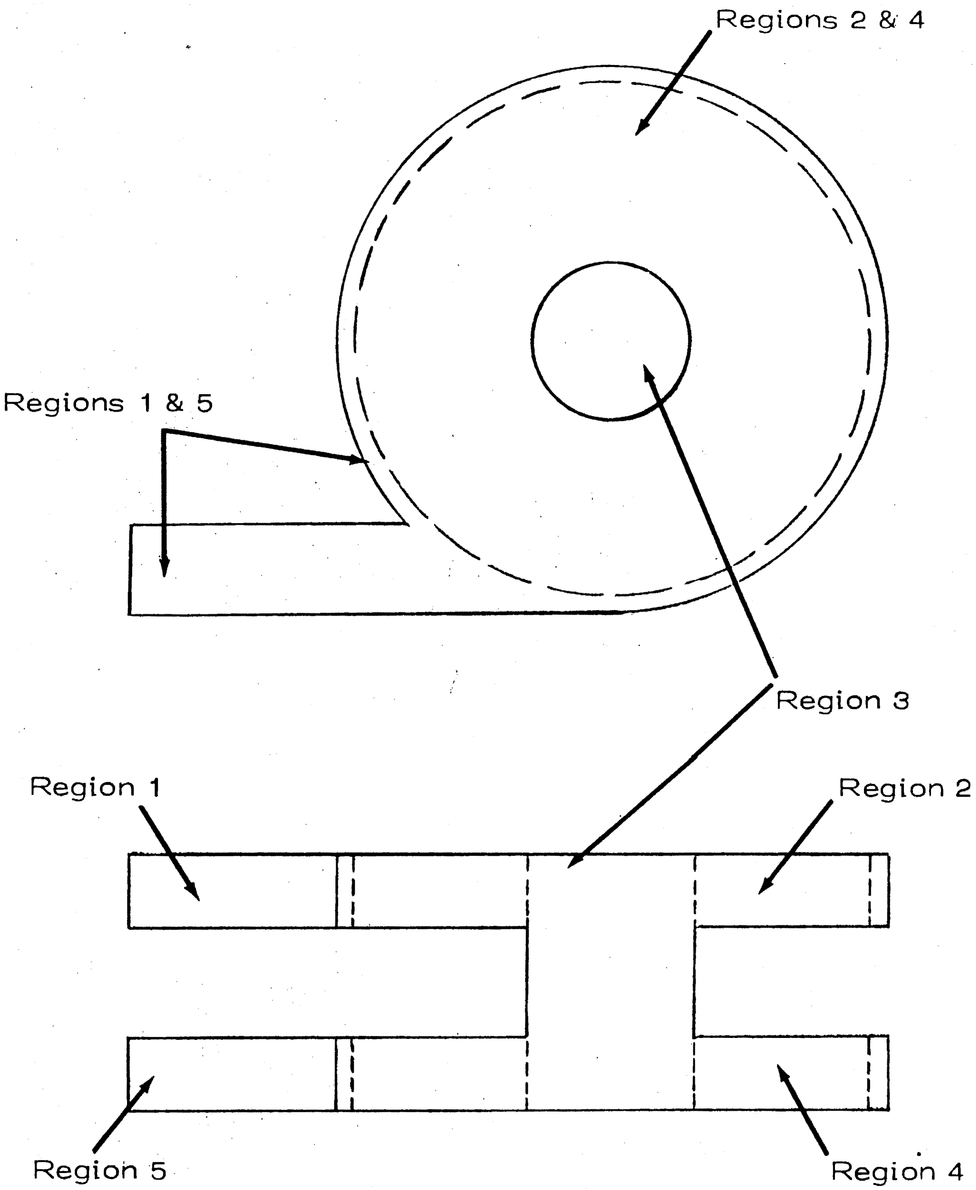

Figure 42. Regions of SVR

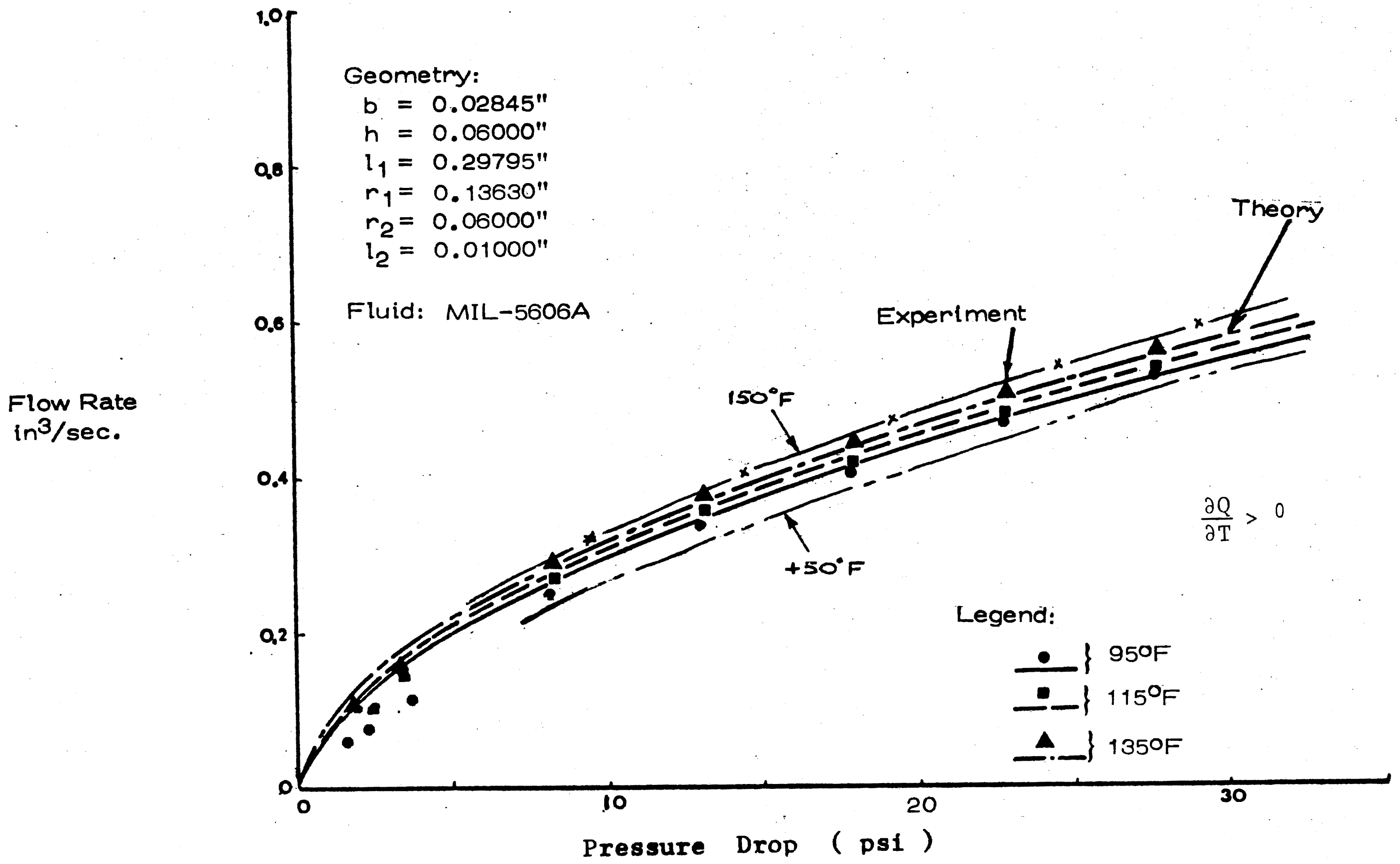

Figure 43. Comparison of Predictions of One-Dimensional Model With Experimental Data of SVR

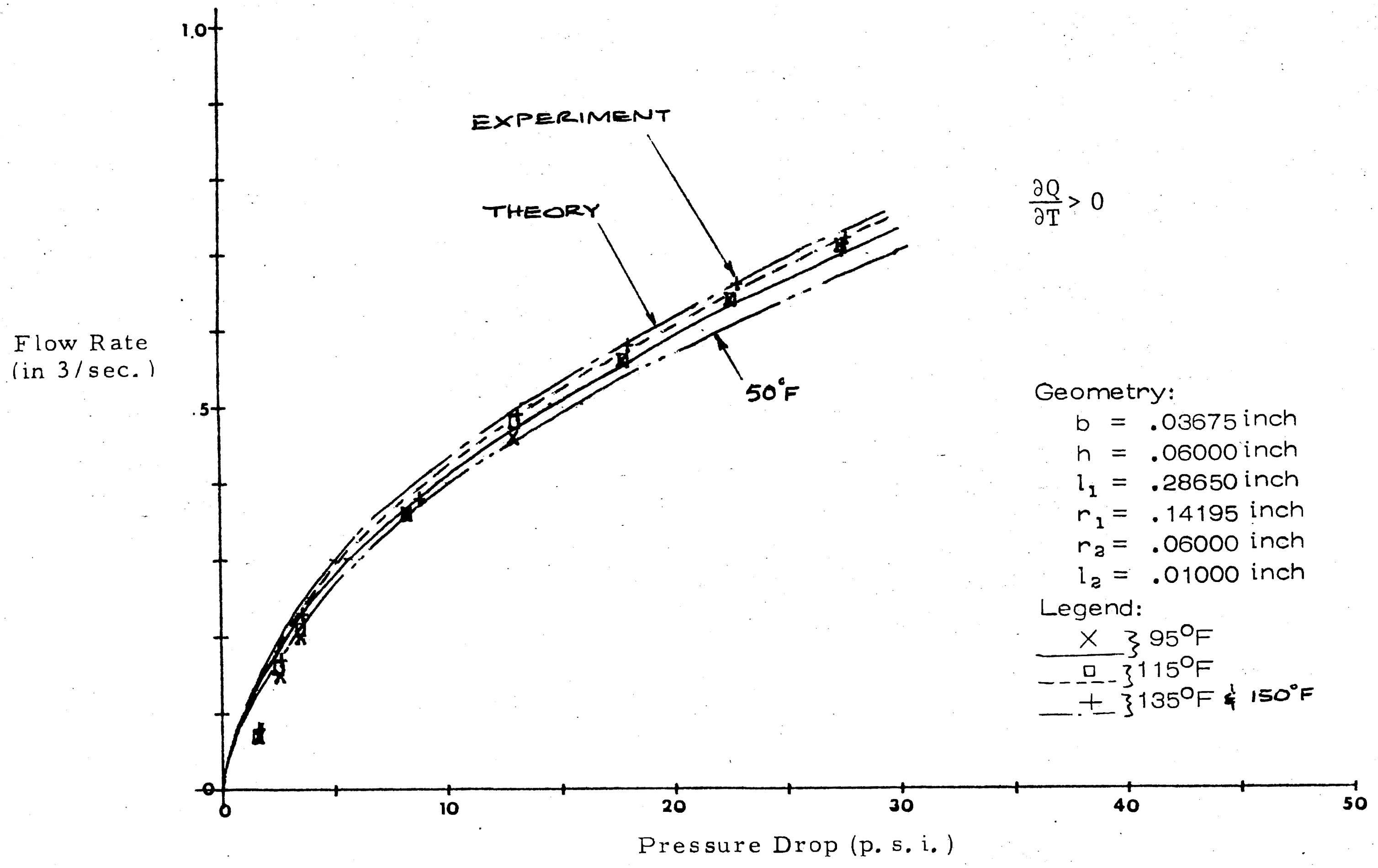

Figure 44. Comparison of Predictions of One-Dimensional Model With Experimental Data of SVR

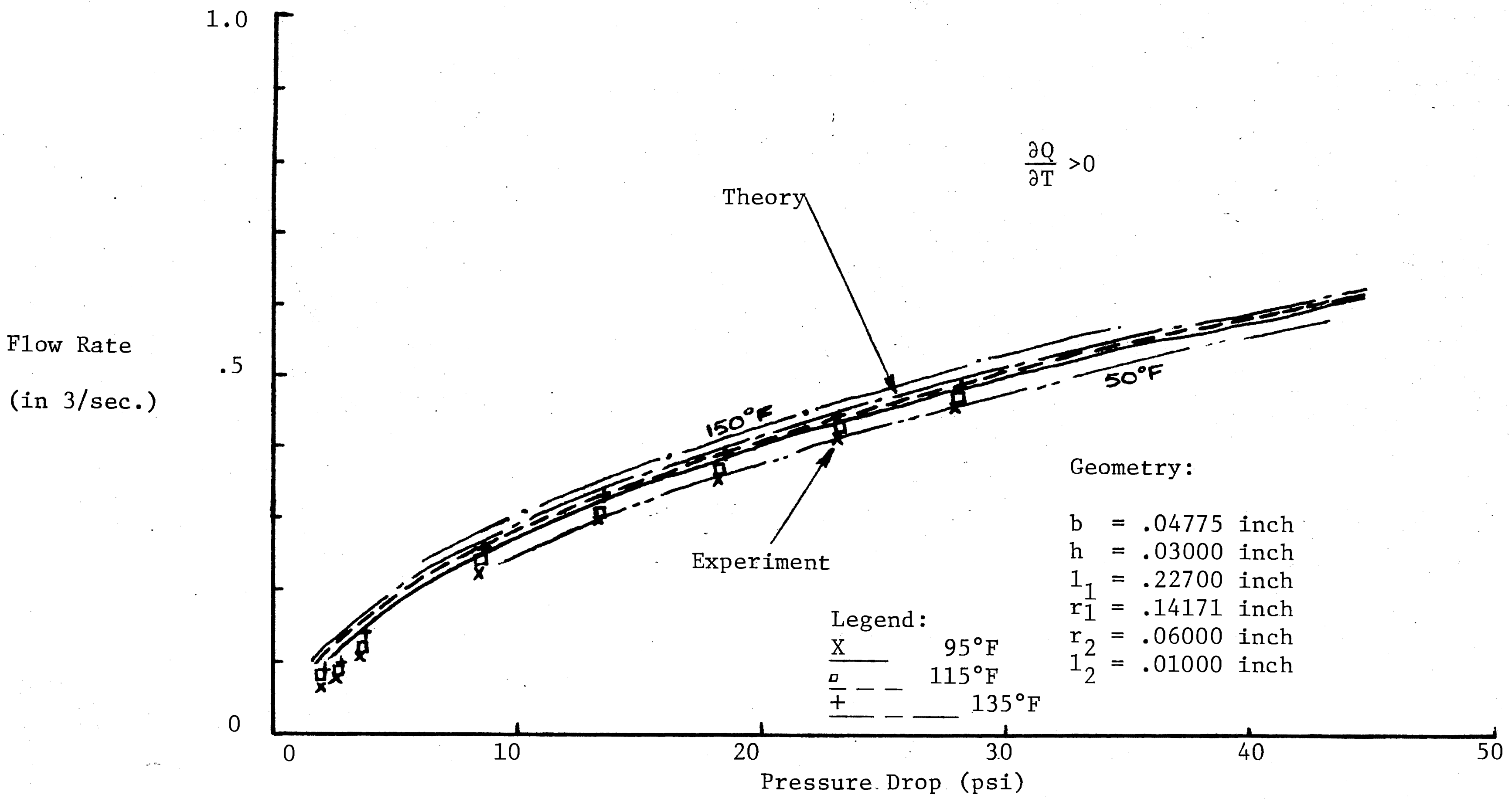

Figure 45. Comparison of Predictions of One-Dimensional Model With Experimental Data of SVR

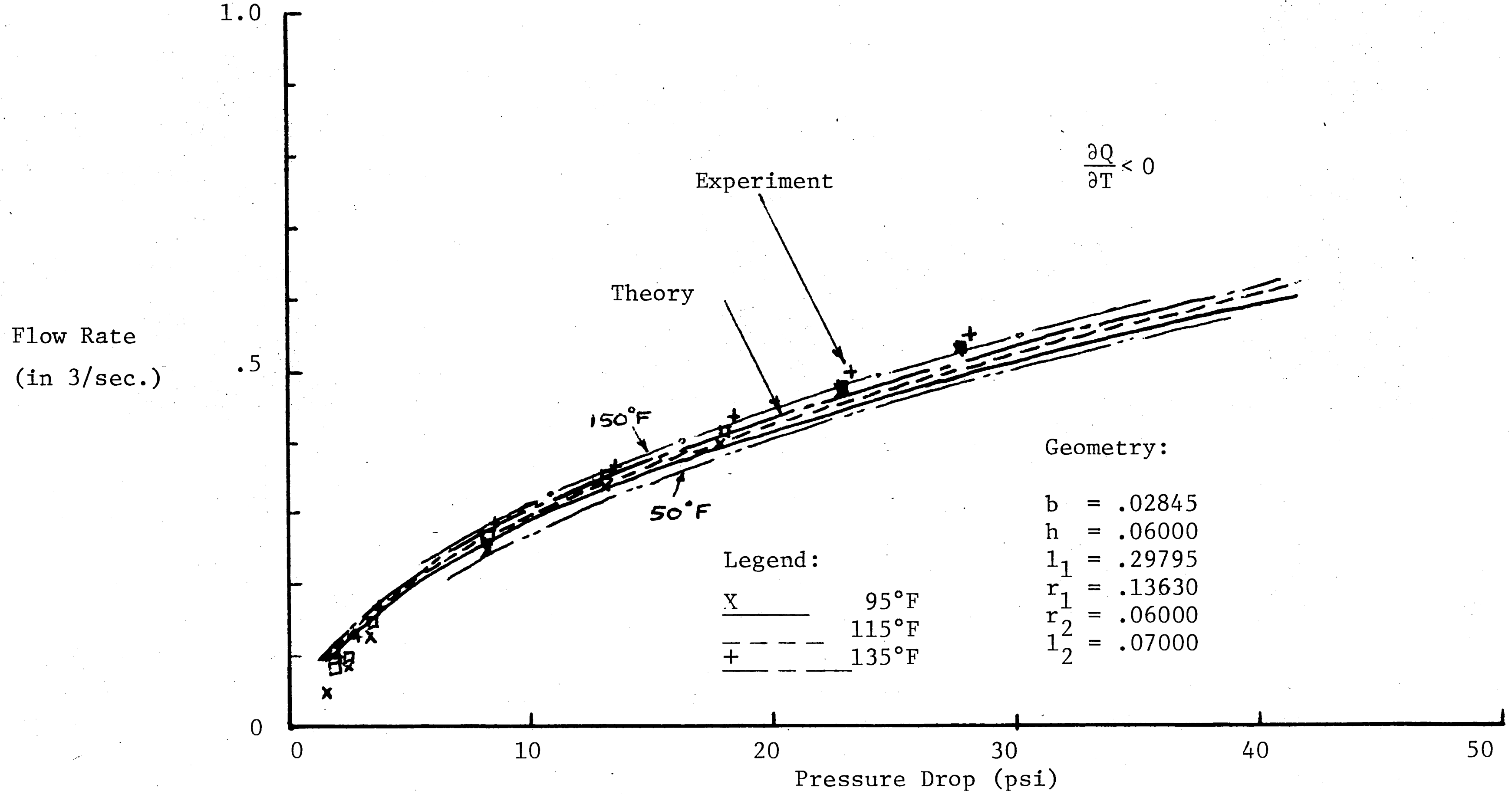

Figure 46. Comparison of Predictions of One-Dimensional Model With Experimental Data of SVR

available which resulted in small temperature sensitivities only, although larger temperature sensitivities are possible with other geometries. The difference between the experimental and predicted values of the flow rate (at constant pressure drop) is less than 5 percent of reading for all but the low flow rate range in all four cases considered. The characteristics at -50°F and +150°F shown in Figures 43-46 indicate the temperature sensitivity of the geometries over a wide temperature range.

IV.4. Two-Dimensional Model of the SVR

IV.4.1. Model Description

The steady-state relations used in the one-dimensional model of the NSVR for regions 1, 3, and 4 are also used for the two-dimensional model.

The model for region 2 is developed by adapting the momentum integral approach of Wormley [9] to the laminar flow case. Appropriate non-uniform velocity profile functions are assumed for the radial and tangential velocities, and the laminar shear stresses (both radial and tangential) are computed directly from the velocity profiles. Integration of the partial differential equations along the vortex chamber height leads to a system of four non-linear ordinary differential equations which are solved numerically. The model includes a "developing-flow" region (as was originally employed by Wormley [9]). In the developing flow region the radial velocity in the core is non-zero and the circulation (i.e., rv_δ) is constant. When the flow is "developed," the radial velocity in the core is zero and the circulation is not constant. Unlike the one-dimensional model, the shear stresses are computed directly from the velocity profiles.

The differential equations are locally linearized at $r=r_1$ (see Appendix D for details) to eliminate computational difficulties which result from the singularity at the outer periphery of the vortex chamber (i.e., at $r=r_1$). An approximate solution, valid in a close neighborhood of r_1, is obtained to initiate the numerical integration.

IV.4.2. Typical Results

Figures 47-50 show comparisons of model predictions and typical experimental data for different NSVR geometries. The difference between experimental and predicted values is less than 15 percent of reading in all cases.

The two-dimensional model predicts the temperature sensitivity more accurately (see Figures 33 and 48) than the one-dimensional model. The improvement in the accuracy may be attributed to the two-dimensional nature of the velocity profiles.

Figures 51 and 52 show the radial distribution of the velocities and the boundary layer thickness corresponding to the NSVR geometry of Figure 47 for a flow rate of 0.4 in^3/sec. The radial velocity in the core (i.e., u_δ) is zero at about $r=0.127$ inch (see Figure 51), indicating that all the flow is contained in the boundary layer. The boundary layer thickness (δ) increases rapidly in the developing flow region. The thickness (δ) increases slowly and then decreases as the flow progresses towards the center. The decrease is due to a rapid acceleration of the fluid particles in the radial direction caused by the steep pressure gradient existing near the center (see Figure 52). The tangential velocity (v_δ) increases linearly in the developing flow region and remains relatively constant in the developed flow region.

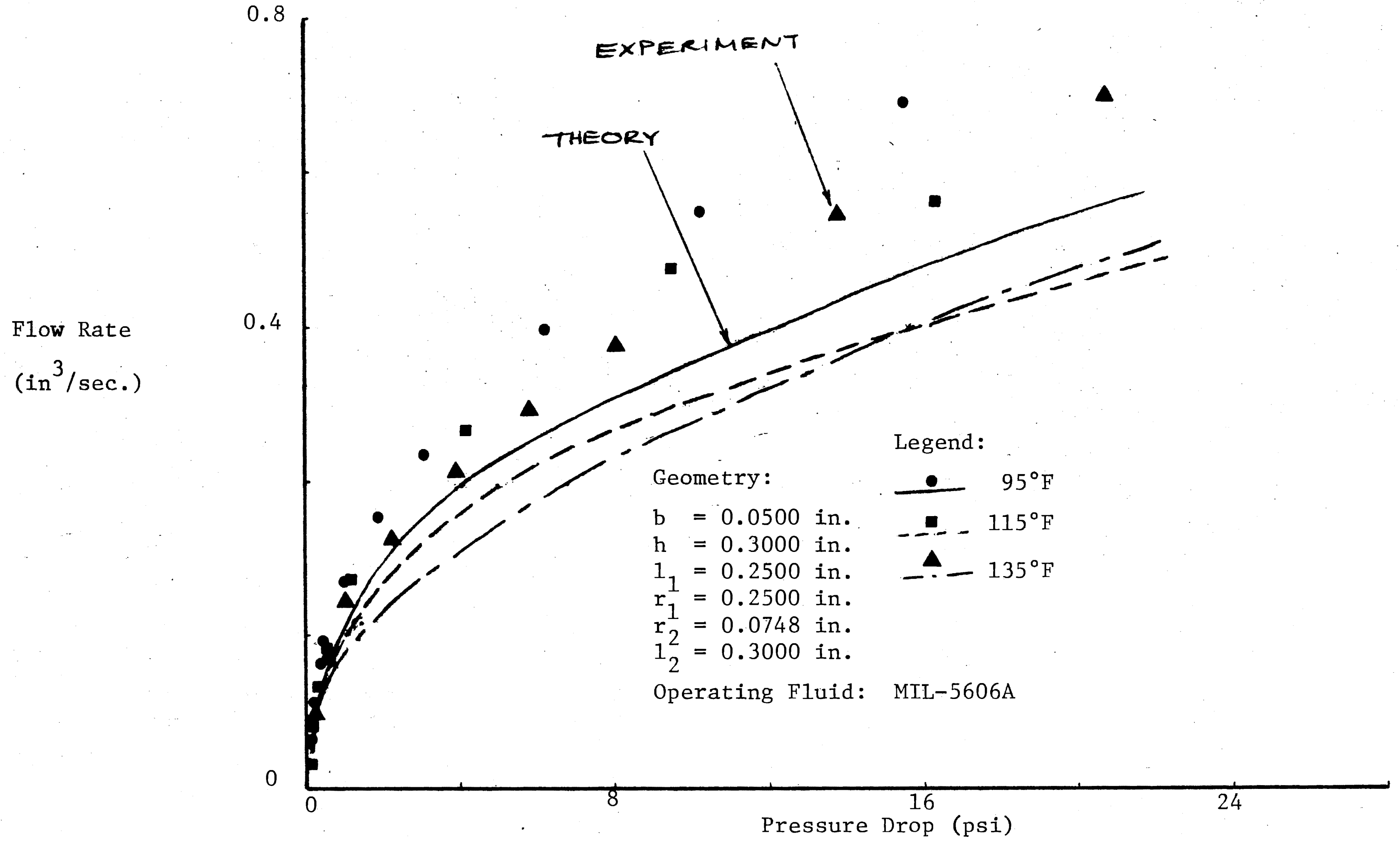

Figure 47. Comparison of Predictions of Two-Dimensional Model With Experiment

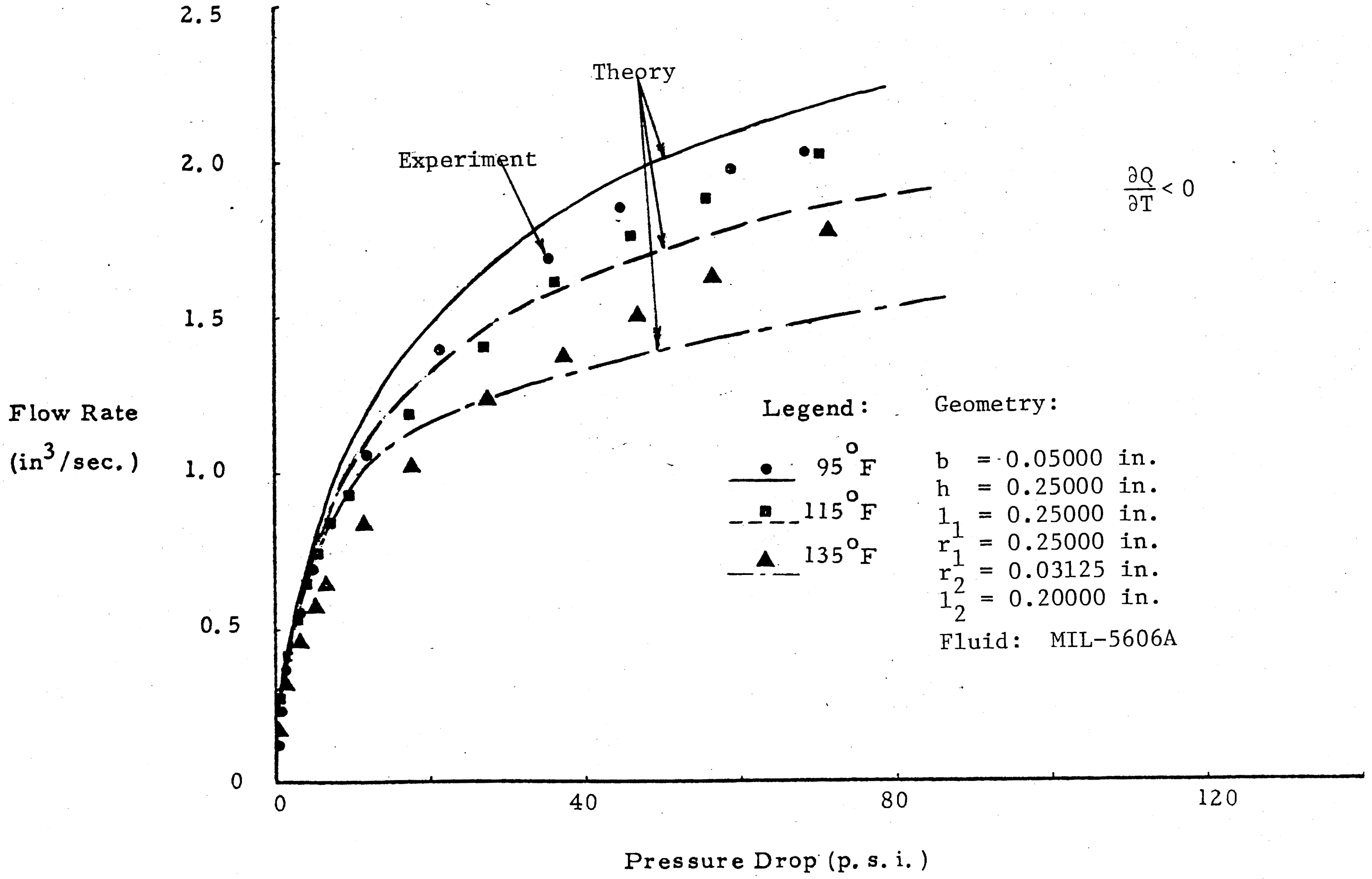

Figure 48. Comparison of Predictions of Two-Dimensional Model With Experiment

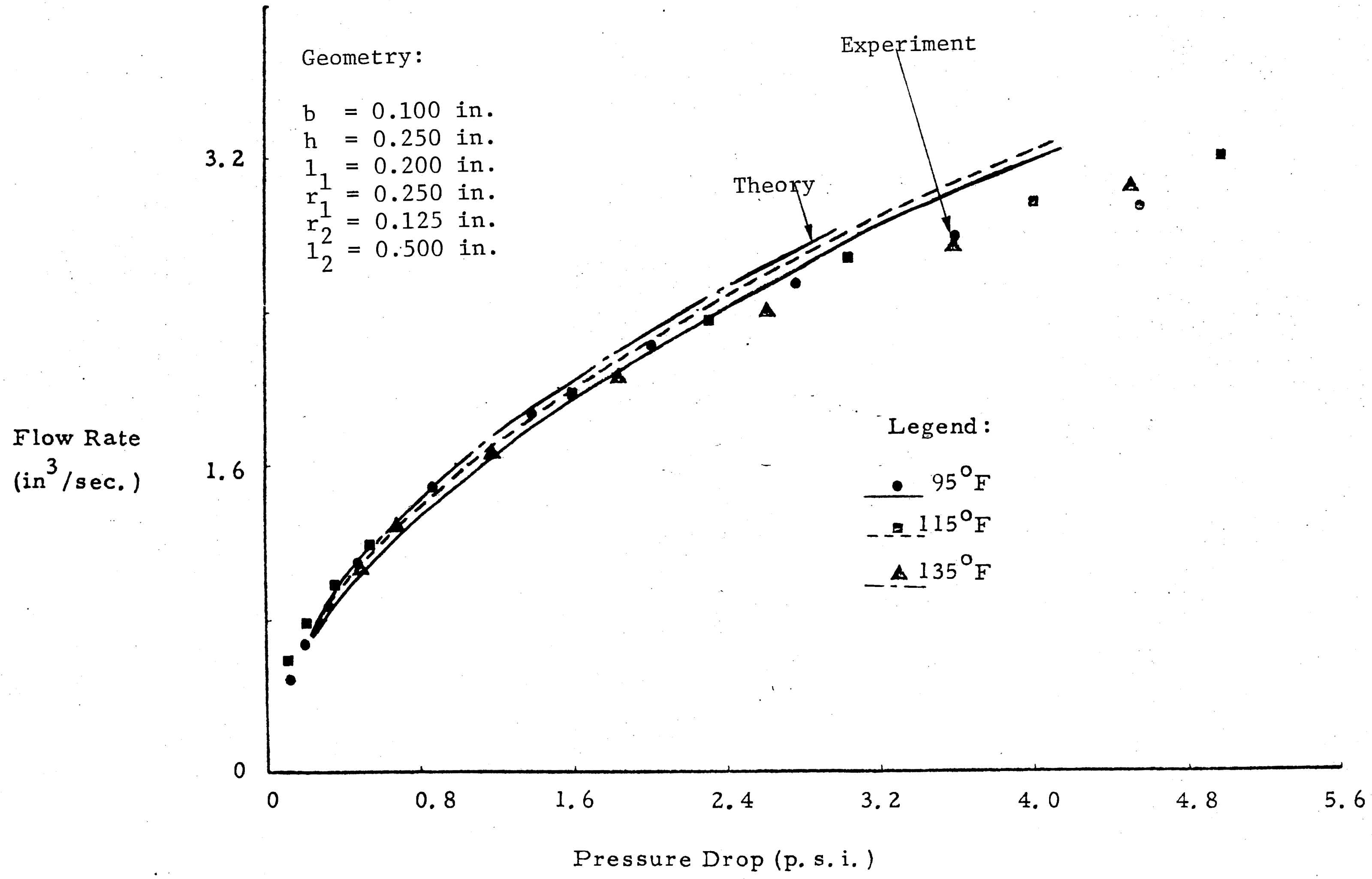

Figure 49. Comparison of Predictions of Two-Dimensional Model With Experiment

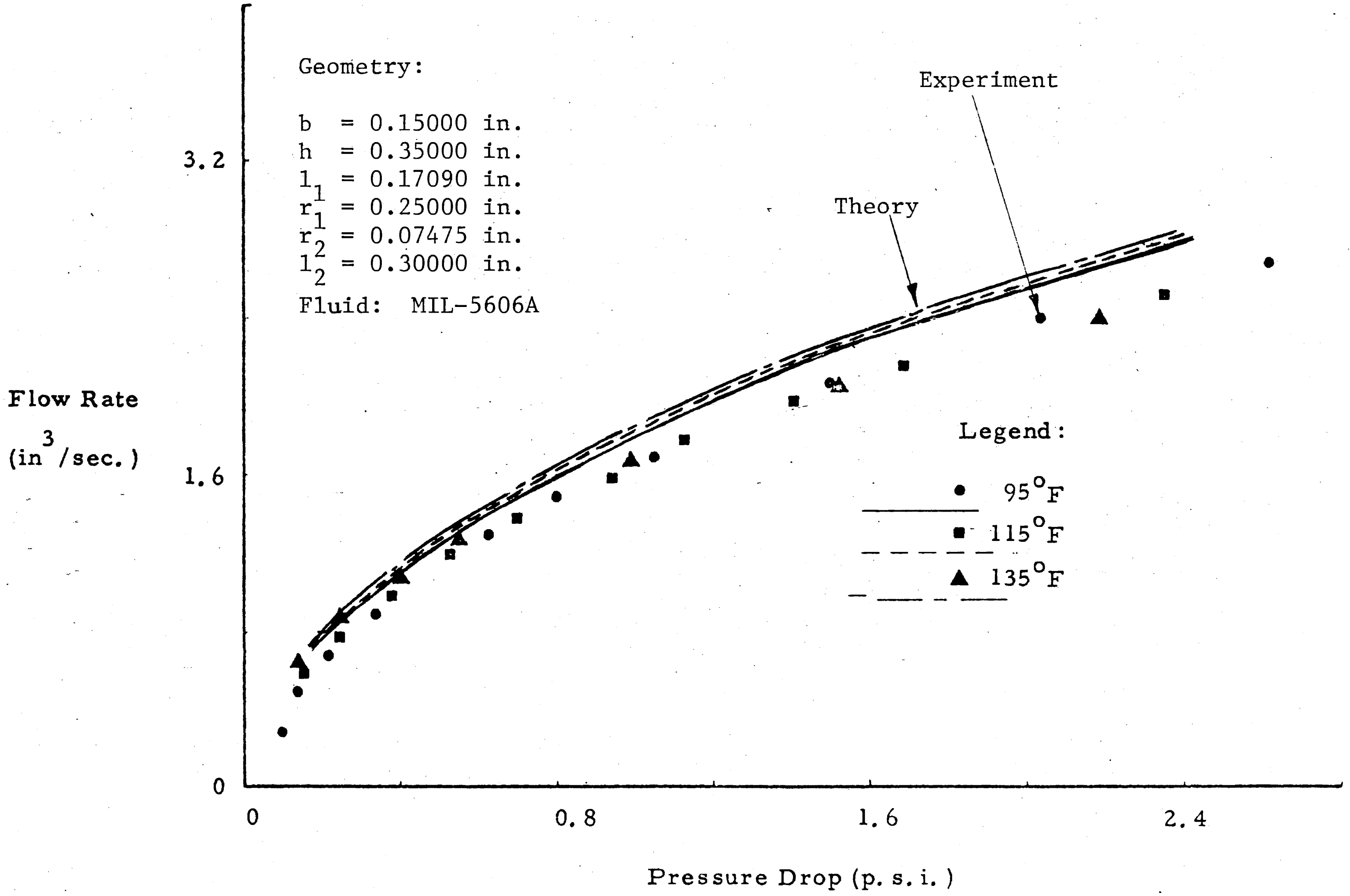

Figure 50. Comparison of Predictions of Two-Dimensional Model With Experiment

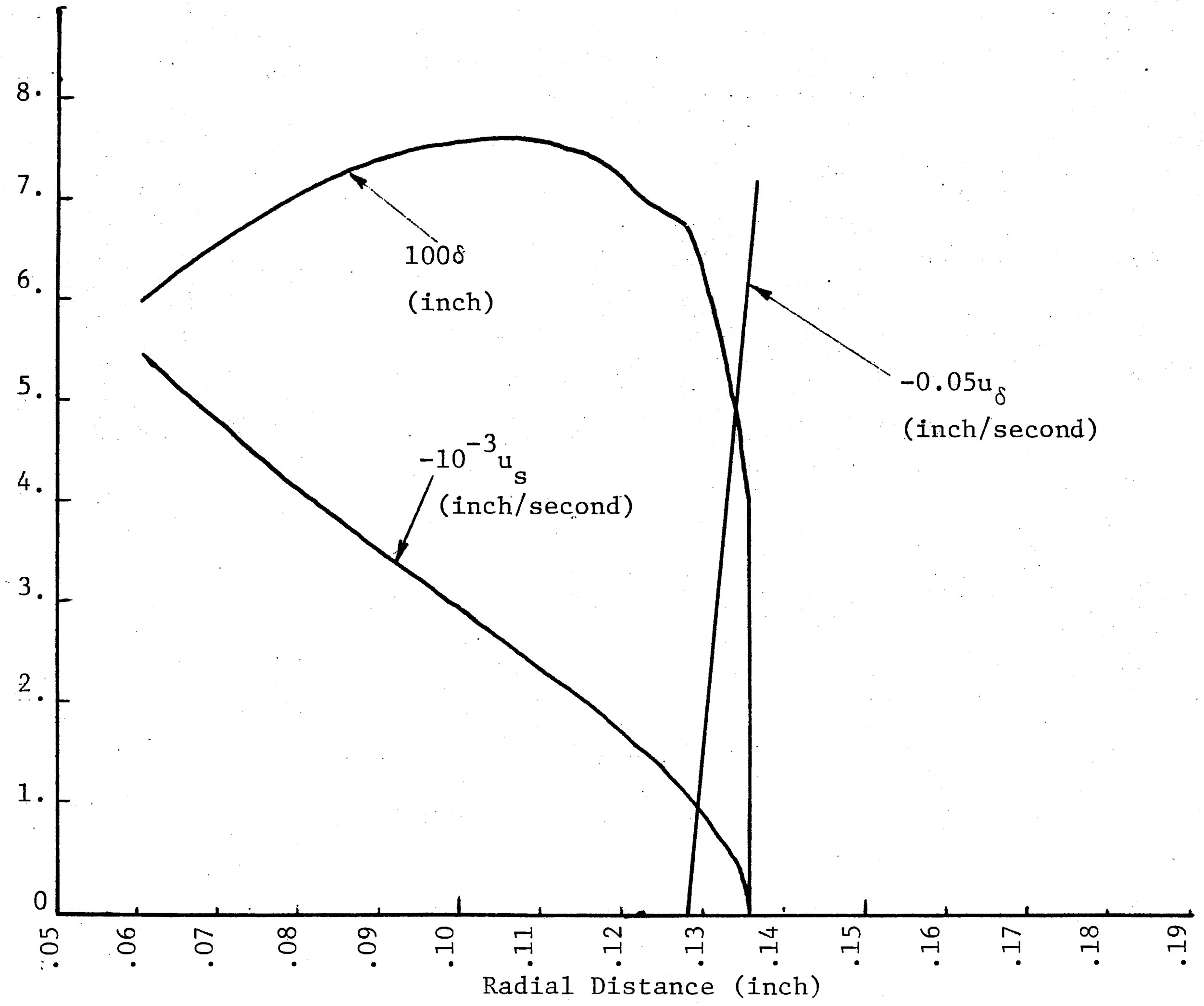

Figure 51. Radial Distributions of the Radial Velocity Functions (u_δ,u_s) and the Boundary Layer Thickness (δ) as Predicted by the Two-Dimensional Model

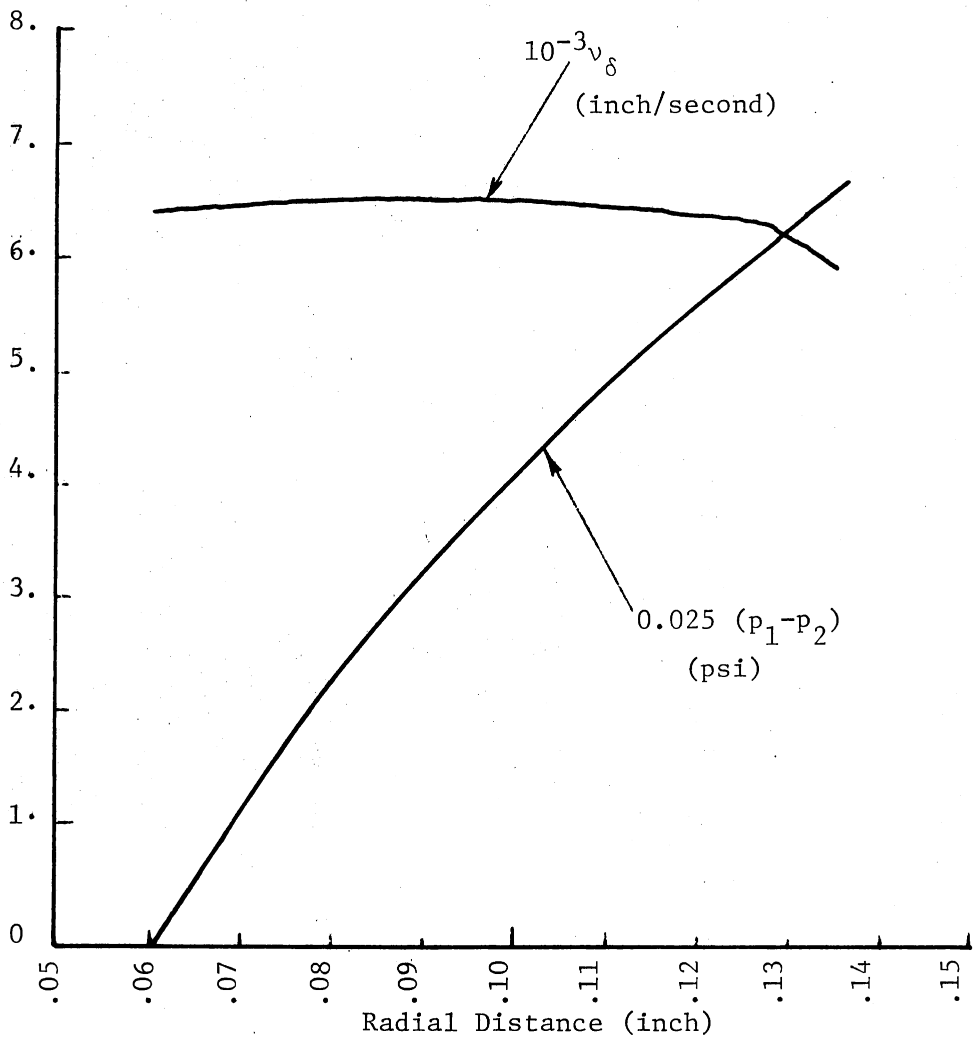

Figure. 52. Radial Distributions of Tangential Velocity and Pressure in the Vortex Chamber as Predicted by the Two-Dimensional Model

CHAPTER V

DYNAMIC BEHAVIOR OF NSVR

This chapter summarizes the development of an approximate analytical model which describes the dynamic behavior of the NSVR configuration, and the results of experimental transient response studies on one particular NSVR geometry.

V.1. Dynamic Model Development

A detailed discussion of the dynamic model development is given in Appendix E. The dynamic model employs the one-dimensional steady-state model (Chapter IV) with appropriate changes made to include primary dynamical effects. The orifices and the diffuser chamber are modeled as purely resistive elements. A time delay T_1 and a first-order lag T_2 characterize the propagation of the tangential velocity in the vortex chamber. The resulting mathematical model is nonlinear.

Linearization of the nonlinear model results in the following transfer function relating the principal variables of interest:

$$\frac{\Delta p_o}{\Delta p_i} = \frac{K_3(1-T_2D)}{1+T_2D+K_4\exp(-T_1D)} \qquad (1)$$

where K_3 and K_4 are constants defined in Appendix E. Equation 1 can be used for small-signal dynamic analysis.

V.1.1. Determination of the Time Delay T_1 and the Time Constant T_2

The time delay T_1 and the time constant T_2 are estimated by modeling the vortex chamber as a "tube" of width b and length L (see Figure 53). The time delay T_1 is assumed to be the time taken for the tangential velocity information to travel the length L. That is

$$T_1 = L/\bar{v} \tag{2}$$

where $\bar{v}$ is the average tangential velocity in the vortex chamber obtained from the steady-state analysis.

The time constant T_2 is obtained by considering the inertance I of the equivalent tube of length L and the overall steady-state resistance R of the vortex resistor. Therefore

$$T_2 = I/R \tag{3}$$

The inertance I is given by $\rho L/bh$.

V.1.2. Computed Step Response

The dynamic model constants (K_3, K_4, T_1 and T_2) are computed by using average flow conditions. Table II lists numerical values for an example problem. Flow variables (i.e. velocities and pressure) corresponding to zero flowrate are used as the initial conditions for the dynamic simulation.

Figure 54 shows the computed transient response of a NSVR (see Table II for geometry) subjected to a step input of 20 psi. The overshoot is due to the time delay T_1 associated with the tangential velocity propagation. Until the new tangential velocity information reaches the central orifice, the NSVR, exhibits a resistance value corresponding to

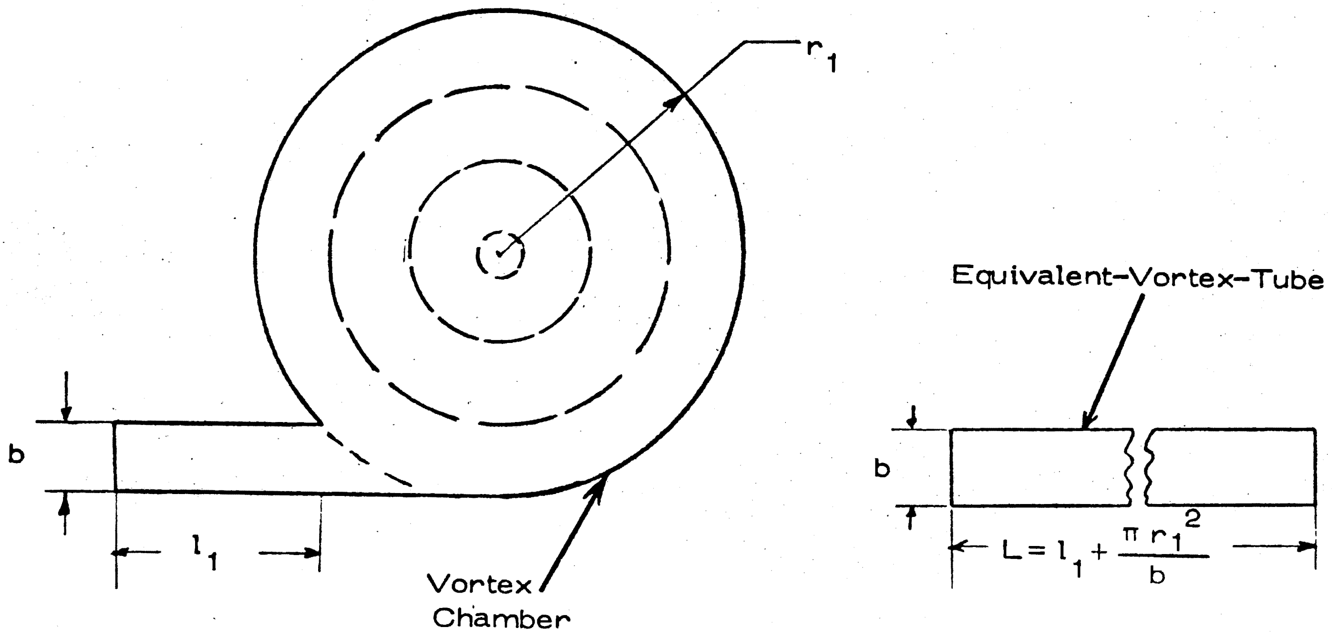

Figure 53. Tube-Equivalent of Vortex Chamber

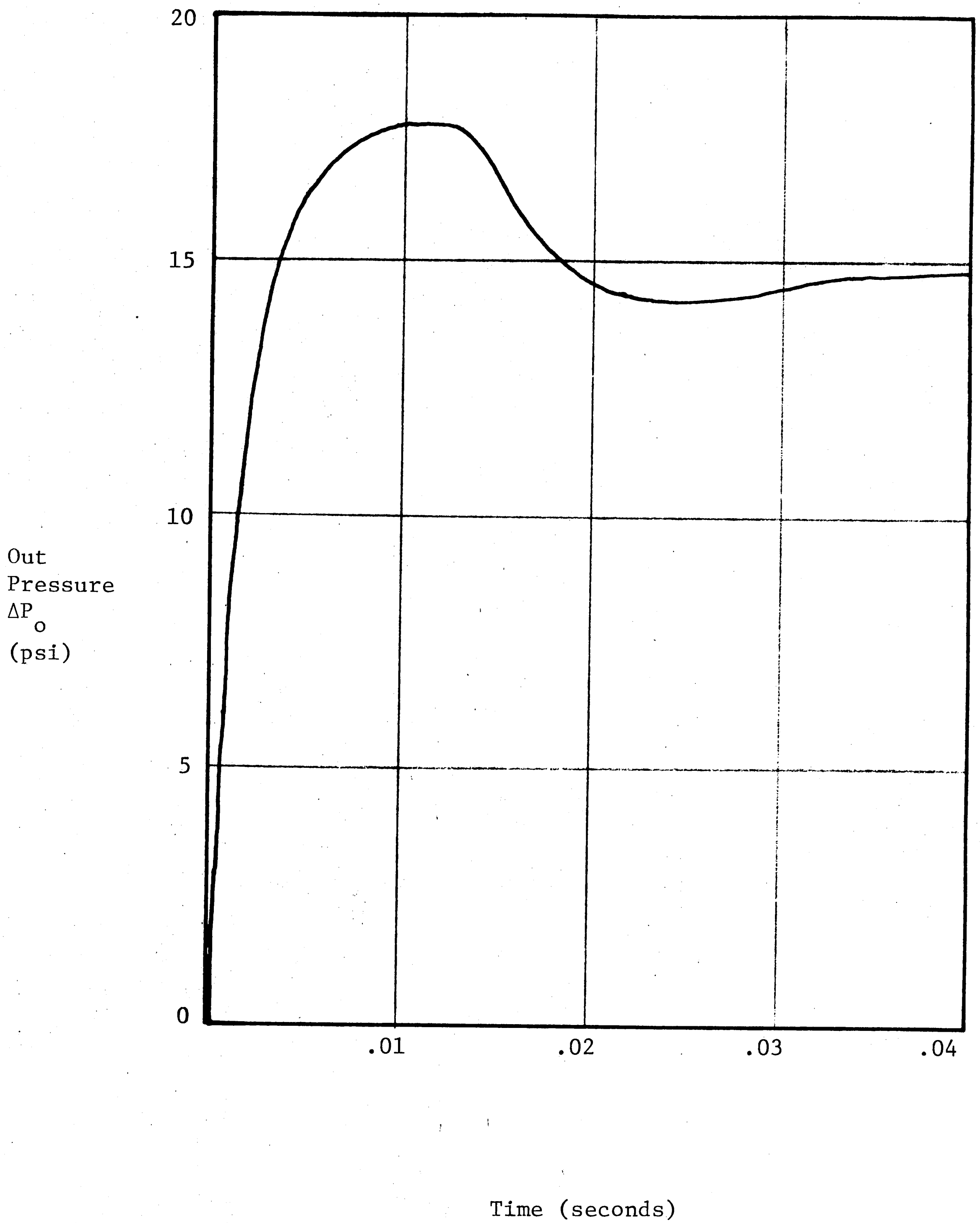

Figure 54. Computed Transient Response of the NSVR to a Step

TABLE II

DYNAMIC MODEL PARAMETERS - EXAMPLE

Geometry of NSVR

$b = 0.1500$ inch

$h = 0.3500$ inch

$l_1 = 0.1709$ inch

$r_1 = 0.2500$ inch

$r_2 = 0.1005$ inch

$l_2 = 0.4000$ inch

Model Coefficients

$L = 1.2743$ inch

$\bar{v} = 95.8423$ inch/sec.

$I = 1.8975 \times 10^{-3}$ lbf/sec^2/in^5

$R = 0.9000$ lbf.sec/in^5

$T_1 = 13$ milli-seconds

$T_2 = 2$ milli-seconds

$K_3 = 0.894596$

$K_4 = 0.199428$

---

the initial operating point. For a positive step input, this delay corresponds to a temporary increase in the resistance. The temporary decrease in flow rate caused by the delay, results in the overshoot observed in Figure 54. For a negative step input, there would exist a corresponding undershoot.

V.2. Experimental Study

V.2.1. Apparatus

Figure 55 shows a schematic of the apparatus used in the experimental study of the dynamic behavior of vortex resistors. The hydraulic system used was the same as that used for the steady-state experiments. A quick opening solenoid valve (3/16 inch orifice diameter) was employed to generate a transient input at the upstream or downstream end of the vortex resistor. An accumulator and a flow bypass path (using a needle valve) was used to minimize pressure fluctuations upstream of the solenoid valve, during and after sudden opening of the valve. A fixed resistor (shorttube orifice L=0.2500", D=0.0625") was connected at the downstream end of the vortex resistor to simulate a typical load. The instantaneous pressure drop across this "load" orifice was a measure of the instantaneous flow-rate at the exit of the vortex resistor. Figure 56 shows the dimensions of the end blocks of the vortex resistor and the pressure transducer locations.

V.2.2. Instrumentation

Kistler Piezoelectric Model 601A transducers with Model 504A charge amplifiers were used to measure the time dependent pressures at the inlet and exit of the vortex resistor. The long time constant

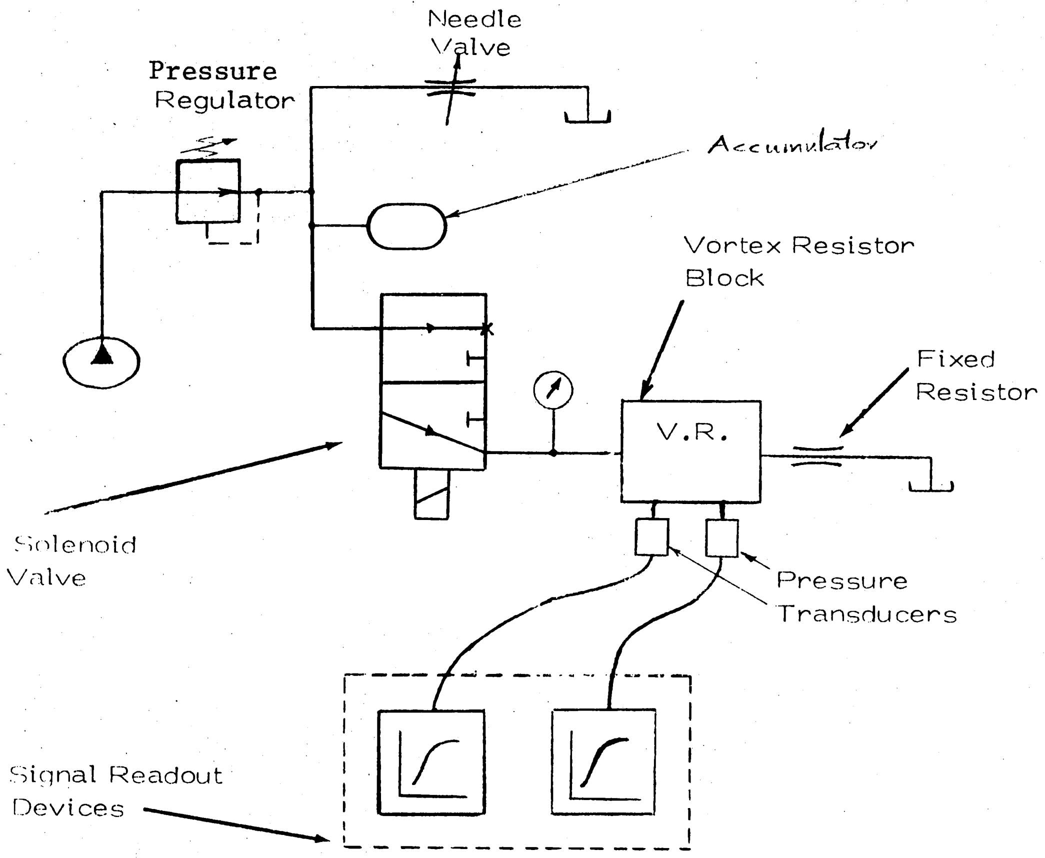

Figure 55. Schematic of Transient Response Experiment (Solenoid Valve was Located at the Downstream of Vortex Resistor in Some Cases)

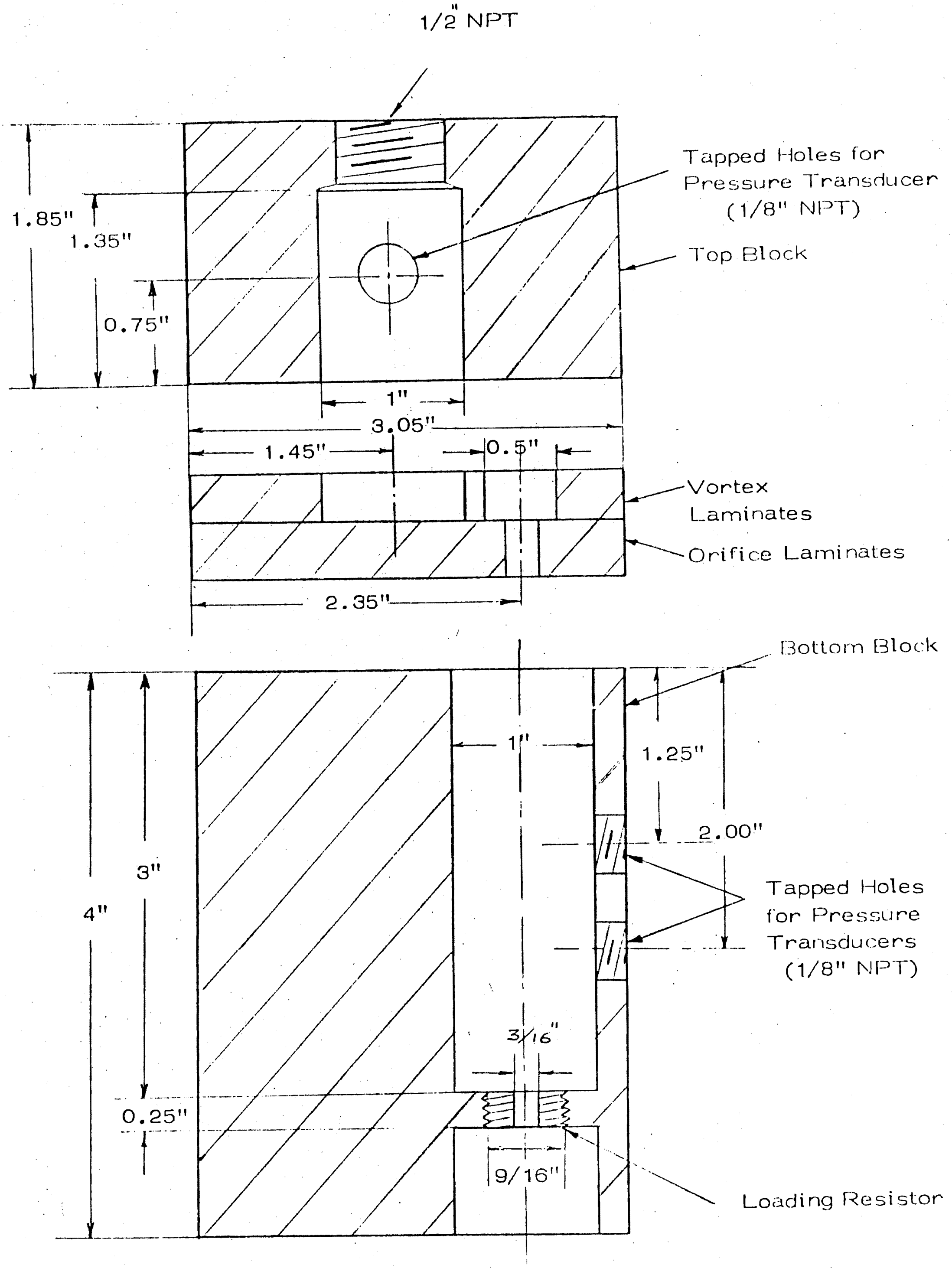

Figure 56. Vortex Resistor Block

setting on the charge amplifiers permitted the static calibration of the pressure measuring system. The temperature measurement system used in steady-state experiment was used to measure the average temperatures during the dynamic response tests. The temperature of the hydraulic oil was relatively constant (within ± 1°F) during the transient response tests.

The input and output pressure signals (from the upstream and downstream of the vortex resistor) were displayed on a Tektronix Model 502 dual-beam oscilloscope. Polaroid pictures were taken of the oscilloscope traces.

V.2.3 Experimental Results

Figure 57 shows a typical response obtained on an NSVR configuration. A positive step input was applied by suddenly opening the solenoid valve located at the upstream end of the vortex resistor block. The rise time of the pressure "step" input was of the order of 10 milliseconds; this was the shortest rise time possible with the available components. No discernable pure time delay or first-order lag is evident on the transient response traces of Figure 57.

Figure 58 shows a transient response trace taken for a somewhat higher pressure step input. The high frequency noise in the input was due to a short term oscillation of the pressure regulator.

In an effort to sharpen the input pressure signal, a negative step was used. The negative step input was generated by locating the solenoid valve between the downstream end of the vortex resistor and the loading resistor. The rise time obtained was of the order of 4 milliseconds. Figures 59 and 60 show transient responses for two different

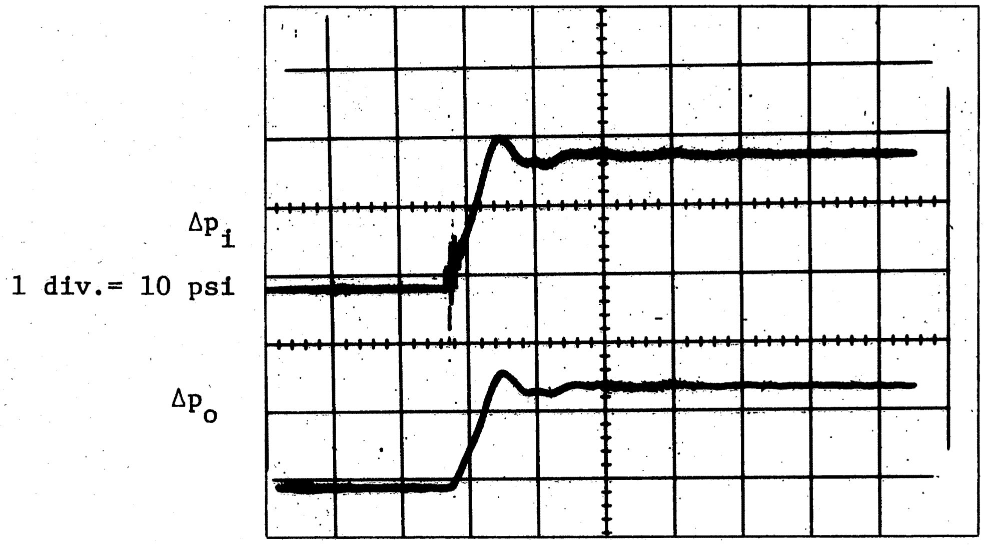

1 div. = 20 milli-seconds

Figure 57. Transient Response of an NSVR to a Positive Step Input

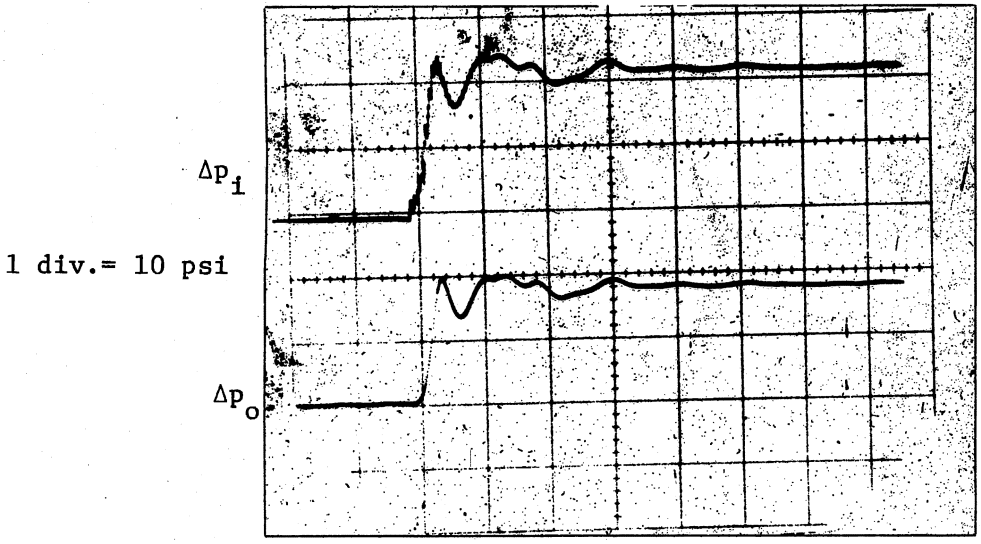

1 div. = 20 milli-seconds

Figure 58. Transient Response of an NSVR to a Positive Step Input

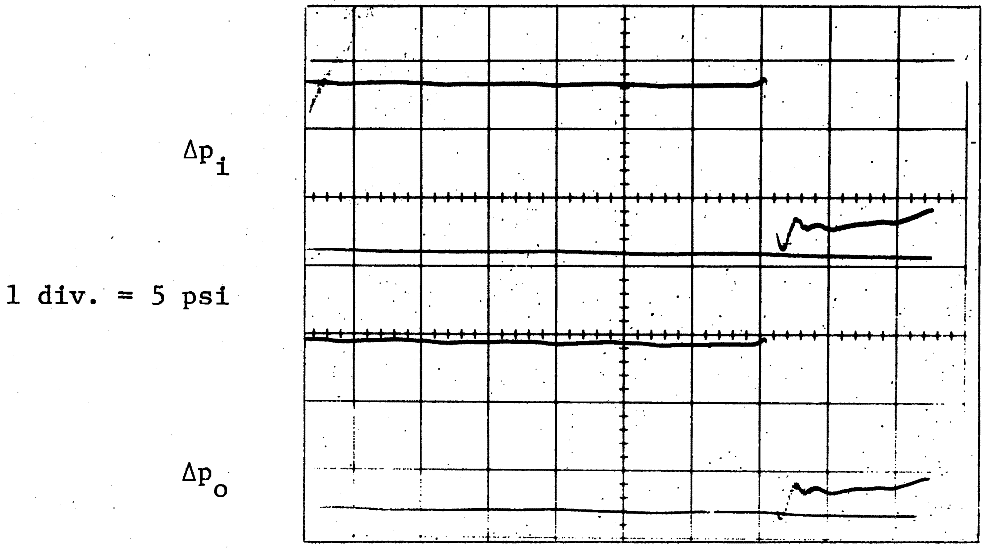

1 div. = 10 milli-seconds

Figure 59. Transient Response of an NSVR to a Negative Step Input (Loading Orifice Diameter = 0.1250 inch)

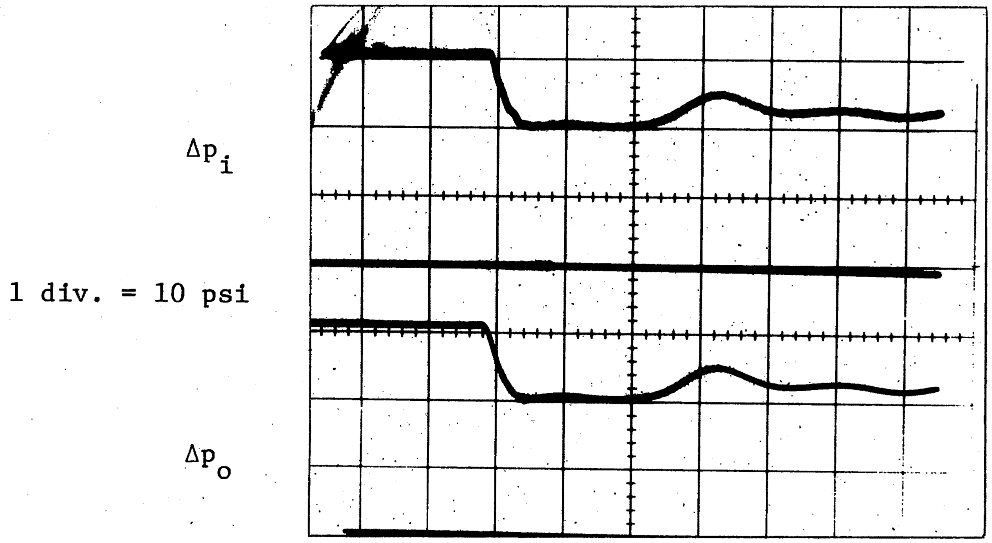

1 div. = 10 milli-seconds

Figure 60. Transient Response of an NSVR to a Negative Step Input (Loading Orifice Diameter = 0.0625 inch)

loading resistors at the downstream of the vortex resistor. No discernable dynamics are evident from these traces. The resolution obtainable from the scope photographs is of the order of 0.5 millisecond. Therefore, delays or time constants smaller than 0.5 millisecond are not observable.

V.3. Comparison of Theory and Experiment

The rise time experimental input was considered too long to permit a direct comparison of experimental data with the predicted step response of Figure 54. A terminated-ramp-type input signal having a rise time of 10 milliseconds approximates the experimental input condition. Figure 61 compares the experimental and predicted dynamic responses for this ramp input. The model predicts the basic dynamic behavior well in a qualitative sense, even though there appears to be some error in T_1 and T_2. More accurate estimation of the time constants T_1 and T_2 may be possible using a distributed parameter approach similar to that used by Anderson [31], but the procedure presented in this chapter is probably adequate for most purposes.

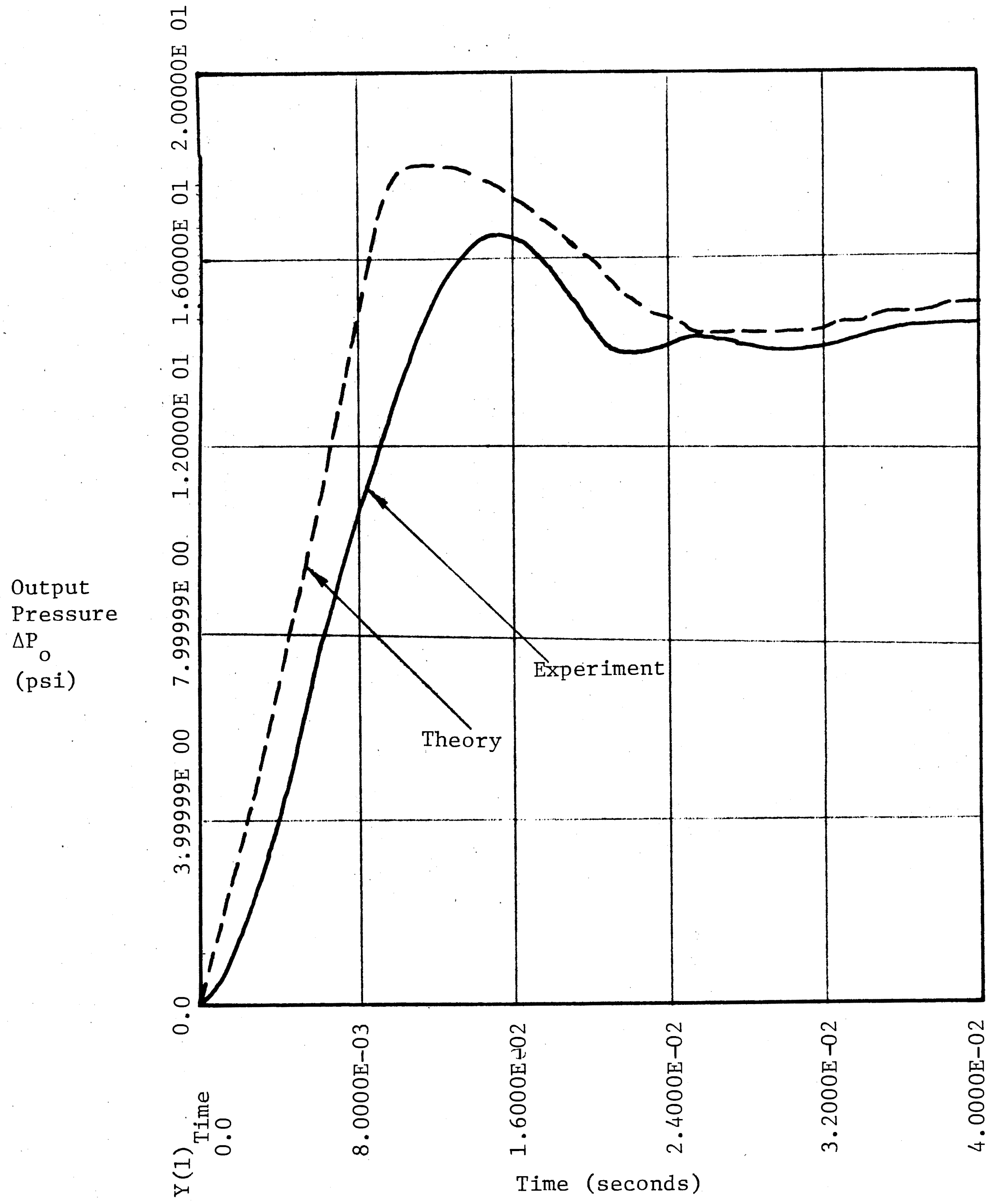

Figure 61. Comparison of Experimental and Computed Transient Responses of a NSVR (to a Terminated Ramp Input)

CHAPTER VI

CONCLUSIONS AND RECOMMENDATIONS

VI.1. Conclusions

This study has established that (1) temperature-insensitive vortex resistors can be built in practical sizes, and (2) temperature compensation for fluid resistors of the orifice and capillary tube types can be provided by means of vortex resistors and (3) vortex resistors (operating on hydraulic oil) behave primarily as resistors with no appreciable reactive dynamics.

The empirical models discussed in Appendix A can be employed for designing vortex resistors having a given temperature sensitivity. The accuracy of these models cannot be insured for operation outside the range of the data base.

The one-dimensional anaytical models developed for the NSVR and SVR configurations can also be used for design purposes. These models are expected to be more accurate over a wider range of geometries and flow conditions than the empirical models. The empirical models do not include all the important geometrical parameters and are limited by constraints placed on the establishment of a data base through experimentation. The analytical models, include most of the variables believed to be of significance.

The two-dimensional model developed for the NSVR is more accurate than the one-dimensional model for some geometries, but it is not as efficient computationally due to the numerical integration required.

The dynamic model developed for the NSVR is only an approximate dynamic characterization of the resistor, but it is sufficiently accurate for most system dynamics needs. Model predictions as validated by transient response requirements, suggest that the dynamics of a vortex resistor are relatively unimportant compared to the dynamics of other principal elements in a typical fluid system which incorporates the resistor.

VI.2. Recommendations

The following areas are suggested for future studies:

1. The empirical models developed for the SVR and NSVR (low resistance direction) are limited in usefulness to a relatively small range of geometries, temperatures, and flow conditions. The most serious limitation of the data base used to develop the empirical models is the small temperature range (95° to 135°F) covered. Military and industrial specifications usually call for an operating temperature range of -50°F to 150°F. Additional data should be acquired in order to broaden the range of validity of the empirical models.

2. Velocity profiles in the vortex chamber should be measured to validate more fully the flow field assumptions which underly the two-dimensional model.

3. An improved diffuser model should be sought for the SVR

configuration. The model should take into account the secondary reverse flow in the diffuser. A momentum integral approach can be used for this purpose.

4. The dynamic response experiments conducted to date have established that the time constants associated with a typical vortex resistor (vortex chamber diameter = 0.5") are less than 0.5 milliseconds. More precise determination of these time constants would be difficult using typical size geometries. A more accurate dynamic characterization could be made by time-scaling transient response measurements on a large scale model. A distributed parameter model similar to Anderson's turbulent flow model [31] could be developed to more accurately predict the vortex chamber dynamics for the laminar flow case. This model would yield values for the time constants τ_1 and τ_2 to be used in the approximate lumped-parameter model.

5. Algorithms and computer programs should be developed to allow efficient use of the analytical models as design tools.

BIBLIOGRAPHY

[1] Thoma, D. "Fluid Lines," U. S. Patent No. 1,839,618, Patented 5 January 1932.

[2] Technical Hydraulic Handbook, The Lee Company, Westbrook, Connecticut, 1971.

[3] Paul. F. W. "Steady-State Performance of Fleuric Diodes." (Unpub. Ph.D. dissertation, Lehigh University, 1968.)

[4] Kidd, G. J., Jr. and G. J. Farris. "Potential Vortex Flow Adjacent to a Stationary Surface," ASME Paper No. 68-APM-15.

[5] Hoffmann, J. A. "Similarity Solutions for the Interaction of a Potential Vortex with Free Stream Sink Flow and a Stationary Surface," Trans. ASME, Journal of Fluids Eng'g.,Vol. 96, No.1 (March, 1974), pp. 49-54.

[6] Von Kármán, T. "Uber laminare und turbulente Reibung," Zeits, Ang. Math. Mech. I (August, 1921), pp. 233-252.

[7] Boyack, B. E., and W. Rice. "Integral Method for Flow Between Rotating Disks," Trans. ASME, Journal of Basic Eng'g., Series D, Vol. 93, No. 3 (September, 1971), pp. 350-354.

[8] Rott, N., and W. S. Lewellen. "Boundary Layers and Their Interactions in Rotating Flows," Progress in Aeronautical Sciences, Vol. 7 (1966), pp. 111-144.

[9] Wormley, D. N. "Analytical Model for the Incompressible Flow in Short Vortex Chambers," Trans. ASME, Journal of Basic Eng'g., Series D, Vol. 91, No. 1 (June, 1969), pp. 264-276.

[10] Kwok, C. C. K., N. D. Thinh, and S. Lin. "An Investigation of Confined Vortex Flow Phenomena," Trans. ASME, Journal of Basic Eng'g., Series D, Vol. 94, No. 3 (September, 1972), pp. 689-696.

[11] Taplin, L. B. "Small Signal Analysis of Vortex Amplifiers," Chapter 7, AGARDograph, 118 (December, 1968), pp. 235-295.

[12] Bichara, R. T., and P. A. Orner. "Analysis and Modeling of the Vortex Amplifier," Trans. ASME, Journal of Basic Eng'g., Series D, Vol. 91, No. 1 (December, 1969), pp. 755-763.

[13] Farris, G. J., G. J. Kidd, Jr., D. W. Lick, and R. E. Textor. "A Theoretical and Experimental Study of Confined Vortex Flow," Trans. ASME, Journal of Applied Mechanics, Series E, Vol. 91, No. 4 (December, 1969), pp. 687-692.

[14] Hondour, Y. T., and C. W. Rezek. "Hydraulic Vortex Valve, Modeling and Design," ASME Paper No. 74-WA/Aut-19, (1974).

[15] Taylor, G. I. "The Boundary Layer in the Converging Nozzle of a Swirl Atomizer," Quarterly Journal of Mechanics and Applied Mathematics, Vol. 3 (1950), pp. 129-140.

[16] Weber, H. E. "The Boundary Layer Inside a Conical Surface Due to Swirl," Trans. ASME, Journal of Applied Mechanics, Series E, Vol. 78, No. 4 (December, 1956), pp. 587-592.

[17] Lichtarowicz, A., R. K. Duggins, and E. Markland. "Discharge Coefficients for In-compressible Non-Cavitating Flow Through Long Orifices," Journal of Mechanical Engineering Sciences, Vol. 7, No. 2 (1965), pp. 210-219.

[18] Reid, K. N. "Static Characteristics of Fluid Amplifiers," Proceedings of the Fluid Power Research Conference, Oklahoma State University, July 25-26, 1967.

[19] Jansen, W. "Rotating Stall in a Radial Vaneless Diffuser," Trans. ASME, Journal of Basic Eng'g., Series D, Vol. 86, No. 4 (December, 1964), pp. 750-758.

[20] Jansen, W. "Steady Fluid Flow in a Radial Vaneless Diffuser," Trans. ASME, Journal of Basic Eng'g., Series D, Vol. 86, No. 3 (September, 1964), pp. 607-619.

[21] Daily, J. W., and R. E. Nece. "Chamber Dimension Effects on Induced Flow and Frictional Resistance of Enclosed Rotating Disks," Trans. ASME, Journal of Basic Eng'g., Series D, Vol. 82, No. 1 (March, 1960), pp. 217-232.

[22] Miloh, T., and M. Poreh. "The Resistance to Rotation of Free Enclosed Disks," Trans. ASME, Journal of Applied Mechanics, Series E., Vol. 93, No. 4 (December, 1971), pp. 749-755.

[23] Sarpkaya, T. "A Theoretical and Experimental Investigation of the Vortex-Sink Angular Rate Sensor," Proceedings of the HDL Amplification Symposium, Vol. II (October, 1965).

[24] Sarpkaya, T., J. M. Goto, and J. M. Kirshner. "A Theoretical and Experimental Study of Vortex Rate Gyro," Advances in Fluidics, (May, 1967).

[25] Ostdiek, A. J. Viscous Vortex Rate Sensor, Technical Report No. TR-1555, Harry Diamond Laboratories, (November, 1971).

[26] Duff, J., K. Foster, and D. G. Mitchell. "Some Experiments on the Vortex Valve," First Cranfield Fluidics Conference, British Hydromechanical Research Association, Cranfield, England (1965).

[27] Knapp, A. B. "The Development and Control of a Vented Vortex Amplifier," Third Cranfield Fluidics Conference, British Hydromechanical Research Association, Cranfield, England, (1968).

[28] Taplin, L. B. "Phenomenology of Vortex Vlow and its Applications to Signal Amplification," Paper at Engineering Seminar on Fluid Control Systems, Pennsylvania State University Engineering Proceedings (1967), p. 45.

[29] Krishner, J. M., and S. Katz. Design Theory of Fluidic Components. New York: Academic Press, 1975, pp. 276-310.

[30] Bell, A. C. "Optimization of a Vortex Valve," (Unpub. M. S. thesis, Massachusetts Institute of Technology, 1965.)

[31] Anderson, W. W. "A Dynamic Model of Vortex-Type Fluid Amplifier," (Unpub. Ph.D. dissertation, Massachusetts Institute of Technology, 1971.)

[32] Schlichting, H. Boundary-Layer Theory. 6th ed., New York: McGraw-Hill Book Co., Inc., 1941.

[33] "Steady-State Characteristics of Vortex Resistors: Experimental Data," Supplement to the report submitted by Oklahoma State University to Harry Diamond Laboratories under contract no. DAAG39-74-R-9621, February, 1976.

APPENDIX A

STEADY-STATE EMPIRICAL MODELS

A.1. Basic Model

The geometries of the NSVR and the SVR are described by six length parameters (see Figure 4): b, h, l_1, r_1, r_2, and l_2. Due to symmetry, the diffuser chamber dimensions are the same as those of Vortex chamber for an SVR. The steady-state characteristic of a fluid resistor may be described by a functional relationship between the volumetric flow rate (for incompressible flow situations) and the pressure drop across the resistor. This functional dependence involves the geometry of the resistor and relevant physical properties (density and viscosity in this case) of the fluid. In the case of the vortex resistor this relationship may be expressed as follows:

$$Q = Q(b, h, l_1, r_1, r_2, l_2, \Delta P, \rho, \mu) \qquad (A.1)$$

For purpose of scaling, it is necessary to normalize the variables. The following dimensionless parameters may be defined based on the variables of equation (A.1):

$$\frac{r_1^4 \Delta P}{\rho Q^2}, \frac{Q}{r_1 \nu}, \frac{b}{r_1}, \frac{h}{r_1}, \frac{l_1}{r_1}, \frac{r_2}{r_1}, \frac{l_2}{r_1}$$

The choice of r_1 as the characteristic length is arbitrary. Equation (A.1) may be replaced by

$$\frac{r_1^4 \Delta P}{\rho Q^2} = f\left(\frac{Q}{r_1 \nu}, \frac{b}{r_1}, \frac{h}{r_1}, \frac{l_1}{r_1}, \frac{r_2}{r_1}, \frac{l_2}{r_1}\right) \qquad (A.2)$$

The function f can be any function that fits the experimental data within the desired accuracy. However, the choice of the function f is governed by mathematical simplicity and ease of numerical manipulation. From this point of view, a reasonable functional form would be as follows:

$$\frac{r_1^4 \Delta P}{\rho Q^2} = a_1 \left(\frac{b}{r_1}\right)^{a_2} \left(\frac{h}{r_1}\right)^{a_3} \left(\frac{l_2}{r_1}\right)^{a_3} *$$

$$\left(\frac{Q}{r_1 \nu}\right)^{a_5} \left(\frac{l_1}{r_1}\right)^{a_6} \left(\frac{r_2}{r_1}\right)^{a_7} \qquad (A.3)$$

where a_1, a_2, ..., a_7 are constants. These constants can be determined by linear regression using experimental data.

A.2. Data Base

Ideally the experimental data to be used for an empirical model development should envelop with a fine grid the entire range of useful geometries and flow situations. However, practical considerations make such an exhaustive data acquisition infeasible. Therefore, a limited number of geometries were selected and tested under a few judiciously selected flow situations. Various factors were involved in the selection of the geometries and the operating conditions. These factors are discussed below.

For the NSVR configuration, 24 geometries were selected close to the geometrical proportions of the Lee Visco Jet #62AVL 1 (see reference [2]) which was observed to have a negative $\partial Q/\partial T$ while operating on MIL-5606 hydraulic oil. Of the five geometrical ratios (i.e., b/r_1, h/r_1, l_1/r_1, r_2/r_1, and l_2/r_1), only three were considered as having a strong influence on the vortex characteristics. These ratios were b/r_1, h/r_1, and r_2/r_1. This simplification was necessary to limit the number of geometries to a manageable number.

The vortex chamber radius r_1 was selected to be 0.250". Although smaller values of r_1 would likely be used in most fluidic applications, the dimensional accuracy afforded by the available machining equipment prohibited a smaller value of r_1 for the experiments reported here. Figure 51 shows the grid locations of the 24 geometries used. The dimensions of these geometries are given in Table III. In each of the six vertical planes of Figure 62 four geometries were selected, thereby allowing uniform spanning of the geometrical space. The geometries were staggered to decouple the space variables. Otherwise, the selection of the geometries was arbitrary. The data obtained on 24 geometries for an NSVR operating in the high resistance direction of flow is considered adequate for development of the NSVR model.

Additional experimental data were obtained for the SVR configuration and for flow in the low resistance direction of the NSVR. The ratio r_2/r_1 was held constant for these data. These data were primarily intended for evaluation of the analytical model. Therefore, only a few geometries were selected from the available laminations (see Table IV) The number of geometries used, i.e. 8, is not sufficient to develop an empirical model valid over a wide range of operating conditions. However, the empirical models developed using these limited experimental data can provide at least approximate estimates of the steady-state characteristics of the SVR and of the NSVR operating in the low resistance flow direction.

TABLE III

GEOMETRIES OF THE NSVR

Geometry Number	b (in)	h (in)	l_1 (in)	d_1 (in)	d_2 (in)	l_2 (in)
1	0.05	0.25	0.2500	0.5	0.0625	0.20
2	0.20	0.25	0.1550	0.5	0.1250	0.25
3	0.25	0.25	0.1500	0.5	0.2010	0.40
4	0.10	0.25	0.2000	0.5	0.2500	0.50
5	0.10	0.30	0.2000	0.5	0.1250	0.25
6	0.05	0.30	0.2500	0.5	0.1495	0.30
7	0.15	0.30	0.1709	0.5	0.2010	0.40
8	0.25	0.30	0.1500	0.5	0.2500	0.50
9	0.10	0.35	0.2000	0.5	0.0625	0.20
10	0.15	0.35	0.1709	0.5	0.1495	0.30
11	0.05	0.35	0.2500	0.5	0.2010	0.40
12	0.20	0.35	0.1550	0.5	0.2500	0.50
13	0.20	0.40	0.1550	0.5	0.0625	0.20
14	0.15	0.40	0.1709	0.05	0.1250	0.25
15	0.25	0.40	0.1500	0.5	0.1495	0.30
16	0.05	0.40	0.2500	0.5	0.2500	0.50
17	0.15	0.45	0.1709	0.5	0.0625	0.20
18	0.05	0.45	0.2500	0.5	0.1250	0.25
19	0.10	0.45	0.2000	0.5	0.1495	0.30
20	0.25	0.45	0.1500	0.5	0.2010	0.40
21	0.25	0.50	0.1500	0.5	0.0625	0.20
22	0.05	0.50	0.2500	0.5	0.1495	0.30
23	0.20	0.50	0.1550	0.5	0.2010	0.40
24	0.15	0.50	0.1709	0.05	0.2500	0.50

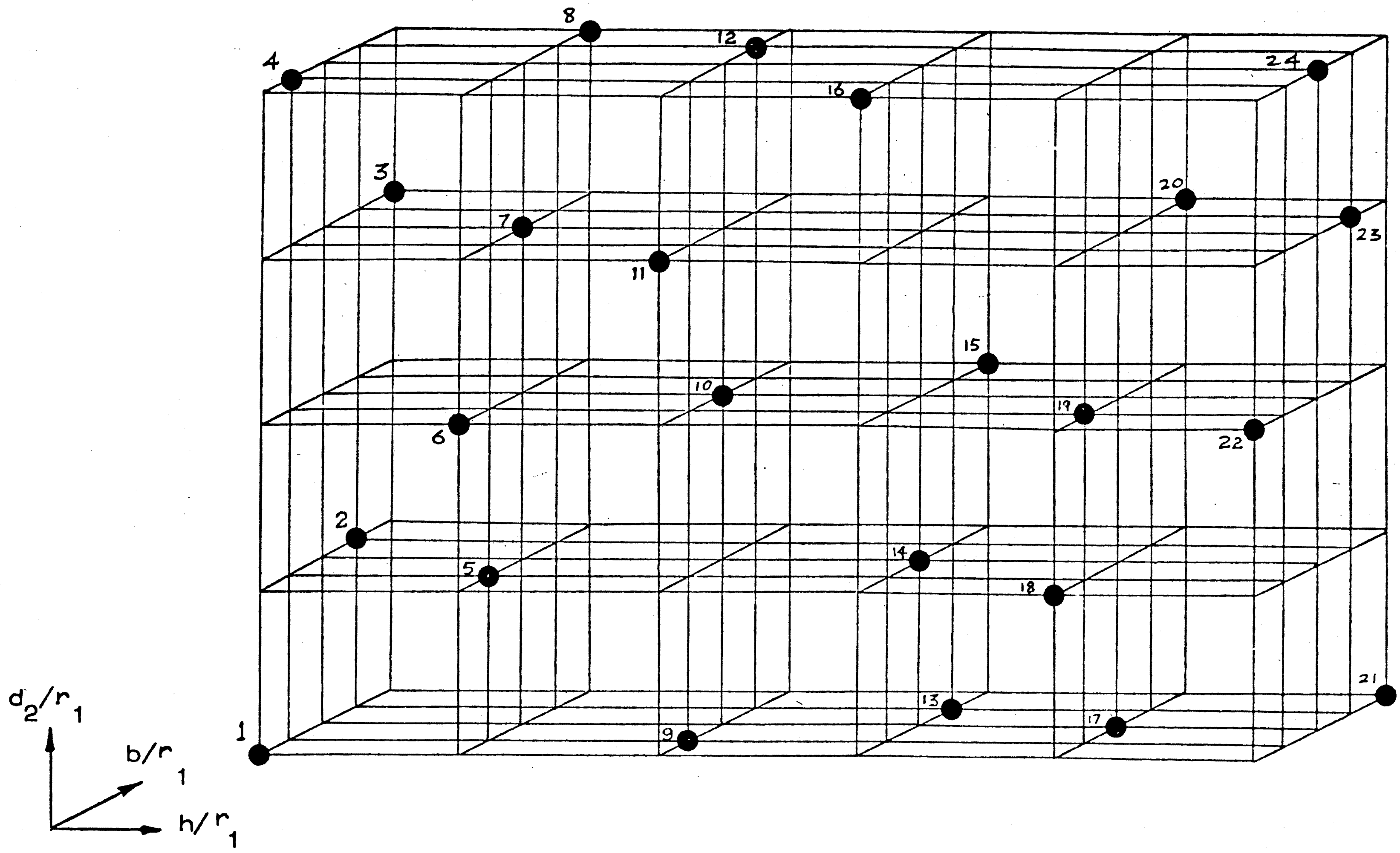

Figure 62. Location of Geometries Selected for Empirical Study (See Table 1 for Dimensions of the Geometries)

TABLE IV

GEOMETRIES OF THE VORTEX RESISTORS (CONSTRUCTED BY AIR RESEARCH CORPORATION)

Geometry Number	b (in)	h (in)	l_1 (in)	d_1 (in)	d_2 (in)	l_2 (in)
1	0.02845	0.060	0.29795	0.27260	0.120	0.010
2	0.02845	0.060	0.29795	0.27260	0.120	0.070
3	0.04775	0.030	0.22700	0.28342	0.120	0.010
4	0.04775	0.030	0.22700	0.28342	0.120	0.070
5	0.02845	0.030	0.29795	0.27260	0.120	0.070
6	0.02845	0.060	0.28650	0.28342	0.120	0.010
7	0.03675	0.060	0.28650	0.28342	0.120	0.010
8	0.03675	0.060	0.28650	0.28342	0.120	0.070

A.3. Results

Table V lists the constants (a_i's) for the NSVR and the SVR for various flow situations. Figures 63-67 show correlations of the experimental data with the empirical models. The empirical predictions are within ten percent for most of the cases. In cases 2-4 the maximum error between model and data is less than 20 percent and in case 1 the error is within 30 percent.

From equation (A.3), with $a_6 = a_7 = 0$,

$$Q = \left[\frac{r_1^{4+a_5} \quad \Delta P}{\rho a_1 \left(\frac{b}{r_1}\right)^{a_2} \left(\frac{h}{r_1}\right)^{a_3} \left(\frac{l_2}{r_1}\right)^{a_4}} \right]^{\frac{1}{2+a_5}} \cdot \frac{a_5}{\nu^{2+a_5}} \qquad (A.4)$$

Differentiating with respect to the kinematic viscosity

$$\left.\frac{\partial Q}{\partial \nu}\right|_{\Delta P = \text{Constant}} = \frac{a_5}{2+a_5} \, C^{-\frac{2}{2+a_5}} \qquad (A.5)$$

where

$$C = \left[\frac{r_1^{4+a_5} \quad \Delta P}{\rho a_1 \left(\frac{b}{r_1}\right)^{a_2} \left(\frac{h}{r_1}\right)^{a_3} \left(\frac{l_2}{r_1}\right)^{a_4}} \right]^{\frac{1}{2+a_5}}$$

From Equation (A.5) and Table V it can be observed that the sign of the viscosity sensitivities ($\partial Q/\partial \nu$) for the NSVR (in reverse flow) and the SVR, are negative for low Reynolds' numbers and positive for high Reynolds' numbers. The sensitivities are always negative for the forward flow direction of the NSVR. A positive value of $\partial Q/\partial \nu$ implies that the flow rate increases with viscosity. A small magnitude of $\partial Q/\partial \nu$, as in the case of the NSVR (high resistance direction of flow) for the r_2/r_1

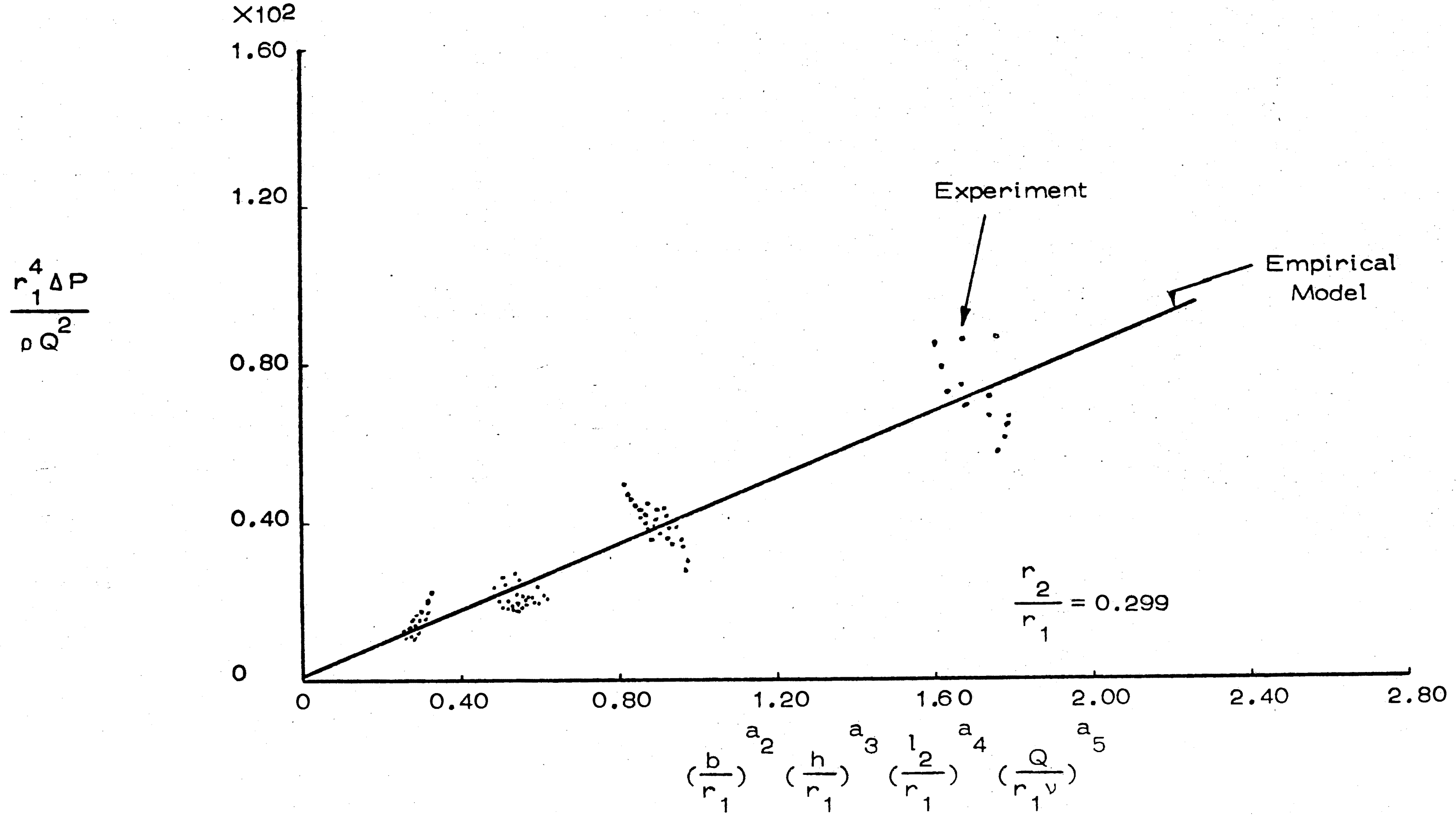

Figure 63. Empirical Model of NSVR Operating in High Resistance Flow Direction

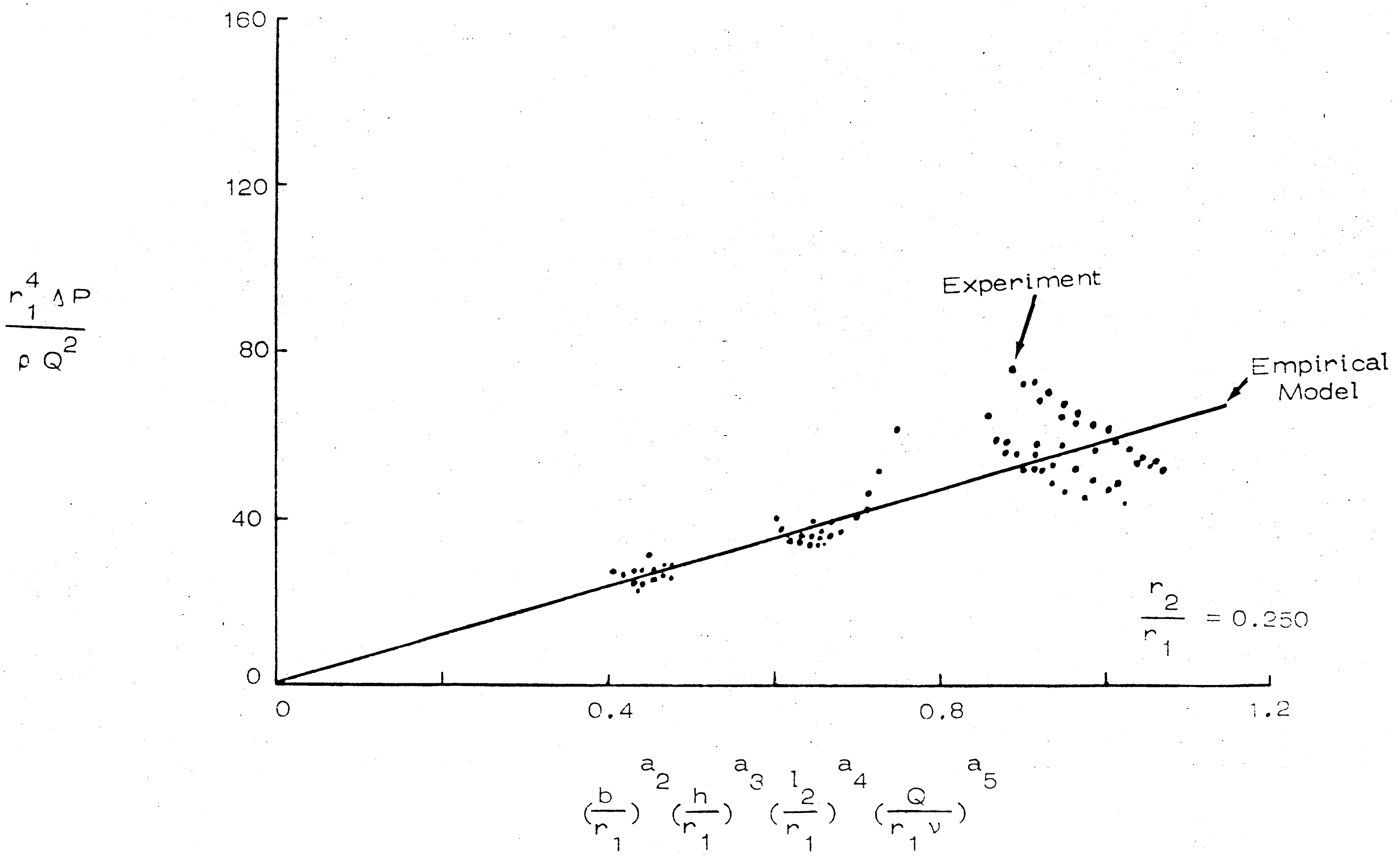

Figure 64. Empirical Model of NSVR Operating in High Resistance Flow Direction

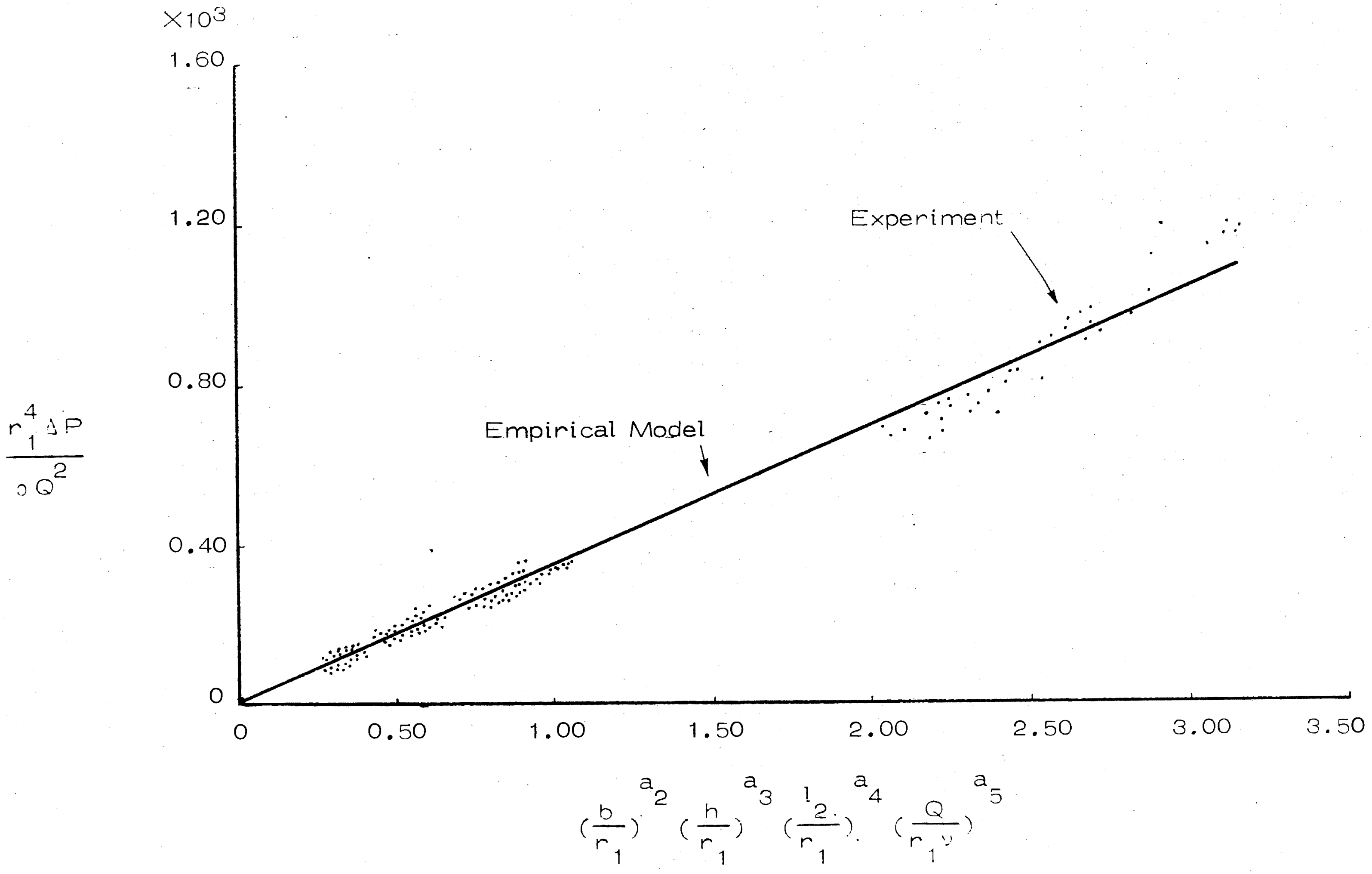

Figure 65. Empirical Model of NSVR for Flow in Low Resistance Flow Direction

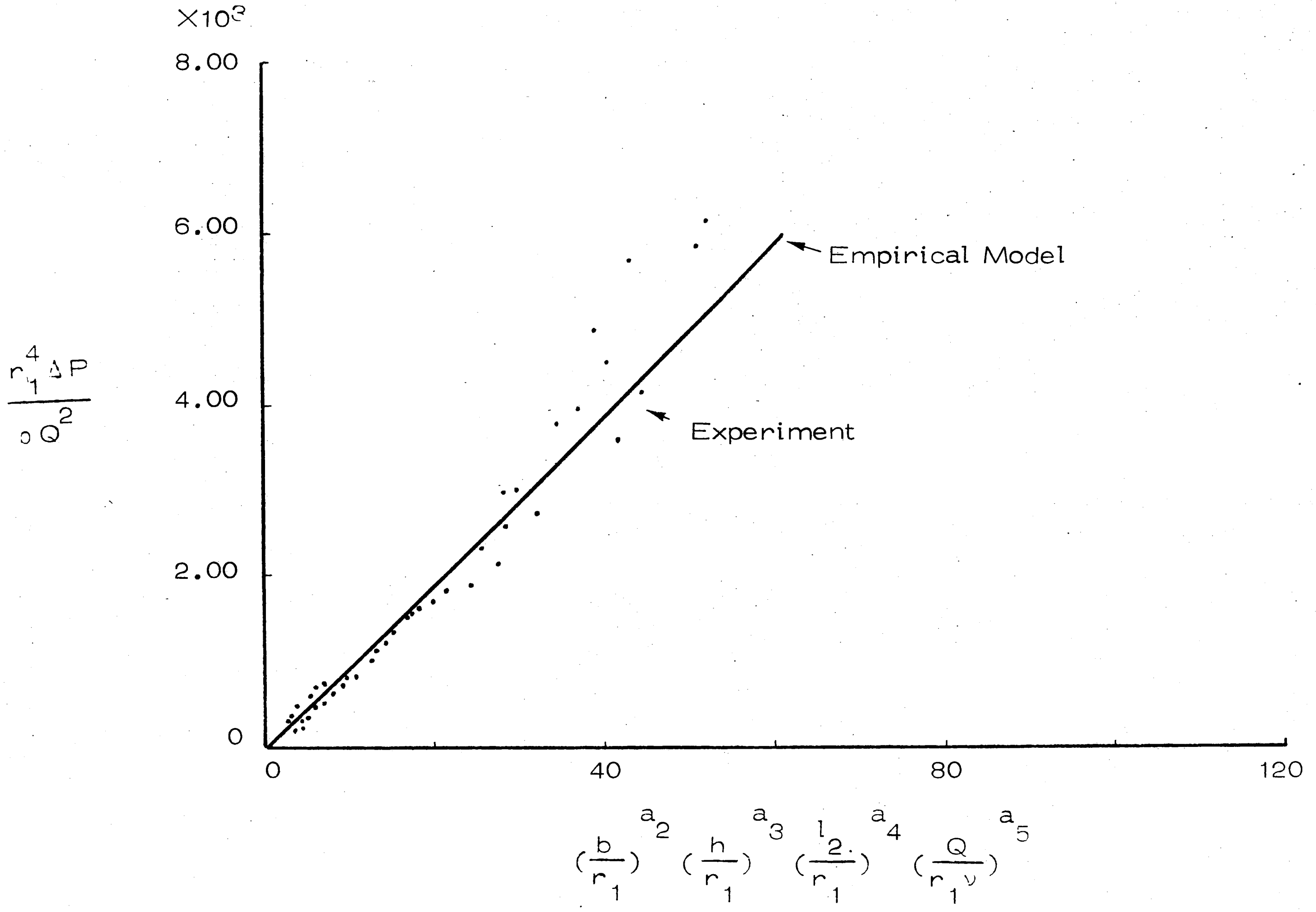

Figure 66. Empirical Model of SVR for Low $Q/r_1\nu$

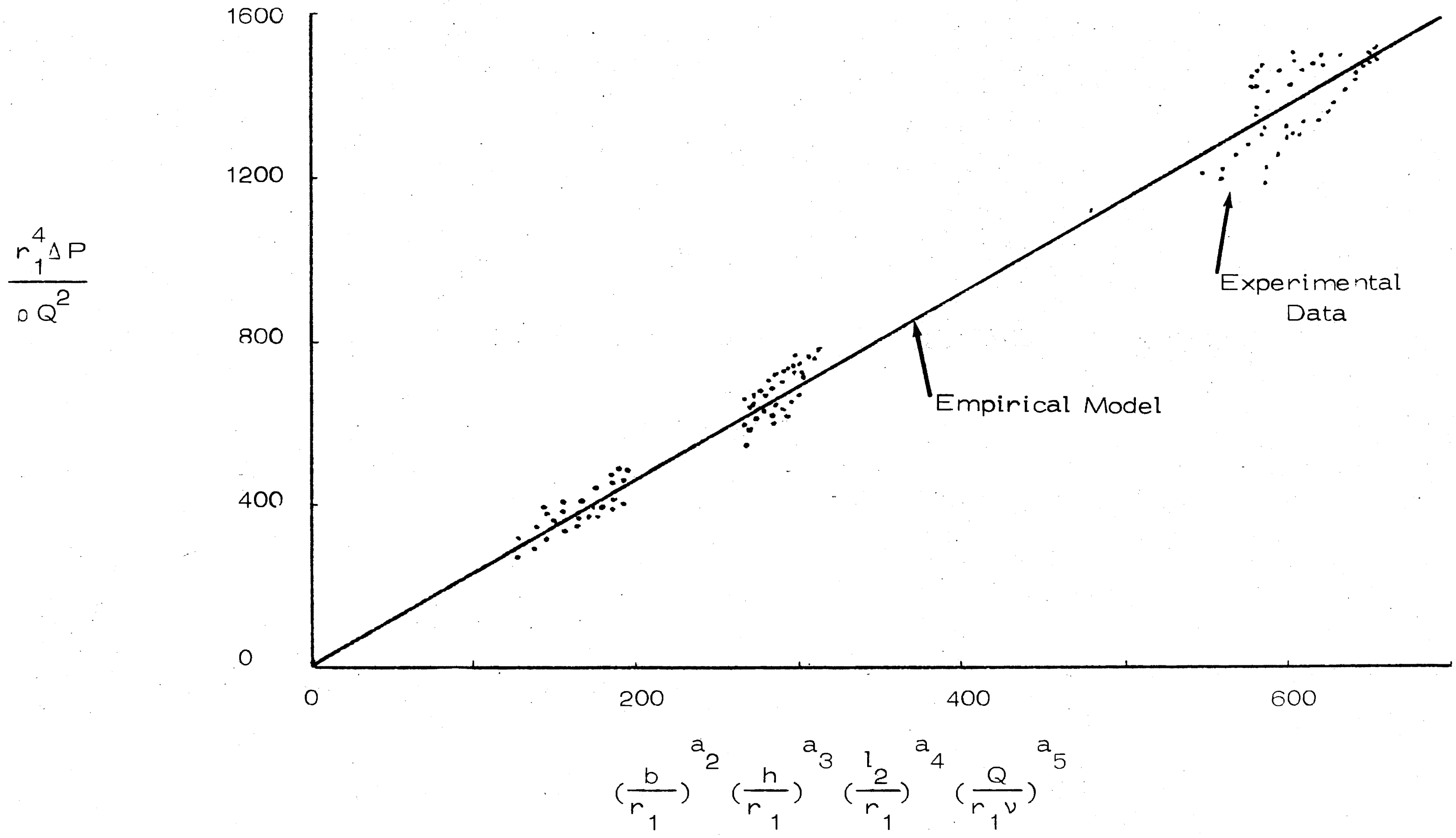

Figure 67. Empirical Model of SVR for High $Q/r_1\nu$

TABLE V

CONSTANTS OF EMPIRICAL MODELS

Case	Resistor Type	Flow Rate Range	a_1	a_2	a_3	a_4	a_5
1	NSVR High Resistance direction of flow	$100 < \frac{Q}{r_1 \nu} < 1000$	$a_1 = 2987.8402-34015.2540 + 146802.2200x^2 - 279280.1600x^3 + 195865.3207x^4$ $a_2 = 7.1037 - 110.3456x + 554.8653x^2 - 1187.7469x^3 + 902.3449x^4$ $a_3 = 3.340 - 56.0170x + 227.0982x^2 - 346.9231x^3 + 152.5452x^4$ $a_4 = 0$ $a_5 = -0.4937 + 10.8926x - 78.7254x^2 + 214.0315x^3 -194.2896x^4$ where $x \equiv r_2/r_1$				
2	NSVR Low Resistance direction of flow	$56 < \frac{Q}{r_1 \nu} < 1100$	3.424471	-2.213886	-2.052803	0.0047308	-0.2029383
3	SVR	$15 < \frac{Q}{r_1 \nu} < 400$	96.63902	-1.788208	-1.633816	-0.017810	-0.503094
4	SVR	$400 < \frac{Q}{r_1 \nu} < 1100$	2.289831	-1.816749	-1.839667	0.0114691	0.1379318

0.402 geometries indicates that the resistor is nearly temperature insensitive.

APPENDIX B

ONE-DIMENSIONAL MODEL OF NSVR

Figure 68 shows the four regions of the NSVR which can be individually modeled. The equations derived here are similar to those of reference [12] but with modifications for operation in laminar regime. Also reference [12] does not include region 4 of Figure 68. Further, due to operation in laminar regime the discharge coefficient of inlet orifice is not treated as constant but is allowed to vary with the Reynolds number. The basic assumptions are:

1. The fluid is incompressible and Newtonian,
2. The flow is laminar throughout the device,
3. No heat transfer,
4. All surfaces are smooth and geometrically exact,
5. No body forces,
6. The operating fluid properties are assumed constant throughout the flow field.

Additional assumptions are described in the sections which follow.

B.1. Region 1

Figure 69 shows region 1 of the NSVR (same as region 1 of SVR).

B.1.1. Assumptions

1. A shear stress based on the flat plate Blassius profile is assumed to exist on the annular surface of region 1.

2. The radial and tangential velocities and pressure are uniform over the annular surface of region 1.

3. The discharge coefficient of the inlet passage is the same as that of an equivalent circular short tube orifice with sharp-edged entry even though the downstream conditions are not the same for the two cases.

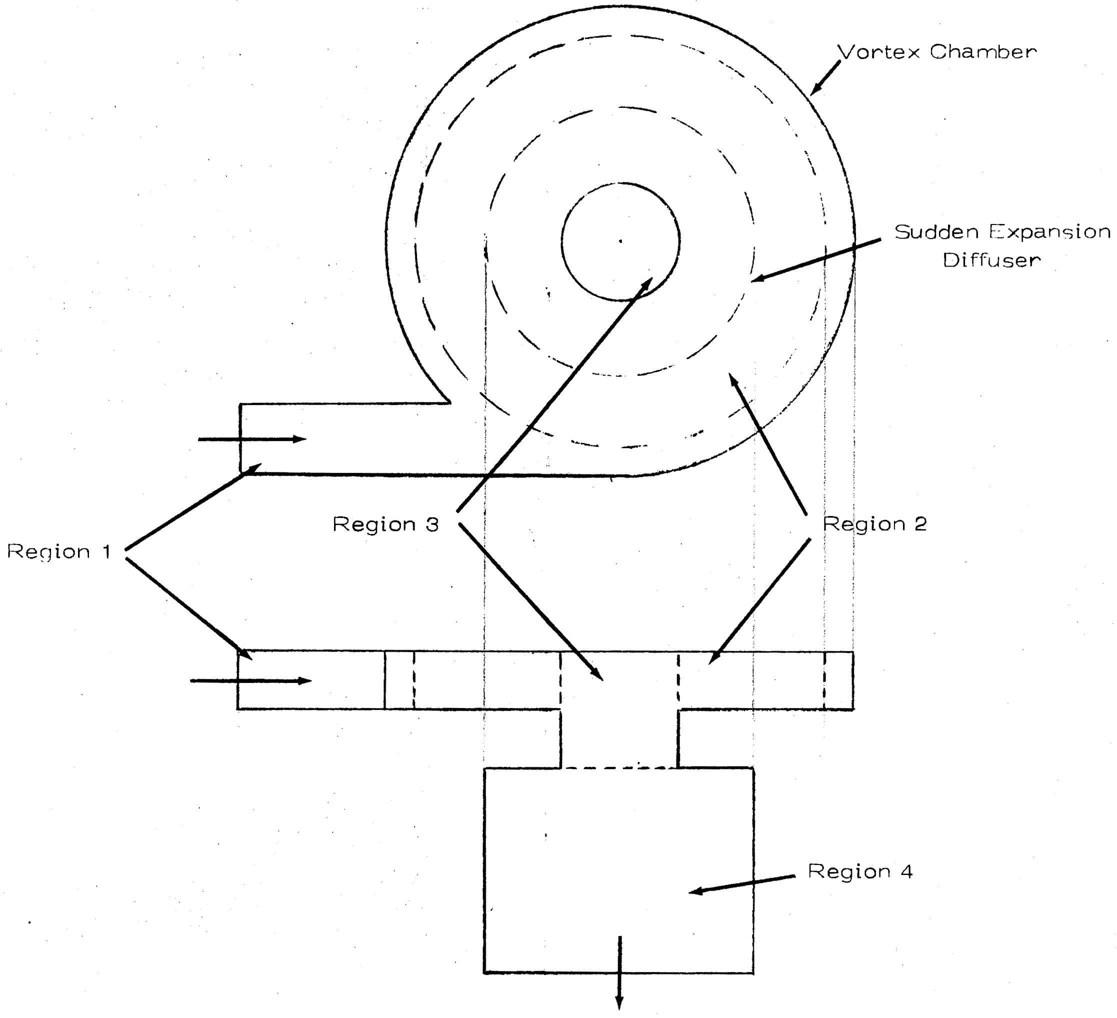

Figure 68. Regions of NSVR

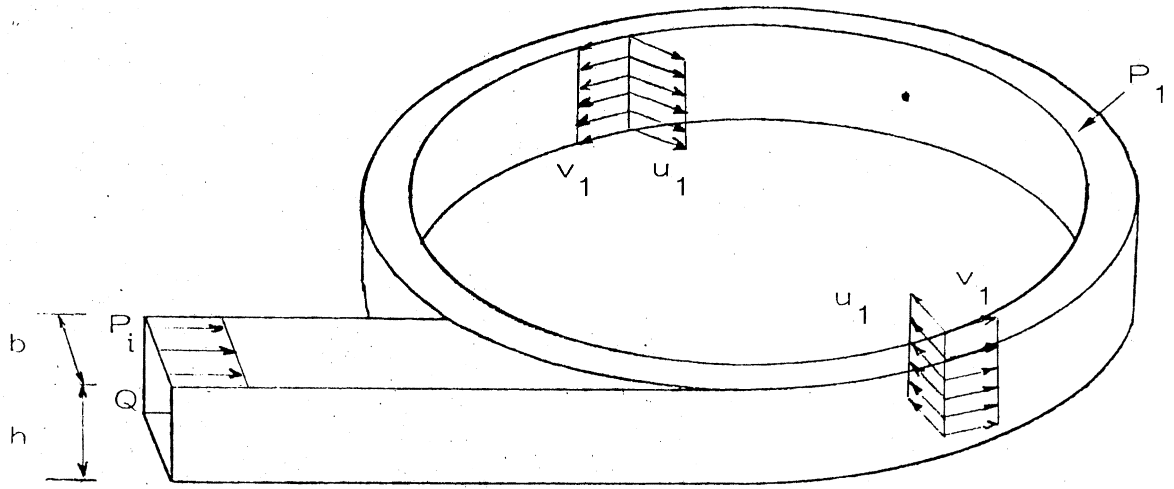

Figure 69. Region 1 of Vortex Resistors (SVR and NSVR)

4. The width of the inlet orifice, b, is much smaller than the diameter of vortex chamber (i.e., $b \ll 2r_1$).

B.1.2. Governing Equations

Flow Rate: $Q = C_{d1} bh\sqrt{2(p_i - p_1)/\rho}$ (B.1)

Radial Velocity at inlet $\}$ $u_1 = -Q/2\pi r_1 h$ (B.2)

Conservation of angular momentum $\}$ $\dfrac{\rho r_1}{bhC_{d1}} Q^2 - \rho r_1 Q v_1 = 2\pi r_1^2 h\tau_{t1}$ (B.3)

Shear Stress:

$$\tau_{t1} = 0.664\ \mu v_1^{1.5} / \sqrt{\nu x_{m1}} \tag{B.4}$$

where

$$x_{m1} = 2r_1[2\pi - \cos^{-1}(\frac{r_1 - b}{r_1})]$$

Orifice Discharge Coefficient:

$$C_{d1} = \sum_{i=1}^{5} \sum_{j=1}^{6} C_{ij}(\log_{10} Re_{d_e})^{i-1} (\frac{1}{d_e})^{j-1} \tag{B.5}$$

where

$$Re_{d_e} = \frac{4Q}{\pi d_e \nu}, \quad d_e = \frac{2bh}{b+h}$$

```
C(1,1)=0.209285657990720 D 00 ,C(2,1)=0.791788479941879 D-02
C(3,1)=0.226876244315706 D 00 ,C(4,1)=-0.507148451077533D-01
C(5,1)=-.249327806165838 D-02 ,C(1,2)=-0.795026948224413D 00
C(2,2)=0.142923814768118 D 01 ,C(3,2)=-0.107062947471109D 01
C(4,2)=0.327389281735691 D 00 ,C(5,2)=-0.322173197963765D-01
C(1,3)=0.632542509986194 D 00 ,C(2,3)=-0.127600317094214D 01
C(3,3)=0.934492443943111 D 00 ,C(4,3)=-0.286766619747770D 00
C(5,3)=0.304900339103475 D-01 ,C(1,4)=-0.151492790673141D 00
C(2,4)=0.312611655321839 D 00 ,C(3,4)=-0.229092531851455D 00
C(4,4)=0.707338263930315 D-01 ,C(5,4)=-0.766974040642524D-02
C(1,5)=0.148165042552580 D-01 ,C(2,5)=-0.307706419128231D-01
C(3,5)=0.225854454114608 D-01 ,C(4,5)=-0.700958813169788D-02
C(5,5)=0.768051230807445 D-03 ,C(1,6)=-0.518515906302915D-03
C(2,6)=0.107854148254401 D-02 ,C(3,6)=-0.792969865409395D-03
C(4,6)=0.247201065756165 D-03 ,C(5,6)=-0.272806432199908D-04
```

Equation (B.5) is an empirical model developed from the experimental data of reference [18] and is accurate to within 5 percent error in the range

$$10 \leq Re_{de} \leq 2200$$

$$0.5 \leq l_1/d_e \leq 12.$$

B.2. Region 2

B.2.1. Assumptions

1. Flow is symmetric, see Figure 70.
2. Flow is one-dimensional, i.e., pressure and velocities (radial and tangential) are functions of only the radial distance.
3. Friction in the radial direction is neglected.

B.2.2. Governing Equations

Radial Momentum: $$u \frac{du}{dr} - \frac{v^2}{r} = - \frac{1}{\rho} \frac{dp}{dr} \tag{B.6}$$

Tangential Momentum: $$u \frac{dv}{dr} + \frac{uv}{r} = \frac{1}{\rho} \frac{\partial \tau_{t2}}{\partial y} \tag{B.7}$$

Continuity: $$\frac{d}{dr} (ru) = 0 \tag{B.8}$$

Shear Stress: $$\tau_{t2} \Big|_{y=\pm \frac{h}{2}} = \mp \frac{12\mu}{h} v \tag{B.9}$$

This shear stress value is twice that for fully developed laminar flow between parallel plates.

B.3. Region 3

Figure 71 shows region 3 of NSVR.

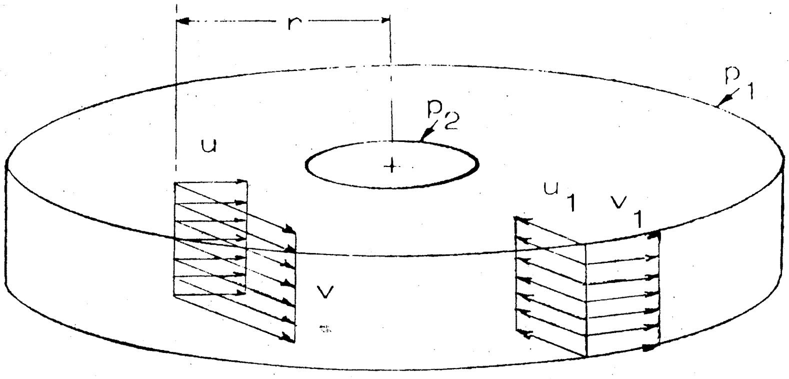

Figure 70. Region 2 of Vortex Resistors (NSVR and SVR)

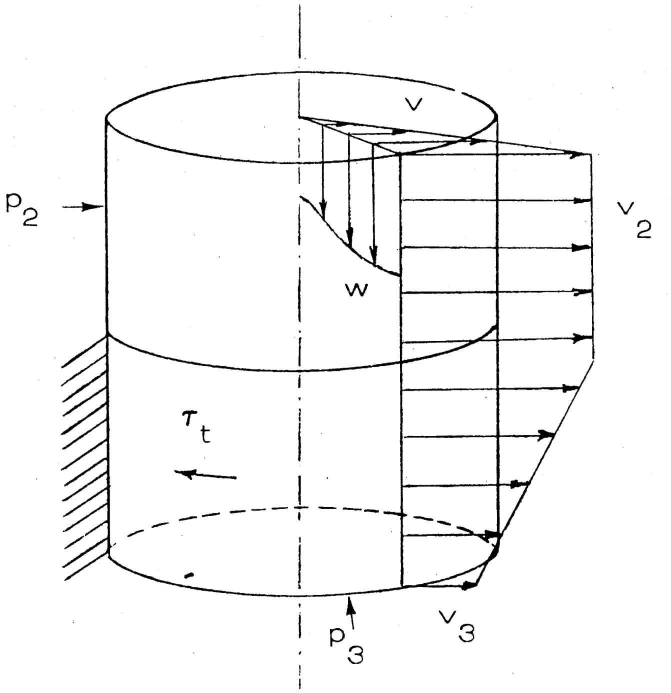

Figure 71. Region 3 of NSVR

B.3.1. Assumptions

1. Radial velocity has a discontinuity at region 3's boundaries in vortex and diffuser chambers. The radial velocity is zero in region 3,

2. Flow is axisymmetric,

3. The rotary motion of fluid is that of a rigid body,

4. The tangential shear stress on the cylindrical surface is given by the flat plate boundary layer stress.

B.3.2. Governing Equations

Tangential velocity }

$$v = \frac{r}{r_2} v_2 \tag{B.10}$$

Pressure distribution }

$$\frac{dp_u}{dr} = \frac{\rho v^2}{r} \tag{B.11}$$

Axial velocity

$$w = \sqrt{2(p_u - p_3)/\rho} \tag{B.12}$$

Boundary condition at $r = r_2$ }

$$p_u = p_2 + \frac{1}{2} \rho u_2^2 \tag{B.13}$$

Flow rate

$$Q = C_{d2} \int_0^{r_2} 2\pi r \, w \, dr \tag{B.14}$$

Conservation of angular momentum }

$$\rho r_2 Q v_2 - \rho r_2 Q v_3 = 2\pi r_2^2 \, l_2 \tau_{t3} \tag{B.15}$$

where

$$\tau_{t3} = 0.664\mu \left(\frac{v_2 + v_3}{2}\right)^{1.5} / \sqrt{\nu x_{m2}}$$

$$x_{m2} = 2\pi r_2 .$$

B.4. Region 4

B.4.1. Assumptions

1. The diffuser chamber is assumed to be large enough to result in small velocity heads.

2. The diffuser efficiency is assumed to be 0.5. That is 50 percent of the kinetic energy is recovered in the diffuser. This figure (50 percent) is selected on the basis of the axial momentum equation (written for the control volume comprising of region 4 of NSVR) assuming potential vortex and neglecting axial velocity terms. The resulting axial momentum equation is

$$p_o - p_3 = \frac{1}{2}\rho v_3^{\,2} \,[\, 1 - \frac{A_2}{A_o} - \frac{A_2}{A_o} \ln(\frac{A_o}{A_2})]$$

which gives a pressure recovery of approximately 50 percent. (Assumptions of rigid body rotation and constant tangential velocity lead to unbounded pressure recovery for increasing diffuser dimensions.)

B.4.2. Governing Equations

$$p_o = p_3 + \frac{1}{4}\rho(\frac{Q^2}{\pi^2 r_2^4} + v_3^2) \qquad \text{(B.16)}$$

Euqations (B.1) through (B.16) describe the mathematical model of the NSVR in laminar regime of operation. These equations may be rearranged for numerical solution as follows:

From equation (B.1):

$$p_1 = p_i - \frac{\rho}{2(C_{d1}bh)^2} Q^2 \qquad \text{(B.17)}$$

Combining equations (B.3) and (B.4):

$$a_1 v_1^{1.5} + a_2 v_1 - a_3 = 0 \qquad \text{(B.18)}$$

where

$$a_1 \equiv 1.328\pi r_1^2 \, h\rho\sqrt{\nu/x_{m1}}$$

$$a_2 \equiv \rho r_1 Q$$

$$a_3 \equiv \rho r_1 Q^2/bhC_{d1} \, .$$

From Equation (B.8):

$$u_2 = r_1 u_1 / r_2 \qquad \text{(B.19)}$$

From Equations (B.7) - (B.9):

$$v_2 = \frac{r_1/r_2}{\exp[\frac{\lambda}{2}(1-\frac{r_2^2}{r_1^2})]} \quad v_1 \qquad \text{(B.20)}$$

where

$$\lambda \equiv 24\ \nu r_1 / h_1^2 u_1 l.$$

From Equations (B.6) - (B.9):

$$p_2 = p_1 - \frac{\rho u_1^2}{2} \left(\frac{r_1^2}{r_2^2} - 1\right) - \frac{v_1^2}{\exp(\lambda)} \cdot$$

$$\left[\frac{1}{2}\left(\frac{r_1^2}{r_2^2} - 1\right) - \lambda \ln\left(\frac{r_2}{r_1}\right) + \sum_{i=2}^{\infty} \frac{\lambda^i \{1-(r_2/r_1)^{2i-2}\}}{i!\ (2i-2)} \right]$$

Combining Equations (B.10) - (B.14) gives:

$$Q = \frac{2}{3} \frac{C_{d2}\pi r_2^2}{v_2^2} \left[\frac{2(p_2-p_3)}{\rho} + u_2^2\right]^{3/2} \cdot \left[1-\left|1-\frac{v_2^2}{\frac{2}{\rho}(p_2-p_3)+u_2^2}\right|^{3/2}\right] \qquad \text{(B.22)}$$

From Equation (B.15):

$$v_3 = v_2 - \frac{0.664\pi\nu r_2 l_2}{Q\sqrt{2\nu x_{m2}}} \quad (v_2 + v_3)^{1.5} \qquad \text{(B.23)}$$

Numerical Computations Algorithm

Given the geometry, fluid properties and flow rate Q the pressure drop $\Delta P = P_i - P_o$ may be computed as follows:

Steps:
1. Calculate u_1 from Equation (B.2), and p_1 from Equation (B.17) by assuming any arbitrarily chosen value of p_i.
2. Solve Equation (B.18) for v_1. Due to nonlinearity it will involve a numerical search.
3. Calculate v_2 from Equation (B.20), and p_2 from Equation (B.21). Note that the series in Equation (B.21) converges to a desired accuracy within a finite number of terms (less than 50 terms).
4. Numerically solve Equation (B.22) for p_3, and Equation (B.23) for v_3.
5. Compute p_o from Equation (B.16) and calculate $\Delta P = p_i - p_o$.

APPENDIX C

ONE-DIMENSIONAL MODEL OF SVR

Figure 72 shows the five regions of SVR. The models of regions 1, 2, and 3 of SVR and NSVR (described in Appendix B) are identical. Only the models of regions 4 and 5 are described below.

C.1. Region 4

Figure 73 shows region 4 of SVR.

C.1.1. Assumptions

1. Flow is assumed one-dimensional and axisymmetric.

2. A fraction of the angular momentum at the inlet of the diffuser chamber is recovered as potential energy. The remainder is dissipated completely in the diffuser chamber.

3. The shear stress in the radial direction is neglected. Blassius solution of flat plate boundary layer is used for the tangential shear stress used in the model.

C.1.2. Governing Equations

Radial Momentum: $$u\frac{du}{dr} - \frac{v^2}{r} = -\frac{1}{\rho}\frac{dp}{dr} \qquad (C.1)$$

Tangential Momentum: $$u\frac{dv}{dr} + \frac{uv}{r} = \frac{1}{\rho}\frac{\partial \tau_{\tau}}{\partial y} \qquad (C.2)$$

Continuity: $$\frac{d}{dr}(ru) = 0 \qquad (C.3)$$

Shear Stress: $$\tau_t\Big|_{y=\pm\frac{h}{2}} = \mp\frac{12\mu}{h}v \qquad (C.4)$$

Boundary Conditions:

$$p_3' = p_3 + \frac{1}{2}\rho(v_3^2 - v_3'^2 \qquad (C.5)$$

$$v(r_1) = 0 \qquad (C.6)$$

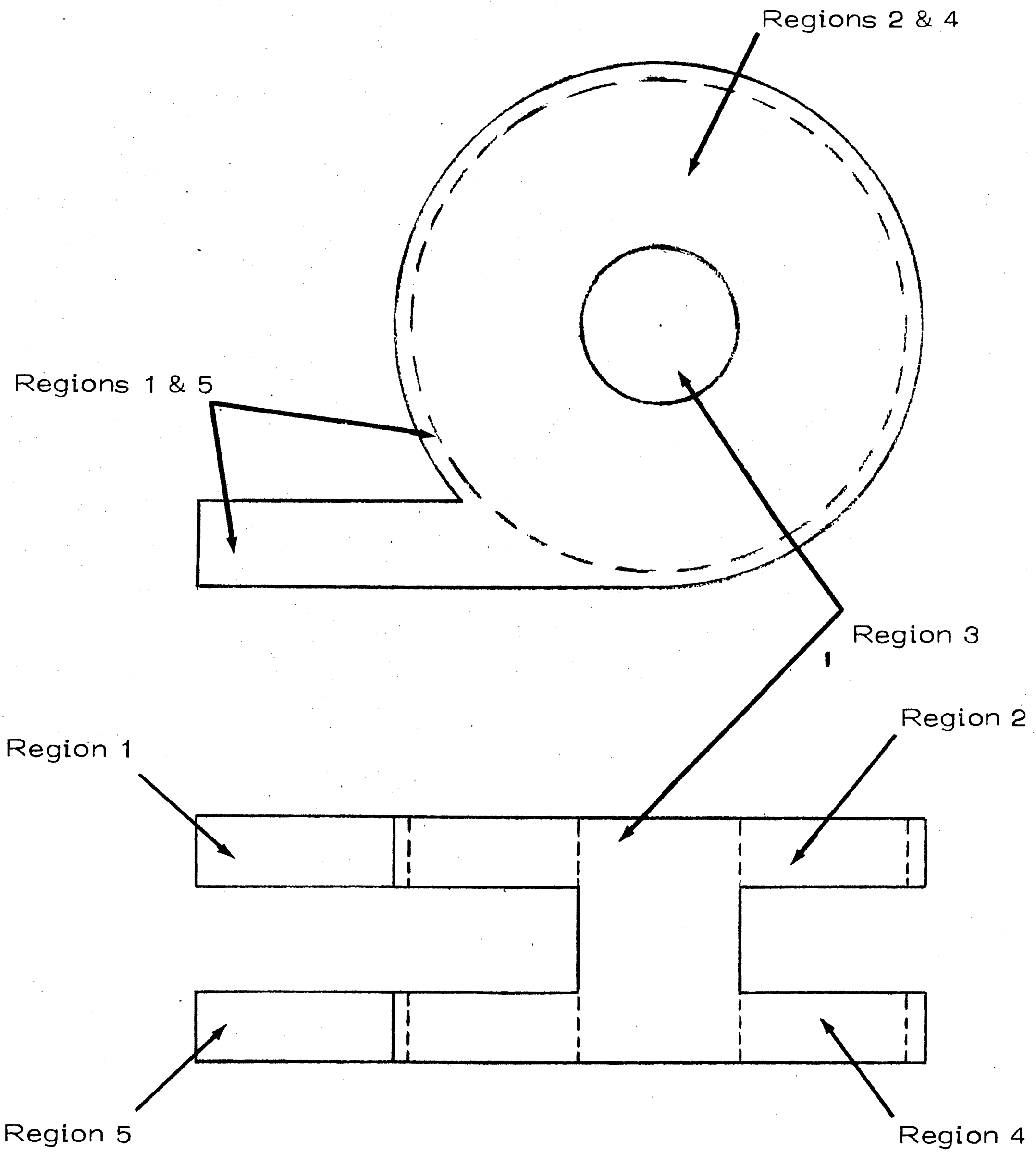

Figure 72. Regions of SVR

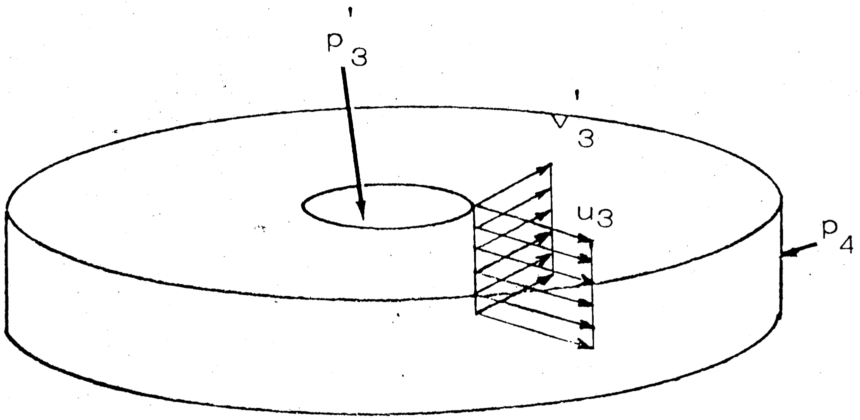

Figure 73. Region 4 of SVR

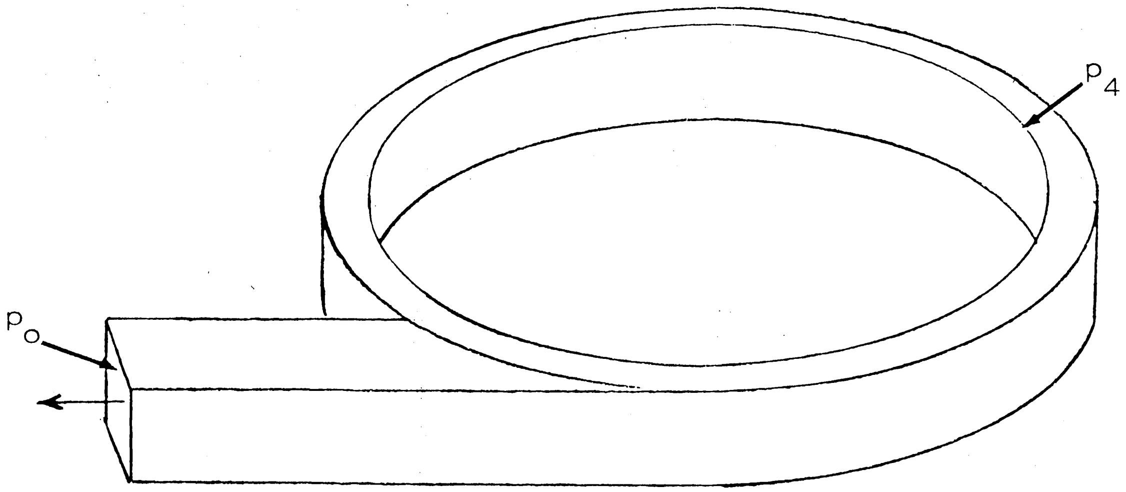

Figure 74. Region 5 of SVR

C.2. Region 5

Figure 74 shows region 5 of SVR.

C.2.1. Assumptions

1. The tangential momentum at the annular inlet of region 5 is assumed to be dissipated completely due to friction at the annular wall.

2. An orifice characteristic may be used for the exit channel.

C.2.2. Governing Equations

$$Q = C_{d3} bh \sqrt{2(p_4 - p_o)/\rho} \tag{C.7}$$

where $C_{d3} = C_{d1}$ and is calculated from Equation (B.5).

Equations (B.1) through (B.16) and (C.1) through (C.7) describe the complete SVR model. Equations (B.17) through (B.23) are valid for this case. Additional equations needed for calculations of p_4 and p_o are developed below: From Equations (C.2) - (C.4):

$$v = \frac{r_2/r}{\exp[\frac{\lambda}{2} \frac{r^2 - r^2{}_2)}{r_1^2}]} v_3' \tag{C.8}$$

From Equation (C.8) it can be observed that the boundary condition (C.6) cannot be satisfied exactly. Therefore instead of requiring $v(r_1)$ to be zero, it was allowed to be small enough so that the associated angular momentum was a negligible fraction of the total momentum. Therefore

$$v_3' = \frac{\exp\left[\frac{\lambda}{2}\left(\frac{r_1^2 - r_2^2}{r_1^2}\right)\right]}{r_2/r_1} \quad v(r_1) \tag{C.9}$$

where $v(r_1)$ = 0.01 inch/sec (assumed).

Combining Equations (C.1), (C.3), and (C.8) gives upon simplification:

$$p_4 = p_3' + \left(1 - \frac{r_2^2}{r_1^2}\right) \frac{1}{2}\rho u_3^2 + \rho \left(\frac{r_2^2}{r_1^2} v_3'^2\right) - \exp\left(\lambda \frac{r_2^2}{r_1^2}\right) \left[\frac{1}{2}\left(\frac{r_1^2}{r_2^2} - 1\right) - \lambda \ln\left(\frac{r_1}{r_2}\right) + \sum_{i=2}^{\infty} \frac{(-\lambda)^i \{1-(r_2/r_1)^{2i-2}\}}{i!(2i-2)}\right] \tag{C.10}$$

From Equation (C.5)

$$p_o = p_4 - \frac{\rho}{2(C_{d3}bh)^2} \quad Q^2 \tag{C.11}$$

Equations (B.17) - (B.23) and (C.9), (C.5), (C.10), and (C.11) constitute the SVR model for numerical calculations. These equations are solved sequentially to determine the pressure drop across the resistor for a given flow rate.

APPENDIX D

TWO-DIMENSIONAL MODEL FOR NSVR

In Appendix B a steady-state one-dimensional model was derived for the NSVR. The velocity profiles in region 2 (i.e., the vortex chamber) were assumed to be uniform across the chamber height. In this appendix this restriction has been relaxed and the velocity profiles are allowed to be nonuniform. Appropriate equations are derived for region 2 based on Von Kármán's momentum integral technique. Equations derived earlier in Appendix B for regions 1, 3, and 4 remain the same.

D.1. Region 2

Figure 75 shows region 2 of NSVR.

D.1.1. Assumptions

1. Vortex chamber is thin, i.e., $h/r_1 \ll 1$.
2. Flow is axisymmetric.
3. Flow is symmetric about xx(see Figure 75).
4. The radial velocity in the core is zero when the flow is fully developed.

D.1.2. Governing Equations

Continuity:

$$\frac{\partial u}{\partial r} + \frac{u}{r} = -\frac{\partial w}{\partial y} \qquad \text{(D.1)}$$

Boundary Layer Momentums:

$$u\frac{\partial u}{\partial r} - \frac{v^2}{r} + w\frac{\partial u}{\partial y} = -\frac{1}{\rho}\frac{dp}{dr} + \nu\frac{\partial^2 u}{\partial y^2} \qquad \text{(D.2)}$$

$$u\frac{\partial v}{\partial r} + \frac{uv}{r} + w\frac{\partial v}{\partial y} = \nu\frac{\partial^2 v}{\partial y^2} \qquad \text{(D.3)}$$

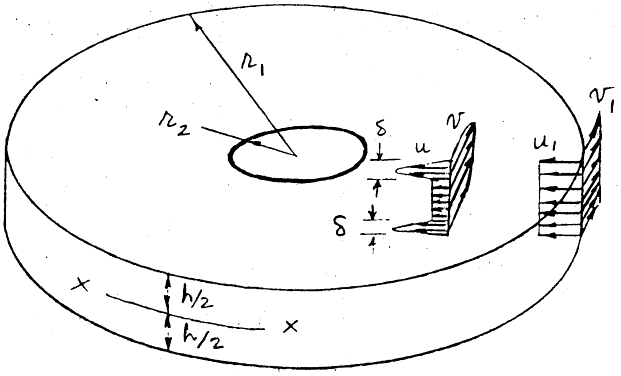

Figure 75. Region 2 of NSVR

Core Momentum: $$u_\delta \frac{du_\delta}{dr} - \frac{v_\delta^2}{r} = \frac{-1}{\rho} \frac{dp}{dr} \qquad (D.4)$$

$$u_\delta \frac{dv_\delta}{dr} + \frac{u_\delta v_\delta}{r} = 0 \qquad (D.5)$$

Boundary Conditions:

$$\begin{aligned} &\text{At } y = 0, \quad u = v = w = 0 \\ &\text{At } y = h/2, \quad w = \partial u/\partial y = \partial v/\partial y = 0 \\ &\text{At } r = r_1, \quad u = u_1 \\ &\qquad\qquad\quad v = v_1 \\ &\qquad\qquad\quad w = 0 \\ &\qquad\qquad\quad p = p_1 \end{aligned} \qquad (D.6)$$

Velocity Profiles:

$$\left.\begin{aligned} &\left.\begin{aligned} u &= u_\delta(r) f(\eta) + u_\delta(r)\, g(\eta) \\ v &= v_\delta(r) f(\eta) \end{aligned}\right\} \quad 0 \leq y \leq \delta \\ &\left.\begin{aligned} u &= u_\delta(r) \\ v &= v_\delta(r) \end{aligned}\right\} \quad \delta < y \leq L/2 \\ &\eta \equiv y/\delta \end{aligned}\right\} \qquad (D.7)$$

Integrating Equations (D.1) - (D.3) using the velocity profiles of (D.7) and the boundary conditions of (D.6) gives the following system of ordinary differential equations (note equations D.4 and D.5 are also included):

$$[(\alpha_5-1)u_\delta+\alpha_4 u_s]\frac{d\delta}{dr} + [(\alpha_5-1)\delta+\frac{h}{2}\ ] \frac{du_\delta}{dr} + [\alpha_4 \delta] \frac{du_\delta}{dr} = \frac{1}{r} [(\alpha_5-1)$$

$$\delta u_\delta + \frac{h}{2} u_\delta + \alpha_4 \delta\ u_s] \qquad (D.8)$$

$$[(\alpha_1-\alpha_5)\ u_\delta^2 + (2\alpha_2-\alpha_4)\ u_\delta u_s + \alpha_3 n_s^2\ ] \frac{d\delta}{dr} + [(2\alpha_1-\alpha_5)\ \delta u_\delta +$$

$$2\alpha_2 \delta u_s] \frac{du_\delta}{dr} + [(2\alpha_2-\alpha_4)\ \delta u_\delta + 2\alpha_3 \delta u_s] \frac{du}{dr} + [\frac{\delta}{\rho}] \frac{dp}{dr} = \frac{\delta}{r}$$

$$[\alpha_1 \nu_\delta^2 - (\alpha_1-\alpha_5)\ u_\delta^2 - (2\alpha_2-\alpha_4)\ u_\delta u_s - \alpha_3 u_s^2] - \frac{\nu}{\delta} (f_o' u_\delta +$$

$$g_o' u_s) \qquad (D.9)$$

$$[(\alpha_1-\alpha_5)\, U_\delta + (\alpha_2-\alpha_4)\, u_s]\, \frac{d\delta}{dr} + [(\alpha_1-\alpha_5)\delta].$$

$$\frac{d\delta}{dr} + [(\alpha_1\delta u_\delta + \alpha_2\delta u_s)/v_\delta]\, \frac{dv_\delta}{dr} +$$

$$[(\alpha_2 - \alpha_4)\delta]\, \frac{du_s}{dr} = \frac{\delta}{r}\, [-(2\alpha_1-\alpha_5).$$

$$u_\delta - (2\alpha_2 - \alpha_4)\, u_s] - \frac{\nu}{\delta} f_o' \qquad \text{(D.10)}$$

$$[u_\delta]\, \frac{du_\delta}{dr} + [\frac{1}{\rho}]\, \frac{dp}{dr} = v_\delta^2/r \qquad \text{(D.11)}$$

where

$$\alpha_1 = \int_o^1 f^2 d\eta \;, \quad \alpha_2 = \int_o^1 fg d\eta$$

$$\alpha_3 = \int_o^1 g^2 d\eta \;, \quad \alpha_4 = \int_o^1 g d\eta$$

$$\alpha_5 = \int_o^1 f d\eta \;, \quad f_o' = \frac{df}{d\eta}\Big|_{\eta = 0}$$

$$g_o' = \frac{dg}{d\eta}\Big|_{\eta = 0}$$

Profile functions f and g may be selected arbitrarily to satisfy the boundary conditions [$f(0)=0$, $f(1)=1$, $f'(0)>0$, $f'(1)=0$ and $g(0)=g(1)=0$, $g'(0)>0$, $g'(1)=0$]. The following functions satisfy these conditions:

$$f(\eta) = c[\eta - \frac{c-1}{c}\{\eta^{c/(c-1)}\}] \qquad \text{(D.12)}$$

$$g(\eta) = b_o\, [\, \eta(1-\eta)^{b_1}] \qquad \text{(D.13)}$$

where

$$b_o = (b_1+1)^{b_1+1}/(b_1^{b_1}). \quad (b_1=2 \text{ and } c=1.25 \text{ are used}).$$

There exists a singularity at $r=r_1$, for the system of differential equations (D.8)-(D.11). Approximate solutions for δ, u_s and u_δ may be obtained by locally linearizing the differential equations. The resulting solution is valid in the neighborhood of the singularity.

D.2. Approximate Solution Near The Singularity

Forcing u_δ to zero Equations (D.9)-(D.11) gives respectively

$$\alpha_3 u_s^2 \frac{d\delta}{dr} + 2\alpha_3 \delta u_s \frac{du_s}{dr} + \frac{\delta}{\rho}\frac{dp}{dr}$$

$$= \frac{\delta}{r}\left[\alpha_1 v_\delta^2 - \alpha_3 u_s^2\right] - \frac{\nu}{\delta} g_o' u_s \tag{D.14}$$

$$(\alpha_2-\alpha_4)\, u_s \frac{d\delta}{dr} + (\alpha_2-\alpha_4)\delta \frac{du_s}{dr}$$

$$= -\frac{(2\alpha_2-\alpha_4)}{r}\delta u_s - \frac{\nu f_o'}{\delta} + \frac{\alpha_2}{r}\delta u_s \tag{D.15}$$

$$\frac{1}{\rho}\frac{dp}{dr} = \frac{v_\delta^2}{r} \tag{D.16}$$

Assuming potential core flow, Equation (D.16) gives

$$p(r) = p_1 + \frac{p}{2}(r_1 v_1)^2\left(\frac{1}{r_1^2} - \frac{1}{r^2}\right) \tag{D.17}$$

Rearranging Equation (D.15)

$$(\alpha_2-\alpha_4)\frac{d}{dr}(\delta u_s) = -\frac{2\alpha_2-\alpha_4}{r}\delta u_s - \frac{\nu f_o'}{\delta} + \frac{\alpha_2}{r}\delta u_s \tag{D.18}$$

At $r=r_1$, $u_s = 0$ but $d/dr(\delta u_s)$ is not negligible. Therefore, neglecting δu_s terms in Equation (D.18) gives

$$(\alpha_2-\alpha_4)\frac{d}{dr}(\delta u_s) = -\frac{\nu f_o'}{\delta} \tag{D.19}$$

Neglecting the radial friction in Equation (D.14) and combining with Equation (D.17) gives

$$\alpha_3 \frac{d}{dr}(\delta u_s^2) + \delta\frac{(r_1 v_1)^2}{r^3} = \alpha_1 (r_1 v_1)^2 \frac{\delta}{r^3} \tag{D.20}$$

In a close neighborhood of r_1 let

$$\delta \cong c_1 \, (\Delta r)^{n_1}$$

$$u_s \cong c_2 \, (\Delta r)^{n_2} \qquad \text{(D.21)}$$

where $\Delta r \equiv r_1 - r$. Substituting from (D.21) in (D.19) and (D.20) gives respectively

$$-(n_1+n_2)\,(\alpha_2-\alpha_4)\; c_1 c_2 \Delta r^{\,n_1+n_2-1} = \frac{\nu f_o'}{c_1}\,(\Delta r)^{-n_1} \qquad \text{(D.22)}$$

$$-(n_1+n_2)\;\alpha_3 c_1 c_2^2\;(\Delta r)^{n_1+2n_2-1} = (\alpha_1-1)\,\frac{c_1(r_1 v_1)^2}{r_1^3}\,(\Delta r)^{n_1} \qquad \text{(D.23)}$$

Equating indices of Δr terms and solving the resulting equations gives

$$n_1 = 0.25$$

$$n_2 = 0.50 \qquad \text{(D.24)}$$

Combining Equations (D.21) - (D.24) gives

$$\delta \cong \left[\frac{\nu f_o'}{0.75(\alpha_4-\alpha_2)}\sqrt{\frac{1.25\alpha_3 r_1}{(1-\alpha_1)v_1^2}}\;\right]^{1/2} (\Delta r)^{1/4}$$

$$u_s \cong -\sqrt{\frac{(1-\alpha_1)v_1^2}{1.25\alpha_3 r_1}}\;(\Delta r)^{1/2}$$

$$u_\delta \cong \frac{u_1 h/2 - \alpha_4 \delta u_s}{\frac{h}{2} - (1-\alpha_5)\,\delta} \qquad \text{(D.25)}$$

The numerical algorithm is similar to the one described in Appendix B for one-dimensional model.

APPENDIX E

DYNAMIC MODEL OF THE NSVR

The dominant dynamics of an NSVR element are expected to be in the vortex chamber, i.e., region 2. The inlet and the central orifices and the diffuser are expected to respond much faster than the vortex chamber. Hence, steady-state models are used for all regions except region 2 of NSVR. One-dimensional approach used for steady-state modeling is also used for dynamic model development as described below.

Governing equations of regions 1, 3, and 4 of NSVR are the same as those given in Appendix B. However, they have been repeated here for eacy reference. (See Appendix B for assumptions involved in modeling of regions 1, 3, and 4.)

E.1. Region 1

E.1.1. Governing Equations

Flow: $$Q = C_{d1} bh \sqrt{2(p_i - p_1)/\rho} \qquad \text{(E.1)}$$

Continuity: $$u_1 = -Q/2\pi r_1 h \qquad \text{(E.2)}$$

Angular Momentum: $$\frac{\rho r_1 Q^2}{bhC_{d1}} - \rho r_1 Q v_1 = 2\pi r_1^2 h \tau_{t1} \qquad \text{(E.3)}$$

where

$$\tau_{t1} = 0.664 \mu v_1^{1.5} / \sqrt{\nu x_{m1}} \qquad \text{(E.4)}$$

E.2. Region 2

E.2.1. Assumptions

Assumptions in addition to those given in Appendix B are given below:

1. There is a time delay T_1 and a first order lag T_2 associated with the propagation of the tangential velocity in the vortex chamber.

2. Variations of through flow are small so that the discharge coefficient variations are negligible.

E.2.2. Governing Equations

Continuity:

$$u_2 = r_1 u_1 / r_2 \tag{E.5}$$

Tangential Momentum:

$$v_2 = \frac{e^{-T_1 s}}{1+T_2 s} \cdot \frac{v_1}{\frac{r_2}{r_1} \exp\{ \frac{\lambda}{2} (1- \frac{r_2^2}{r_1^2})\}} \tag{E.6}$$

where $\lambda \equiv \dfrac{24 \nu r_1}{h^2 |u_1|}$.

Radial Momentum (linearized)

$$\Delta(p_1 - p_2) = k_1 \left(\frac{e^{-T_1 D}}{1+\tau_2 D} \right) \Delta v_1 + k_2 \Delta u_1 \tag{E.7}$$

where k_1 and k_2 are obtained from

$$p_2 = p_1 - \frac{\rho u_1^2}{2} \left(\frac{r_1^2}{r_2^2} - 1 \right) - \frac{\rho v_1^2}{e^\lambda} \left[\frac{1}{2} \left(\frac{r_1^2}{r_2^2} - 1 \right) - \lambda \ln\left(\frac{r_2}{r_1} \right) + \sum_{i=2}^{\infty} \frac{\lambda^i \{1-(r_2/r_1)^{2i-2}\}}{i!\,(2i-2)} \right] \tag{E.8}$$

E.3. Region 3

E.3.1. Governing Equations

Radial Velocity: $u_3 = -u_2$ (E.9)

Angular Momentum:

$$v_3 = v_2 - \left(\frac{0.664\pi\nu r_2 l_2}{Q\sqrt{2\nu x_{m2}}}\right) \cdot (v_2+v_3)^{1.5} \tag{E.10}$$

Flow Rate:

$$Q = \frac{2}{3}\,\frac{C_{d2}\pi r_2^2}{v_2^2}\left[\frac{2(p_2-p_3)}{\rho} + u_2^2\right]^{3/2} \cdot \left[1-\left|1-\frac{v_2^2}{\frac{2}{\rho}(p_2-p_3)+u_2^2}\right|^{3/2}\right] \tag{E.11}$$

E.4. Region 4

E.4.1. Governing Equations

Pressure Recovery: $p_o = p_3 + \frac{1}{4}\,\rho(u_3^2 + v_3^2)$ (E.12)

Equations (E.1) - (E.12) can be linearized (wherever necessary) and combined to result in a linear dynamic model of NSVR which can be used for small signal AC analysis. Linearizing Equations (E.1) and (E.2) gives respectively:

$$\Delta p_i - \Delta p_1 = a_1\,\Delta Q \tag{E.13}$$

and

$$\Delta u_1 = a_2 \Delta Q \tag{E.14}$$

where

$$a_1 = \sqrt{2\rho(p_i^* - p_1^*)}/C_{d1}bh$$

$$a_2 = -1/2\pi r_1 h$$

combining Equation (E.3) and (E.4) and linearizing

$$\Delta v_1 = a_3 \Delta Q \tag{E.15}$$

where

$$a_3 \equiv \left[\frac{2\rho r_1 Q^*}{bhC_{d1}} - \rho r_1 v_1^*\right] / \left[1.992\pi r_1^2 h^2 \mu \sqrt{\frac{v_1^*}{\nu x_{m1}}} + \rho r_1 Q^*\right].$$

Linearizing Equations (E.5) and (E.6) gives respectively

$$\Delta u_2 = a_4 \Delta u_1 \tag{E.16}$$

and

$$\Delta v_2 = a_5 \left(\frac{e^{-T_1 D}}{1+T_2 D}\right) \Delta v_1 + a_6 \Delta u_1 \tag{E.17}$$

where

$$a_4 \equiv r_1/r_2$$

$$a_5 \equiv 1/\left[\frac{r_2}{r_1} \exp\left\{\frac{\lambda^*}{2}(1-r_2^2/r_1^2)\right\}\right]$$

$$a_6 \equiv \frac{v_1^*}{\frac{r_2}{r_1} \exp\left\{\frac{\lambda^*}{2}\left(1-\frac{r_2^2}{r_1^2}\right)\right\}} \left\{-\frac{1}{2}\left(1-\frac{r_2^2}{r_1^2}\right)\frac{\lambda^*}{u_1^*}\right\}$$

From Equation (E.8):

$$k_1 = \frac{2\rho v_1^*}{\exp(\lambda^*)}\left[\frac{1}{2}\left(\frac{r_1^2}{r_2^2} - 1\right) - \lambda^* \ln\left(\frac{r_2}{r_1}\right) + \sum_{i=2}^{\infty} \frac{\lambda^{*i}\{1-(r_2/r_1)^{2i-2}\}}{i!\,(2i-2)}\right]$$

$$k_2 = \rho u_1^*\left(\frac{r_1^2}{r_2^2} - 1\right) - \frac{\rho v_1^{*2}}{\exp(\lambda^*)}\left[\frac{1}{2}\left(\frac{r_1^2}{r_2^2} - 1\right) - \lambda^* \ln\left(\frac{r_2}{r_1}\right) + \sum_{i=2}^{\infty} \frac{\lambda^{*i}\{1-(r_2/r_1)^{2i-2}\}}{i!\,(2i-2)}\right] \cdot \frac{\lambda^*}{|u_1^*|} + \frac{\rho v_1^{*2}}{|u_1|\exp(\lambda^*)}.$$

---

*Asterisk refers to values of the variables at the operating point.

$$[-\lambda^* \ln (\frac{r_2}{r_1}) + \sum_{i=2}^{\infty} \frac{1-(r_2/r_1)^{2i-2}}{(i-1)\,!\,(2i-2)} \lambda^{*i}] \qquad \text{(E.18)}$$

Linearizing Equations (E.9) and)E.10) gives respectively:

$$\Delta\, u_3 = -\Delta u_2 \qquad \text{(E.19)}$$

and

$$\Delta v_3 = a_7 \Delta v_2 + a_8 \Delta Q \qquad \text{(E.20)}$$

where

$$a_7 \equiv (1-C_1)/(1+C_1)$$

$$a_8 = \frac{0.664 \pi \nu r_2 l_2 (v_2^* + v_3^*)^{1.5}}{Q^{*2} \sqrt{2\nu x_{m2}} \cdot (1+C_1)}$$

$$C_1 = \frac{0.996 \pi \nu r_2 l_2}{Q^* \sqrt{2\nu x_{m2}}} (v_2^* + v_3^*)^{0.5} \quad .$$

From Equation (E.11):

$$\Delta p_2 - \Delta p_3 = a_9 \Delta u_2 + a_{10} \Delta v_2 + a_{11} \Delta Q \qquad \text{(E.21)}$$

where

$$a_9 \equiv -\rho u_2^*$$

$$a_{10} \equiv [\frac{4}{3} \frac{C_3}{v_2^*} C_2^{3/2} (1-C_4^{3/2}) - 2v_2^* C_3 \sqrt{C_2 C_4} \cdot$$

$$\text{sign}\ (1-v_2^{*2}/C_2)]/\frac{2}{\rho}[C_3 \sqrt{C_2} (1-C_4^{3/2}) - C_3 C_2^{3/2} \sqrt{C_4} \cdot$$

$$\text{sign}\ (1-v_2^{*2}/C_2)(v_2^*/C_2)^2].$$

$$a_{11} = 1/\frac{2}{\rho}[C_3 \sqrt{C_2} (1-C_4^{3/2}) - C_3 C_2^{3/2} \sqrt{C_4}.$$

$$\text{sign } (1-v_2^{*2}/C_2)(v_2^*/C_2)^2]$$

$$C_2 \equiv \frac{2(p_2^*-p_3^*)}{\rho} + u_2^{*2}$$

$$C_3 = C_{d2}\ \pi r_2^2/v_2^{*2}$$

$$C_4 = |1 - v_2^{*2}/C_2| .$$

Linearizing Equation (E.12) gives:

$$\Delta p_3 - \Delta p_o = a_{12}\Delta u_3 + a_{13}\Delta v_3 \qquad \text{(E.22)}$$

where

$$a_{12} = -\rho u_3^*$$

$$a_{13} = -\rho v_3^* .$$

Equations (E.7), (E.13) - (E.22) can be combined to give

$$\frac{\Delta p_i - \Delta p_o}{\Delta Q} = e_1 + e_2 \frac{e^{-T_1 D}}{1+T_2 D} \qquad \text{(E.23)}$$

where

$$e_1 = a_1 + a_{11} + a_8 a_{13} + a_2(k_2 + a_4 a_9 + a_6 a_7 a_{13} + a_6 a_{10} -$$
$$a_4 a_{12})$$

$$e_2 = a_3 \{k_1 + (a_7 a_{13} + a_{10}) a_5\}.$$

E.5. Loading Resistor

For an orifice type of loading resistor the flow rate is given by:

$$Q = C_{d4} A \sqrt{2p_o/\rho} \qquad \text{(E.24)}$$

assuming the downstream end of the orifice is at atmospheric pressure. Linearizing Equation (E.24) gives (assuming ΔQ is small enough so that

C_{d3} remains constant):

$$\Delta Q = a_{14} \Delta p_o \tag{E.25}$$

where

$$a_{14} \equiv \frac{1}{2} C_{d4} \quad A\sqrt{2/\rho p_o^*} \quad .$$

From Equations (E.23) and (E.25),

$$\frac{\Delta p_o}{\Delta p_i} = \frac{k_3(1 - T_2D)}{1 + T_2D + k_4 \exp(-T_1D)} \tag{E.26}$$

where

$$k_3 \equiv 1/(1 + a_{14}e_1)$$

$$k_4 = a_{14}e_2/(1 + a_{14}e_1).$$

VITA

Syed Hamid

Candidate for the Degree of

Doctor of Philosophy

Thesis: STATIC AND DYNAMIC ANALYSES OF VORTEX RESISTORS

Major Field: Mechanical Engineering

Biographical:

Personal Data: Born in Tandur, India, June 24, 1947, the son of Noor Jahan Begum and Syed Omer.

Education: Graduated from Government High School, Tandur, India in 1962; studied up to final year of Bachelor of Engineering course in Osmania University; received the Bachelor of Engineering in Mechanical Engineering from Sri Venkateswara University, Anantapur, India in 1969; received the Master of Science degree from Oklahoma State University, Stillwater, Oklahoma, in 1972; completed the requirements for the Doctor of Philosophy degree at Oklahoma State University in July, 1976.

Professional Experience: Instructor, College of Engineers, Hyderabad, from January, 1970 to August, 1970; graduate research assistant, Oklahoma State University, 1970-76.